University of Alberta

Magnetically targeted deposition and retention of particles in the airways for drug delivery

by

Javed Maqsud Ally

A thesis submitted to the Faculty of Graduate Studies and Research
in partial fulfillment of the requirements for the degree of

Doctor of Philosophy

Mechanical Engineering

Spring 2010
Edmonton, Alberta

Examining Committee

Alidad Amirfazli, Mechanical Engineering (supervisor)

Carlos F. Lange, Mechanical Engineering

Sushanta Mitra, Mechanical Engineering

Subir Bhattacharjee, Mechanical Engineering

Anthony Yeung, Chemical Engineering

Edgar Acosta, Chemical Engineering & Applied Chemistry, University of Toronto

Dedication

In the name of God, the Compassionate, the Merciful:

"Recite, in the name of your Lord who created: who created humankind from a clot of blood. Recite, for your Lord is most generous, who taught by the pen, taught humankind what it did not know."

– Quran 96:1-5, trans. Thomas Cleary

I begin by thanking God, the Creator and Teacher of humankind. This thesis is dedicated to the teachers who have helped to shape me and get me this far: My mother, who taught me that there is something to learn from every one; my father for showing me the discipline required to be a scholar; my sister Alia, who is still teaching me. Also, among others, Bev Crossman, Jeanne Hetherington, Gordon Skeels, Ken Marshall, and most recently, Alidad Amirfazli. Thank you for the doors you have opened for me.

Abstract

This thesis examines the mechanisms of magnetic particle deposition and retention in human airways for magnetically targeted drug delivery. As this is a novel application, fundamental studies were performed to establish the necessary background knowledge for further development.

Magnetic particle deposition from an aerosol in simulated airway conditions was studied using numerical and experimental models. The model results showed qualitative agreement; discrepancies were due to particle aggregation, which enhances deposition. Aerosol flow rate had a limited effect; the main factor in effective deposition was the proximity of the particle trajectories to the magnets. This spatial bias shows the importance of particle distribution in the flow as well as magnetic field geometry. These studies demonstrated the feasibility of capturing magnet particles from aerosol in airway conditions.

For retention, clearance of particles due to motion of the mucus lining of the airways must be overcome. Particle retention was studied *in vitro* using various liquids to simulate mucus and identify relevant parameters. An *ex vivo* animal tissue model was used to demonstrate feasibility. Retention of 3-5 µm diameter iron particles was achieved at reduced liquid/mucus viscosities. Larger (~100 µm) particles were retained at normal mucus viscosities. The size dependence shows that particle aggregation after deposition is crucial for effective retention.

In vitro retention experiments showed aggregate size is correlated with liquid viscosity, i.e. formation of aggregates is limited by forces opposing particle motion along the mucus layer interface. To determine these forces, particle motion on various air-liquid interfaces, chosen to simulate different mucus properties in isolation, was studied. When surfactants are present, as in the mucus layer, particle motion is limited by a velocity-dependent surface tension gradient as well as viscous drag.

Pulling particles through the mucus layer into the tissue beneath was also considered as a potential retention strategy. The force required to pull particles through the mucus layer was also studied using various liquids to simulate mucus properties. In addition to the surface tension force holding the particles at the interface, hydrodynamic forces must be overcome to pull particles into or out of a liquid film such as the mucus layer.

Acknowledgements

Thanks to my supervisor, Alidad Amirfazli; for his time, constant support, and insight. I am very grateful to have him as a mentor and for his invaluable contributions to my personal and professional development.

I am also grateful to all of the people who have helped me with technical assistance: the Mechanical Engineering workshop staff for fabricating apparatus; the staff of the University of Alberta Health Sciences Laboratory Animal Services for assistance with the frog palate speciments; Chidirim Ejim for help with the PDA measurements; Bin Lin and Hasan MD Anwarul for rheological measurements; Uwe Rietzler and Maren Müller at the MPIP for assistance with using the AFM and the SEM images of the colloidal probes, respectively.

Thanks also to Malcolm King for helpful discussions regarding the frog palate experiments, to Warren Finlay regarding particle aerosolization, and Carlos Lange regarding mucus simulants. The experiments in Chapter 6 were performed at the Max Planck Institute for Polymer Science, with the support of Hans-Jürgen Butt and Michael Kappl; thanks to them for their help and the opportunity to do this work at the MPIP. Also, Brian Fleck for his advice and encouragement.

I would like to thank my labmates for interesting talks, helpful feedback, shared frustration, and general encouragement, in particular: Andrew Milne, Mohamed Reza Shadnam, David Barona, Chidirim Ejim, and Farshid Chini.

I would also like to acknowledge the sources of funding for this work: REE, Education Abroad, University of Alberta, NSERC, and the Alberta Cancer Board.

Table of Contents

List of Tables

List of Figures

Chapter 1: Introduction

Targeted delivery of particles in the human body using magnetic fields has been an area of interest since the 1970s, when polymer-coated magnetic microparticles were first developed [1]. Magnetic targeting allows drug particles to be concentrated and held at target sites in the body using magnetic fields. Externally controlled, site-specific drug delivery would improve treatment efficacy by increasing the drug concentration at the target site, as well as decreasing the overall amount of drug required, reducing systemic toxicity and treatment cost. These benefits make magnetic targeting especially attractive for chemotherapy. Administration of chemotherapy drugs to the airways via inhaled aerosol is an ideal application for magnetic targeting due to the localized target sites and requirement to minimize dosage [2]. Chemotherapy for lung cancer by conventional inhaled aerosol drug delivery has shown promise in animal studies [2], however, its effectiveness is limited due to potential damage to healthy airway tissue. In order to develop a magnetic targeting system for inhaled aerosols, a sound understanding of the behavior of magnetic particles in the airways during deposition and retention under applied magnetic fields is required. This thesis provides that understanding on a fundamental level through *in vitro* experiments in which the basic phenomena governing magnetic aerosol particle deposition and retention are identified and characterized.

1.1 Background for magnetic targeting

1.1.1 Applications

Chemotherapy stands to benefit most significantly from magnetic targeting and has been a main focus of magnetic drug targeting research. This is because in most cases that can be effectively treated, the target sites for chemotherapy are localized. In these cases, the goal is to deliver as much drug as possible to the target site and nowhere else in the body, in order to minimize systemic toxicity of the drug. This is particularly true for lung cancer, which provides the motivation for studying magnetic targeting of inhaled aerosols.

The harmful side effects associated with chemotherapy arise from the fact that the drugs will attack healthy as well as cancerous tissue. In non-targeted delivery, the drugs circulate throughout the body, and large doses are required to build up an effective concentration in a tumor. By reducing the overall amount of drug required to deliver enough of the drug to the tumor, the effectiveness of the drug could be increased and side effects reduced. Reducing the overall amount of drug could also reduce the cost of chemotherapy. Chemotherapy drugs are among the most expensive manufactured substances, e.g. paclitaxel which costs $3,000 per gram [3]. Even a slight reduction in the amount required for treatment could lead to significant cost savings.

Various chemotherapy agents, including mitoxantron [4], doxorubicin [5], epirubicin [5], and paclitaxel [5], have been successfully coupled to magnetic carriers. Magnetic targeting of chemotherapy drugs in the circulatory system has been shown to appreciably increase drug concentration in tumors in animal studies using swine, rabbits, and rats [1]. In a study by Alexiou *et al*., the dosage of mitoxantrone required to achieve tumor remission in rabbits was reduced by 80% through magnetic targeting [4]. Although the results of these animal studies are encouraging, there has been little conclusive proof of magnetic targeting being useful in human studies to date [6]. One of the reasons for this is the increase in scale from an animal model to a human. Scaling of magnetic fields and forces must be considered when looking at the results of animal studies.

Although chemotherapy has been the main focus of magnetic targeting research, other therapies, such as anti-inflammatories and antibiotics [1] have been suggested as possible applications of magnetic targeting. As in the case of chemotherapy, these treatments would also benefit by reducing systemic exposure to the drugs used. Targeting of radioactive magnetic particles has also been suggested for cancer treatment [7]. Magnetic targeting may also be useful in enhancing diffusion-mediated processes such as gene transfection. This has been demonstrated in *in vitro* studies [8].

Magnetic particles are also used as contrast agents for magnetic resonance imaging (MRI). Magnetic particles can be concentrated in a region of the body with a magnetic field, allowing for enhanced imaging, which can in turn allow more precise delivery of drugs to the target site, e.g. by direct injection [9].

1.1.2 Magnetic Particles

Magnetic carriers can take different forms, depending on the drug to be delivered and the delivery method. These forms include ferrofluids, inorganic magnetic particles coated with a drug, magnetoliposomes, core-shell particles, and composite polymer particles.

Magnetic particles generally consist of magnetic material bonded to a drug component. The drug may be directly adsorbed to the magnetic material, bonded to a polymer coating on the magnetic material, or in solution with the liquid component of a ferrofluid. Table 1.1 gives a number of examples of drugs that have been bonded to magnetic particles. Ferrofluids are stable colloidal suspensions of magnetic particles in a liquid containing a surfactant preventing particle aggregation. Ferrofluids generally behave as magnetic liquids, and are the basis for the study of magnetohydrodynamics. Figure 1.1 illustrates these different particle configurations. Although drugs can be bonded directly to magnetic nanoparticles, the magnetic moments of nanoparticles are typically insufficient for manipulation with magnetic fields in the body. As a result, the nanoparticles must be suspended in a polymer matrix of a microparticle or a liquid (ferrofluid). Magnetic nanoparticles can also be coated with a phospholipid bilayer to form magnetoliposomes, which can be tailored for biocompatibility or functionality [10].

Table 1.1: Chemotherapy drugs coupled to magnetic particles

Drug	**Form**	**Size**	**Reference**
Doxorubicin	Albumin-coated magnetite	1-2 μm	[6]
Doxorubicin	Irregular carbon-coated iron	0.5-5 μm	[6]
Dactinomycin	Polycyanoacrylate particles	220 nm	[6]
Oxantrazole	Chitosan particles	530 nm	[6]
Methotrexate	Solid lipid	450-570 nm	[6]
Carminomycine	Ferrocarbon	100 nm	[6]
Epirubicin	Ferrofluid	100 nm	[5]

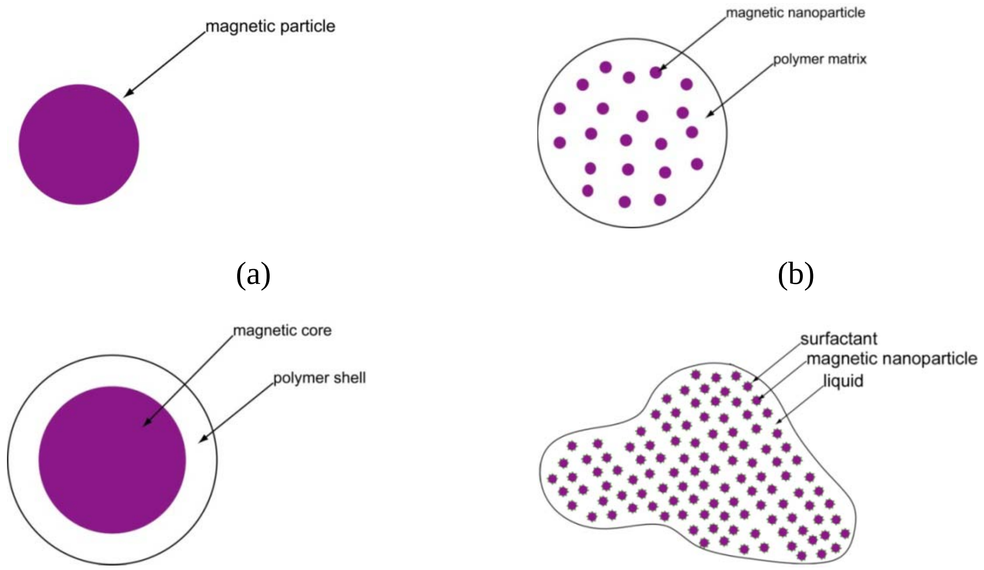

(a) (b)

(c) (d)

Figure 1.1: Various drug delivery particles: (a) a single magnetic particle onto which drugs can be directly adsorbed (b) a composite particle containing magnetic nanoparticles (c) a core-shell type particle with magnetic material encased in a polymer capsule (d) a ferrofluid consisting of magnetic particles suspended in liquid with a surfactant for stability.

Particles have also been developed which can be triggered to release drugs by magnetic fields. Polymer particles containing drugs can be manufactured with magnetite nanoparticles embedded in them that will cause the particles to rupture and release their payload when a magnetic field is applied [7]. Similar mechanisms can also be used to control the diffusion of drugs from particles [7]. Particles that are similarly responsive to oscillating fields have also been developed. This is an advantage because the particles could be guided by static fields and activated by oscillating fields [9].

1.1.3 Magnetic fields

The mechanisms of magnetically targeted drug deposition in the airways and circulatory system are similar: the magnetic field must produce forces on the particles sufficient to overcome the drag force exerted by the fluid in which the particles are entrained. In order for a field to produce a force on a particle, the field must have a gradient in addition to being sufficiently strong. A uniform magnetic field will not produce any force on a non-magnetized particle.

For drug targeting, magnetic fields are typically applied by magnets placed outside of the body. Various types of magnets may be used; typical field strengths are summarized in Table 1.2. The most common method is to use permanent magnets. Permanent magnets are a simple, cost-effective means of producing high-strength, high-gradient magnetic fields; however, careful design is required to produce the desired magnetic field geometry. Also, proper orientation of the magnetic field is necessary in order to direct the particles. Similar design considerations are expected to apply for magnetic targeting in the airways, although previous studies in the literature have focused almost exclusively on targeting systems for drug delivery via the circulatory system.

Table 1.2: Typical maximum field strengths and gradients for various magnets

Magnet type	**Field strength (T)**	**Field gradient (T/m)**
Permanent Nd-Fe-B	2	6
Bulk superconducting magnet	4.5	200
Conventional electromagnet	0.6	120
MRI electromagnet	3	0.1

Electromagnets can also be used to produce suitable gradient fields for magnetic targeting, in some cases even exceeding the strength of permanent magnet materials. Conventional electromagnets typically require liquid cooling to produce such fields. Superconducting magnets can produce fields that far exceed those achievable by permanent magnets [11]. Such magnets are much more complex and costly, however. An example of high-strength, high-gradient electromagnet system is a magnetic resonance imaging (MRI) machine. Another advantage of electromagnet systems is that the magnetic field strength and orientation can be dynamically controlled. Such control would be useful for dynamic targeting and guidance of magnetic particles, as investigated by Sylvain *et al*. for targeting magnetic particles in the liver [12].

Magnetic stents are pieces of magnetizable material, e.g. stainless steel mesh, implanted in the body to aid in trapping particles from the blood. This approach takes advantage of the fact that magnetic materials will distort a magnetic field. Even in a uniform magnetic field, the magnetized material will have a gradient field around it, which will attract magnetic particles as they pass. This is an advantage, as strong uniform magnetic fields are easier to produce with existing magnet technologies than gradient fields. The disadvantage of magnetic stents is that this approach is invasive, as the material must be implanted. Stents have been shown to be effective in *in vitro* and numerical studies of particle deposition in blood vessels [13].

Although not a drug delivery technique, magnetic particle embolization has been proposed as a method for treating tumors by blocking the blood supply to the tumor [5, 14]. Emboli blocking the blood vessels supplying a tumor can be created by using magnetic fields to form large aggregates in the blood vessels, taking advantage of the tendency of magnetized particles to mutually attract one another. This attraction occurs because, like wires in a magnetic stent, the magnetic material in the particles will distort the magnetic field, producing local gradients. A gradient field would still be required for embolization, however, in order to hold the emboli against the pressure of the blood flow. The feasibility of magnetic particle embolization has been demonstrated using *in vitro* [14] and animal models [5].

Uniform magnetic fields, although they do not produce translational forces on non-magnetized particles, may still be useful for targeting, as they do produce magnetic torque and also cause particles to aggregate. Uniform fields are considerably easier to produce over large distances than gradient fields, e.g. by Helmholz coils or magnetic circuits.

1.2 Magnetically targeted particle deposition

1.2.1 Magnetic particle deposition in the circulatory system

In magnetic drug targeting via the circulatory system, magnetic particles are injected into a vein or artery as near as possible to the target site to minimize circulation time. A magnetic field is applied to pull the particles from the blood flow to the target site and hold them there. The magnetic fields are applied using external magnets near the target sites. The magnetic force on the particles due to the magnetic field must overcome the viscous drag force of the blood flow so that the particles are not carried past or away from the target site.

Most previous studies of magnetic targeting have dealt with particles administered via the circulatory system, i.e. the particles are immersed in the blood. In the circulatory system, magnetic particle deposition and retention are similar, as in both cases, the particles are fully immersed in the blood. The problem of magnetic targeting in the airways is more complicated, as magnetic particles are deposited from an inhaled aerosol flow onto the air-liquid interface of the airway surface. As such, particle deposition and particle retention must be considered separately, and have not been addressed prior to this thesis in the literature.

1.2.2 Magnetic particle deposition in the lung

For drug delivery to the lung, the most direct route is the administration of drugs via inhaled aerosol. Inhaled aerosol drug delivery is a well-established therapeutic technique for delivering drugs to the airways and gas exchange surfaces of the lungs. There is a great deal of work in the literature on aerosol drug delivery (non-magnetically targeted). Improvements in inhaler design, instillation methods, and drug formulation have led to many potential applications of aerosol drug delivery. An overview of the mechanics of aerosol drug delivery as well as various inhaler devices is given in [15].

The potential of chemotherapy for lung cancer via a non-targeted inhaled aerosol was demonstrated by Dahl *et al*. [2] in a study of the chemopreventive effects of inhaled isoretinoin in mice. In this study, mice were initially exposed to a carcinogen, followed by regular doses of isotretinoin administered as an inhaled aerosol over 10 – 16 weeks. The dosages of retinoin were much smaller than oral dosages that had been ineffective in previous studies. At the end of the test period, the mice treated with isotretinoin showed reductions in tumor multiplicity of up to 88%. The dosages in the study had to be limited due to toxicity to the healthy snout tissue of the mice, which illustrates the requirement for targeted delivery.

Deposition of conventional inhaled aerosol particles in the conducting airways is primarily the result of inertial impaction and sedimentation. There have been many studies on prediction of where inhaled aerosol particles deposit, using statistical methods as well as direct numerical simulation, e.g. [16], [17], and [18] (all non-targeted). Various deposition models have been developed to predict aerosol deposition in the lung, based on lung geometry, fluid mechanics, and the mechanisms of particle deposition. Deposition is correlated to particle size, although due to individual variability in lung geometry and air flows, there are no general rules governing particle deposition [15]. Particle sizes are given in terms of the particle aerodynamic diameter, which is defined as the diameter of a sphere with a drag coefficient equal to that of the particle. Large particles (>10 µm diameter) will deposit in the conducting airways. Small particles (<3 µm diameter) may not deposit at all, and may simply be inhaled and exhaled. For tracheobronchial deposition, 6 µm is ideal for conventional aerosols. A comprehensive overview of inhaled aerosol drug delivery can be found in [15].

1.2.3 Magnetic aerosol particle deposition in the airways

In magnetically targeted deposition, a magnetic field is used to cause particles to deposit from an aerosol at a target site. There are few studies of magnetic aerosol particle deposition in the literature; particularly there were no studies relating to magnetic drug targeting prior to this thesis. The studies that do exist are focus on deposition in very different environments. In [19] magnetic aerosol deposition is discussed in the context of nondestructive testing and field visualization. Others have considered magnetic aerosol deposition from atmospheric flows on Mars, for the purpose of determining mineral dust composition [20]. As there is little information in the literature pertaining to magnetic targeting in the airways, fundamental studies are required in order to demonstrate the feasibility of such a strategy and to understand the factors governing particle deposition in the airways.

For design of a magnetic aerosol targeting system, numerical modeling will also play an important role. A numerical model of magnetic particle deposition in the airways would allow magnets to be designed and evaluated by simulation. This would allow for testing and optimization of magnet designs. A numerical model of particle deposition would require information about the magnetic field and air flow to determine particle deposition. This information could come from finite element models, computational fluid dynamics data, or experimental data. As there is virtually no data relating to magnetic aerosol deposition in the airways available in the literature, experimental verification of such a numerical deposition model is also required.

Factors that are important for magnetic targeting in the circulatory system, such as fluid flow velocity, field gradient, and magnet positioning, are also expected to be important for magnetic aerosol deposition. As a first step, a simplified model of the airway is required to clearly identify the role played by each of these factors. A simple airway model would also lend itself to verification of a numerical model. Given the practical difficulties in producing magnetic fields over large distances, such a model should be based on the conditions in the trachea to demonstrate feasibility, as this is the largest airway and would represent the ‘worst-case’ situation for particle deposition.

Chapter 2 of this thesis is the first study of magnetic aerosol deposition for drug delivery in airway conditions [21]. More recently, others have considered magnetic aerosol deposition for drug delivery, although these studies have considered different scales [22] and different targeting approaches [23, 24]. Dames *et al*. studied particle deposition in mouse lungs [22]. Although [22] demonstrated successful magnetic targeting, with preferential deposition in one lung over another, the use of an animal model provides little insight into the mechanism of particle deposition. Also, the scale of the mouse model is much smaller than that of the human airway; as such, the results of [22] do not demonstrate the feasibility of magnetic targeting on a human scale. In [23] and [24], uniform magnetic fields were used to cause rod-shaped magnetic particles to deposit by changing their alignment with respect to the air flow in a model human airway. Deposition in the small airways was studied in [23] using an *in vitro* model based on the terminal bronchioles in the lung. The model airways were 0.5 mm in diameter, with parent generations 8 mm long and daughter branches 2 mm long. The model bifurcating airways were assembled with the final apparatus containing 126 parent airways, with a total flow rate of 22 L/minute for inhalation. This method achieved only marginal particle deposition (<5%), and was only considered for the terminal bronchioles, i.e. small airways.

1.3 Magnetic particle retention

1.3.1 Airway surface characteristics

The airway surface is protected from inhaled particles like dust, bacteria, and other contaminants by a layer of mucus that is propelled toward the mouth by ciliated epithelium. Particles depositing in the airways are cleared by this mechanism, which must be counteracted by magnetic forces for effective targeted inhaled aerosol drug delivery.

The airway surface lining consists of a layer of thick, viscoelastic mucus that flows on a watery periciliary layer, as shown in Figure 1.2. The cilia on the epithelium beat within the periciliary layer, and their tips engage the mucus layer, propelling it up the airways. The cilia frequencies are synchronized by the hydrodynamics of the cilia beating next to one another. The elasticity of the mucus allows the tips of the cilia to ‘grab’ the mucus layer and push it. The viscoelastic properties of airway mucus are crucial for the functioning of the mucociliary clearance mechanism. If the mucus is too thick or too thin, the clearance mechanism will not function.

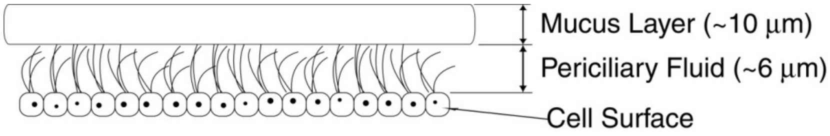

Figure 1.2: Schematic of the airway surface lining in the trachea.

For effective drug targeting in the airways, retention of particles at a target site is as important as deposition. In order for magnetic particles to be retained in the airways, the magnetic force on the particles must overcome the forces from the mucus clearance mechanism. For particles to be retained there are two possible mechanisms. First, particles may be pulled in direct opposition to the mucus flow and held. Second, the particles could be pulled into the mucus layer. In the second case, particle clearance may be overcome by either the particles penetrating the mucus layer, or by the particles simply pushing on the cilia, disrupting their function.

The mucus layer in normal tracheobronchial airways is 5 – 10 μm thick and the periciliary layer 5 – 7 μm thick [25]. This thickness of the mucus layer can vary dramatically in response to various pulmonary conditions. In healthy adults, the tracheal mucus velocity is approximately 7 – 10 mm/min [26]. The mucus velocity is lower in smaller airways, and changes depending upon the health of the airways. The continuity of the mucus layer also varies throughout the airways, as does the number of cilia [27]. For drug delivery purposes in the first generations of the airways, however, it is reasonable to assume particle deposition upon a continuous layer of mucus.

The viscoelasticity of the mucus is determined by the bonds between molecules, and can be disrupted by various chemical agents called mucolytics. Mucolytics are used to treat conditions such as chronic obstructive pulmonary disease. Temporary disruption of mucociliary clearance at a target site in the airways using mucolytics could enhance the effectiveness of magnetic fields in retaining particles.

Prior to this work, there have been no previous studies related to the use of magnetic fields to retain particles in the airways. As such, an understanding of the basic factors determining whether or not particles are retained is required. Although similar considerations as for particle deposition and retention in the circulatory system will apply, retention in the airways is complicated by the fact that the particles will be pinned at the air-liquid interface of the mucus layer (rather than being immersed in a liquid). There is little relevant data in the literature about the behavior of particles at interfaces in these conditions. As a first step, two types of studies are needed: first, the large-scale behavior of particles depositing from aerosol must be studied to determine if retention is feasible and, if so, under what conditions. Secondly, the small-scale (local) behavior of individual particles must be investigated to understand the mechanisms of particle retention.

For both the large-scale and small-scale magnetic particle retention studies, suitable experimental platforms are required. As magnetic particle retention in the airways has not been previously studied, existing platforms used in other types of studies must be adapted, or new ones developed. The purpose of the large-scale experiments is to realistically model magnetic aerosol particle deposition and retention at the airway surface. This will allow the feasibility of magnetic particle retention to be evaluated, and allow the study of retention of a large amount of deposited particles. A model airway surface that allows for realistic particle deposition as well as the control of parameters of interest, such as simulated mucus viscosity, surface tension, is required. A realistic model airway surface is also required to demonstrate the feasibility of particle retention. The purpose of the small-scale experiments is to understand the mechanisms governing the retention of individual particles. Surface uniformity is also important to allow for repeatable microscopic measurements of individual particles. As for the large scale experiments, the ability to control parameters of interest such as simulated mucus viscosity and surface tension is also necessary.

1.3.2 Airway surface models

1.3.2.1 Large scale models

Animal tissue models have been used to provide realistic models of functioning airway tissue [28]. *In vivo* animal models have been used to study mucus properties and mucociliary transport rates in large mammals, e.g. dogs and horses [28]. In such experiments, mucus transport is either measured based on the quantity of mucus collected over a set time, or observed *in situ* using tracer particles and a fibroscope [28]. For initial studies of magnetic particle retention, *in vivo* models are not useful, as there would be significant difficulties in observing particle transport and precisely applying magnetic fields.

Ex vivo animal models have also been used to study mucociliary clearance [29]. Typically these models consist of bullfrog (*Rana catesbeiana*) or leopard frog (*Rana pipiens*) palates. Frog palate models have been used to study the effect of mucus properties and other parameters on mucus transport rates, which can be measured using tracer particles, as in the *in vivo* platform, but without the requirement of a fibroscope. The tissue sample size of the frog palate model is small enough that the sample and observed regions can be precisely positioned in a magnetic field. As such, the frog palate platform provides a suitable, realistic experimental model of mucus transport that can be used to evaluate the feasibility of magnetic particle retention at the airway surface.

In addition to animal model studies, *in vitro* studies are also essential to understand the factors governing particle retention, since parameters such as mucus viscoelasticity and flow rate cannot be easily or precisely controlled in animal tissue models. Most previous *in vitro* studies of the behavior of the airway surface liquid have dealt with mucus clearance due to coughing [30]. In these experiments, the mucus was simulated by a stationary layer of liquid in a channel. In [30] the mucus layer was simulated by a single layer of a locust bean gum-based mucus simulant. A similar experimental platform could be used to study mucus clearance in a model airway. In order to simulate mucus clearance by mucociliary transport, liquid flow is required. This has not been implemented in previous models. A single flowing layer of liquid could serve as model of mucus clearance, and would allow the liquid properties to be controlled. Due to the complexity of the mucus properties, a variety of liquids must be used to understand the various aspects of mucus behavior e.g. viscoelasticity, surface tension, etc.

1.3.2.2 Small-scale models

Due to their non-uniformity, animal tissues are unsuitable for studying the microscopic motion of particles. Studies of the motion of microscopic tracer particles have been performed in the literature using realistic airway tissue models produced using cultured tissue [31]. In cultured tissue models, functional airway epithelium is grown *in vitro* from human lung cells. When grown under appropriate conditions, the culture will develop ciliated epithelium with mucus and periciliary layers. Multiple culture specimens must be grown, as not all will exhibit coordinated ciliary activity resulting in mucus transport (25% in [31]). Although the cultured tissue model provides a realistic model airway surface and mucus layer, as with animal models, precise control of the mucus properties is not possible. Since the goal of the small-scale studies is mechanistic understanding rather than demonstrating feasibility, these models are not suitable for the experiments in this thesis.

Magnetic particles in the airways will be initially deposited at the air-liquid interface of mucus layer. As such, fundamental understanding of particle behavior at air-liquid interfaces is necessary in order to develop an effective approach for magnetic particle retention. Particles at air-liquid interfaces can be studied in a variety of configurations. Microscopic studies have used trajectory analysis of particles to study particle motion at interfaces due to capillary force [32] and Brownian motion [33]. Similar trajectory analysis studies could be performed to study particle behavior at interfaces in a magnetic field. Particle behavior at interfaces has also been studied at the interfaces of droplets and bubbles using the colloidal probe technique [34]. In this method, particles are attached to micromachined cantilevers and their interactions with interfaces measured using an atomic force microscope. Such experiments can be used to study the motion of particles being pulled through the mucus layer. As in the large scale *in vitro* experiments, various liquids are necessary to obtain a complete picture of mucus behavior.

1.3.3 Microscopic (local) particle behavior at the airway surface

Unlike the case of particle deposition, in which the drag force on individual particles in aerosol can be calculated from the Stokes drag equation, precise prediction of the behavior of individual particles at air-liquid interfaces is difficult. Fundamental studies of the mechanisms of particle retention are also necessary because the behavior of particles at the airway surface is not captured by existing theoretical models as it is for particle deposition. Particles in the airways will, at least initially, deposit at the air-liquid interface of the mucus layer. The motion of particles at air-liquid interfaces is not well understood. In order to develop an understanding of particle motion at the interface of a complex liquid such as airway mucus, model studies with simplified systems are necessary. The experiments presented in Chapters 3 - 6 of this thesis are the first such studies of particle motion at air-liquid interfaces performed for the purpose of using magnetic fields to overcome mucociliary clearance in the airways.

Particle motion at the interface can be broken into two components: parallel to the interface, and perpendicular (into or out of) the interface. Both components are expected to play significant roles in particle retention. The parallel component will determine the magnetic field strength required to hold particles against the flow of mucus as well as the effect of interparticle interactions. The perpendicular component of particle motion will determine whether or not the particles can penetrate the mucus layer.

Particle motion along the air-liquid interface in the airways will be subject to viscous drag as well as resistance due to a layer of surfactant on the mucus.

The mucus in airways has a layer of surfactant that reduces its surface tension [35]. The surfactant will cause an additional force resisting the motion of a particle along the air-liquid interface of the airways. Figure 1.3 shows a solid particle moving along an interface with surfactant molecules spread at the interface. As the particle moves, it dilutes the surfactant concentration in its wake [36]. This results in a surface tension gradient across the particle, with higher surface tension in the particle wake than in front of the particle. The surface tension gradient produces an additional resisting force opposing the particle motion (this is sometimes called the surface pressure acting on a particle). The extent of this effect depends upon the particle speed, and the diffusivity of the surfactant, as diffusion acts to restore the uniform distribution of surfactant after it is disrupted by the particle [36].

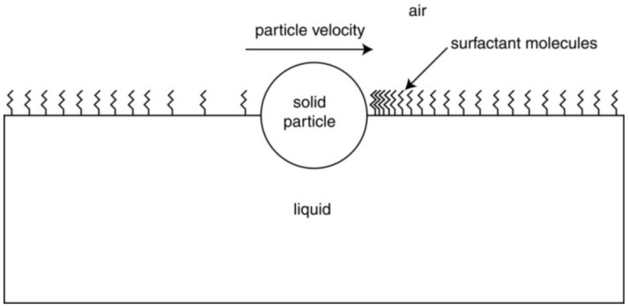

Figure 1.3: Surfactant distribution around a particle moving at an air-liquid interface. The imbalance of surfactant in the immediate vicinity of the particle gives rise to a force resisting particle motion, in addition to viscous drag.

Theoretical models of surfactant resistance to particle motion have approximated surface tension gradient effects using constant surface shear and dilatational viscosities [37]. The use of constant terms neglects the mechanistic basis for the additional resistance due to surfactants. There is no experimental verification of the validity of this approximation in the literature. As there has been little experimental work in this area, and because the theoretical models have not been tested in airway-relevant conditions, experimental studies are required to measure the drag force on particles at air-liquid interfaces.

The particles upon landing on the mucus layer most likely will be partially immersed, depending on the particle wetting characteristics, and the viscosity and thickness of the mucus layer. To determine the magnetic force required to hold partially immersed particles in place against the flow of mucus, the appropriate drag coefficient must be determined. This requires understanding of the wetting properties of the particles used [37], i.e. the particle contact angle with the mucus layer.

Schürch *et al*. have studied the wetting behavior of particles at the air-liquid interfaces of the airways extensively [35]. Their findings have shown that small particles will tend to be highly immersed in the mucus layer, whereas large particles (> 10 µm diameter) will protrude. These findings suggest that nanoparticles may be completely engulfed in the mucus layer, but larger particle aggregates will straddle the interface. Since the majority of particles will deposit as aggregates, the latter case is more appropriate to consider.

A possible approach to particle retention is to use magnetic fields to pull particles through the mucus layer into the tissue beneath, thereby avoiding mucus clearance. The feasibility of this approach will depend on the force required to pull the particles from the air-liquid interface of the mucus layer. The adhesion force between particles and air-liquid interfaces has been studied previously in [38] as a measure of interfacial tension, and in [39]. Previous studies have focused on the force required to remove particles from bubbles or droplets, however, not liquid films. When the liquid is in a confined configuration such as mucus layer, hydrodynamic effects may affect the force required to pull particles through the air-liquid interface. Given the complex properties of mucus, experiments using different liquids to model various aspects of mucus (viscosity, surfactant layer, elasticity) are required to determine the force required to pull particles through the air-liquid interface in the airways.

1.4 Thesis objectives

In order to develop a practical magnetically targeted drug delivery system, a detailed understanding of the mechanisms of magnetic particle deposition and retention in the airways is necessary. The purpose of this thesis is thus to provide this understanding by investigating the mechanisms of particle deposition and particle retention. The objectives of this thesis are as follows:

1. Demonstrate, using an *in vitro* model airway, the feasibility of capturing magnetic particles from an aerosol in simulated airway conditions.
2. Determine relevant parameters that govern particle deposition and retention in simulated airway conditions using *in vitro* and *ex vivo* models. Identify relevant factors that play a role in particle deposition and retention.

3. Evaluate the effectiveness of using mucolytics to enhance magnetic particle retention in the airways using an *ex vivo* frog palate model of the airway surface
4. Measure the surface drag force on particles at air-liquid interfaces using various liquids to simulate the properties of airway mucus
5. Determine the magnetic force required to pull a particle through the air-liquid interfaces of various liquids chosen to simulate the properties of airway mucus.

A schematic showing the structure of this work is shown in Figure 1.4. Particle deposition was studied using numerical and experimental models, which yielded particle collection efficiency data for various magnetic fields (Chapter 2). These results showed the importance of the magnetic field gradient, particle concentration and distribution within the aerosol flow, and particle aggregation for effective deposition.

Particle retention was studied using *in vitro* and animal tissue (frog palate) experimental models (Chapter 3). Analysis of the image data from these experiments indicated that stronger magnetic fields were required for retention than for deposition. The results of the particle retention studies also showed that mucus viscosity is the main determinant of particle retention, due to a direct relationship between particle aggregation and mucus viscosity. The possibility of reducing mucus viscosity using mucolytics was studied using the animal tissue model (Chapter 4). In order to study the limiting factors on particle aggregation, additional experiments were performed to measure the drag force on particles moving along air-liquid interfaces (Chapter 5). The retention results also suggested the strategy of pulling particles through the mucus layer to avoid clearance. This potential of such a strategy was evaluated using atomic force microscope tensiometry (Chapter 6).

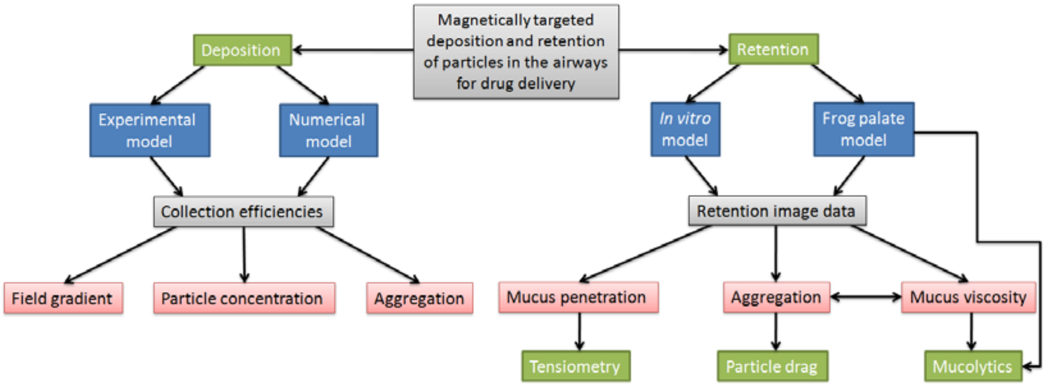

Figure 1.4: Schematic overview of this thesis.

1.5 Scope

In this thesis, only deposition and retention of magnetic aerosol particle in the conducting airways is considered. Other aspects of magnetic aerosol drug targeting such as delivery, dosage, and administration of drugs to the deep (alveolar) regions of the lung are not considered. Inhaled aerosol drug delivery methods have been studied extensively in the literature. As these methods apply to magnetically susceptible particles as well as conventional particles, the focus of this thesis is on magnetic particle deposition and retention, which have not been previously studied. Delivery to the alveolar regions of the lung is also not considered here. In the case of lung cancer, cancers in this region are less treatable by chemotherapy. Also, delivery through the deep lung requires the aerosol to pass through many generations of the airways. Given that magnetic particle deposition in the airways has not been extensively studied, the simpler case of the conducting airways (i.e. the first several generations) is considered here.

The goal of this thesis is to identify the forces affecting magnetic particle motion and factors governing their deposition and retention, as this information is absent in the literature. This is accomplished through the use of various *in vitro* models to simulate conditions in the airways and at the airway surface. In keeping with this goal, the experimental models were designed to allow the particle behavior to be observed and explained rather than to produce a realistic clinical model. Identifying particle behavior using clinically realistic models is beyond the scope of this thesis. Although such models, e.g. animal models, may make some aspects of the results more realistic, they would considerably increase the difficulty in understanding the forces affecting particles as there would be too many uncontrolled variables and individual aspects of particle behavior could not be isolated.

Similarly, the practical design of a magnetic targeting system and magnetic particles are also beyond the scope of this thesis. As described above, there are a variety of methods for producing magnetic fields in the body and types of magnetic particles available. Choosing from these alternatives requires knowledge of the forces that must be exerted on the particles for successful deposition and retention. This thesis provides the necessary understanding of particle deposition and recognition mechanisms for a magnetic targeting system to be designed.

1.6 References

1. Pankhurst, Q.A., Connolly, J. and Dobson, S.K., 2003. Applications of magnetic nanoparticles in biomedicine. J. Phys. D: Appl. Phys., Vol. 36, pp. R167-R181.

2. Dahl, A.R., *et al*. 2000. Inhaled isotretinoin (13-cis retinoic acid) is an effective lung cancer chemopreventive agent in A/J mice at low doses: A pilot study. Clin. Cancer Res., Vol. 6, pp. 3015-3024.

3. Suffness, M. Taxol: Science and Applications. London, UK : CRC Press, 1995.

4. Alexiou, C., *et al*. 2006. Targeting cancer cells: magnetic nanoparticles as drug carriers. Eur. Biophys. J., Vol. 35, pp. 446-450.

5. Lübbe, A.S. and Alexiou, C., Bergemann, C. 2001. Clinical applications of magnetic drug targeting. J. Surg. Res, Vol. 95, pp. 200-206.

6. Hafeli, U.O. and Chastellain, M. Magnetic nanoparticles as drug carriers. [book auth.] V.P. Torchilin. Nanoparticulates as Drug Carriers. London, UK : Imperial College Press, 2006, pp. 397-418.

7. Magnetically modulated therapeutic systems. Hafeli, U.O. 2003, Int. J. Pharm., Vol. 277, pp. 19-24.

8. Plank, C. 2008. Nanomagnetosols: magnetism opens up new perspectives for targeted aerosol delivery to the lung. Trends in Biotech., Vol. 26, pp. 59-63.

9. Amirfazli, A. 2007. Magnetic nanoparticles hit the target. Nat. Nanotechnol., Vol. 2, pp. 467-468.

10. Marcela, G. and Kannan, K.M. 2005. Synthesis of magnetoliposomes with monodisperse iron oxide nanocrystal cores for hypothermia. J. Magn. Magn. Mater., Vol. 293, pp. 265-270.

11. Takeda, S., *et al*. 2007. Development of magnetically targeted drug delivery system using superconducting magnet. J. Magn. Magn. Mater., Vol. 311, pp. 367-371.

12. Automatic transport of magnetic particles in the blood vessels using a clinical MRI system. Sylvain, M. Vancouver, Canada, 2008. 7th Int. Conf. Sci. Clin. Appl. Magn. Carriers, May 21-24.

13. Aviles, M.O., Ebner, A.D. and Ritter, J.A. 2008. Implant assisted-magnetic drug targeting: Comparison of in vitro experiments with theory. J. Magn. Magn. Mater., Vol. 320, pp. 2704-2713.

14. Liu, J., Flores, G.A. and Sheng, R. 2001. In-vitro investigation of blood embolization in cancer treatment using magnetorheological. J. Magn. Magn. Mater, Vol. 225, pp. 209-217.

15. Finlay, W.H. The Mechanics of Inhaled Pharmaceutical Aerosols: An Introduction. London : Academic Press, 2001.

16. Matida, E.A., *et al*. 2004. Improved numerical simulation of aerosol deposition in an idealized mouth-throat. J. Aerosol Sci., Vol. 35, pp. 1-19.

17. Moskal, A. and Gradoń, L. 2002. Temporary and spatial deposition of aerosol particles in the upper human airways during breathing cycle. J. Aerosol Sci., Vol. 33, pp. 1525-1539.

18. Goo, J. and Kim, C.S. 2003. Theoretical analysis of particle deposition in human lungs considering stochastic variations of airway morphology. J. Aerosol Sci., Vol. 34, pp. 585-602.

19. Dikanskii, Y.I. and Kiselev, V.V. 1998. Magnetosensitive aerosols and prospects of their application. Magnetohydrodynamics, Vol. 34, pp. 212-215.

20. Merrison, J., *et al*. 2002. Simulation of the martian aerosol at low wind speeds. J. Geophys. Res., Vol. 107, pp. 16.1-16.8.

21. Ally, J., Martin, B., Khamesee, M.B., Roa, W., Amirfazli, A. 2005. Magnetic targeting of aerosol particles for cancer therapy. J. Magn. Magn. Mater., Vol. 293, pp. 442-449.

22. Dames, P., *et al*. 2007. Targeted delivery of magnetic aerosol droplets to the lung. Nat. Nanotechnol., Vol. 2, pp. 495-499.

23. Martin, A.R. and Finlay, W.H. 2008. Alignment of Magnetite-Loaded High Aspect Ratio Aerosol Drug Particles with Magnetic Fields. Aerosol Sci. and Tech., Vol. 42, pp. 295-298.

24. Martin, A.R. and Finlay, W.H. 2008. Enhanced deposition of high aspect ratio aerosols in small airway bifurcations using magnetic field alignment. Aerosol Sci., Vol. 39, pp. 679-690.

25. Sleigh, M.A., Blake, J.R. and Liron, N. 1988. The propulsion of mucus by cilia. Am. Rev. Respir. Dis., Vol. 137, pp. 726-741.

26. Morgan, L., *et al*. 2004. Scintigraphic measurement of tracheal mucus velocity in vivo. Eur. Respir. J., Vol. 23, pp. 518-522.

27. Martin, D.E. and Youtsey, J.W. Respiratory Anatomy & Physiology. St. Louis, USA : The C.V. Mosby Company, 1988.

28. King, M. 1998. Experimental models for studying mucociliary clearance. Eur. Respir. J., Vol. 11, pp. 222-228.

29. Rubin, B.K., Ramirez, O. and King, M. 1990. Mucus-depleted frog palate as a model for the study of mucociliary clearance. J. Appl. Physiol., Vol. 69, pp. 424-429.

30. King, M., Brock, G. and Lundell, C. 1985. Clearance of mucus by simulated cough. Journal of Applied Physiology, Vol. 58, pp. 1776-1782.

31. Matsui, H., *et al*. 1998. Coordinated clearance of periciliary liquid and mucus from airway surfaces. J. Clin. Invest., Vol. 102, pp. 1125-1131.

32. Petkov, J.T., *et al*. 1995. Measurement of the drag coefficient of spherical particles attached to fluid interfaces. J. Colloid Interface Sci., Vol. 172, pp. 147-154.

33. Sickert, M., Rondelez, F. and Stone, H.A. 2007. Single-particle Brownian dynamics for characterizing the rheology of fluid Langmuir monolayers. Europhysics Letters, Vol. 79, pp. 66005-p1-p6.

34. Bonaccurso, E., Kappl, M. and Butt, H-J. 2008. Thin liquid films studied by atomic force microscopy. Curr. Opin. Colloid Interface Sci., Vol. 13, pp. 107-119.

35. Schürch, S., *et al*. 1999. Particles at the airway interfaces of the lung. Colloids and Surfaces B, Vol. 15, pp. 339-353.

36. Dimitrov, K., Avramov, M. and Radoev, B. 1994. Brownian motion at liquid-gas interfaces. 3. Effect of insoluble surfactants. Langmuir, Vol. 10, pp. 1596-1599.

37. Danov, K., *et al*. 1995. Influence of the surface viscosity on the hydrodynamic resistance and surface diffusivity of a large Brownian particle. Journal of Colloid and Interface Science, Vol. 175, pp. 36-45.

38. Scheludko, A.D. and Nikolov, A.D. 1975. Measurement of surface tension by pulling a sphere from a liquid. Colloid and Polymer Science, Vol. 253, pp. 396-403.

39. Pitois, O. and Chateau, Xavier. 2002. Small Particle at a Fluid Interface: Effect of Contact Angle. Langmuir, Vol. 18, pp. 9751-9756.

Chapter 2: Magnetic targeting of aerosol particles for cancer therapy[*]

In this chapter, an *in vitro* methodology is used to examine the feasibility of targeted delivery of chemotherapeutic agents as an inhaled aerosol to the tracheobronchial region of the lung. In most treatable cases of lung cancer, the cancer occurs in the tracheobronchial region [1]. A numerical model of aerosol particle motion in a magnetic field was also developed to predict the targeting pattern of aerosol particles.

In chemotherapy, cytotoxic drugs are used to kill cancerous cells. These drugs are currently administered intravenously or orally. Generally, combinations of chemotherapy and other drugs are used to mitigate adverse side effects, e.g. skin, gastrointestinal, and bone marrow ailments. Such side effects are inevitable, because the drugs used are toxic to healthy cells as well as cancer cells, and circulate throughout the body.

By delivering chemotherapeutic agents for lung cancer as a magnetically targeted aerosol, it may be possible to reduce adverse side effects by administering chemotherapy agents directly to the cancerous tissue. With a properly designed magnetic targeting system, the drug particles would be guided to the cancerous tissue by an appropriate magnetic field. The magnetic field also would have to be strong enough to overcome mucociliary clearance. Studies have shown that up to 95% of particles (6.5 μm diameter) deposited in the tracheobronchial region are removed by mucociliary clearance [2].

---

[*] A version of this chapter has been published. Ally, Martin, Khamesee, Roa, Amirfazli 2005. Journal of Magnetism and Magnetic Materials. 293: 442-449.

There is hardly any information available for magnetic targeting of inhaled aerosol particles. Dikanskii and Kiselev considered the concept in the context of nondestructive testing and magnetic field visualization [3], although some methodological aspects are absent in their work. Others have considered magnetic aerosol deposition from atmospheric flows on Mars, for the purpose of determining mineral dust composition [4]. There is no information available in the literature regarding clinical applications.

In contrast to the concept of clinical applications for magnetically susceptible aerosols, magnetically targeted particles administered intravenously have been investigated in the past twenty five years. The works by Lübbe *et al*. [5] and Goodwin *et al*. [6] are examples of magnetic targeting *in vivo* to deliver drug particles to tumors. Others, such as Liu *et al*. [7], have investigated the use of magnetic particles for blood embolization. Factors affecting magnetic targeting identified in these works, such as fluid flow velocity, field gradient, and magnet positioning, should also be considered for aerosol targeting.

The first step in the development of a magnetic targeting system for lung cancer is to characterize the deposition of aerosols in simulated conditions of the tracheobronchial region. This was done *in vitro* using a bench top model. In order to facilitate future development of the system, a numerical simulation of particle deposition was also developed and verified using the experimental results. The current work represents a necessary initial step in the development of a magnetic targeting system, and as such, the fundamentals and possibilities of targeted deposition and retention of magnetic aerosol particles in an idealized model representing the conducting airways is considered.

2.1 Theoretical Background

Inhaled aerosols consist of fine particles suspended in air: the flow of air around the particles is characterized by the particle Reynolds number, *Re*. The Reynolds number describes the ratio of the magnitudes of the inertial and viscous forces on the particle. For small Reynolds numbers (*Re*<0.5), the drag force $\vec{\boldsymbol{F}}_{\boldsymbol{D}}$ on a particle is purely due to viscosity, and can be calculated using the Stokes expression for drag force on a sphere as:

$$\vec{\boldsymbol{F}}_{\boldsymbol{D}} = 3\pi\mu d\left(\vec{\boldsymbol{v}}_{\boldsymbol{f}} - \vec{\boldsymbol{v}}_{\boldsymbol{p}}\right) \quad (2.1)$$

where μ is the viscosity of air, *d* is the particle diameter, $\vec{\boldsymbol{v}}_{\boldsymbol{f}}$ is the air velocity, and $\vec{\boldsymbol{v}}_{\boldsymbol{p}}$ is the particle velocity. For the air flow (0.34 m/s) and particles (1 to 3 μm diameter) used in these experiments, the particle Reynolds number was less than 0.1, so the Stokes drag equation shown was applicable.

The magnetic force, $\vec{\boldsymbol{F}}_{\boldsymbol{M}}$, on a small sphere in a nonmagnetic fluid can be calculated as:

$$\vec{\boldsymbol{F}}_{\boldsymbol{M}} = \frac{1}{2}\mu_0 \chi V_p \nabla(\vec{\boldsymbol{H}}^{\boldsymbol{2}}) \quad (2.2)$$

where μ_0 is the permeability of free space, χ is the magnetic susceptibility of the particle, V_p is the particle volume, and $\vec{\boldsymbol{H}}$ is the magnetic field intensity [8].

In aerosols, the density of the particles is typically much higher than that of air, so the buoyancy force can be neglected. Lift is also neglected, as the air velocity can be assumed constant over the particle diameter. Consequently, application of Newton's second law yields the following force balance for a particle:

$$m\frac{d\vec{\boldsymbol{v}}_{\boldsymbol{p}}}{dt} = \vec{\boldsymbol{F}}_{\boldsymbol{M}} + m\vec{\boldsymbol{g}} + \vec{\boldsymbol{F}}_{\boldsymbol{D}} \qquad (2.3)$$

where m is the particle mass, $\vec{\boldsymbol{g}}$ is acceleration due to gravity, and $\vec{\boldsymbol{v}}_{\boldsymbol{p}}$ is the velocity of the particle. Substituting Eqs. (2.1) and (2.2) into (2.3) and considering $\frac{m}{\rho_p} = V_p$ and $\nabla(\vec{\boldsymbol{H}}^{\boldsymbol{2}}) = 2\vec{\boldsymbol{H}}\nabla\vec{\boldsymbol{H}}$ results in the following expression:

$$\frac{m}{3\pi\mu d}\frac{d\vec{\boldsymbol{v}}_{\boldsymbol{p}}}{dt} = \frac{m}{3\pi\mu d}\left(\frac{\mu_0\chi}{\rho_{\boldsymbol{p}}}\vec{\boldsymbol{H}}\nabla\vec{\boldsymbol{H}} + \vec{\boldsymbol{g}}\right) + (\vec{\boldsymbol{v}}_{\boldsymbol{f}} - \vec{\boldsymbol{v}}_{\boldsymbol{p}}) \qquad (2.4)$$

where ρ_p is the particle density and t is time. Defining a time constant τ as $\frac{m}{3\pi\mu d}$, the equation of motion for a single particle can be written as:

$$\tau\frac{d\vec{\boldsymbol{v}}_{\boldsymbol{p}}}{dt} = \tau\left(\frac{\mu_0\chi}{\rho_{\boldsymbol{p}}}\vec{\boldsymbol{H}}\nabla\vec{\boldsymbol{H}} + \vec{\boldsymbol{g}}\right) + (\vec{\boldsymbol{v}}_{\boldsymbol{f}} - \vec{\boldsymbol{v}}_{\boldsymbol{p}}) \qquad (2.5)$$

In the numerical model developed, described in the next section, the motion of a particle is analyzed by discretization into small elements. For a single element, $\vec{\boldsymbol{H}}\nabla\vec{\boldsymbol{H}}$ can be taken as a constant. The fluid velocity can similarly be assumed constant over an element. The solution to Eq. (2.5) over an element is thus:

$$\vec{\boldsymbol{v}}_{\boldsymbol{p}} = \left[\vec{\boldsymbol{v}}_f + \tau\left(\frac{\mu_0\chi}{\rho_{\boldsymbol{p}}}\vec{\boldsymbol{H}}\nabla\vec{\boldsymbol{H}} + \vec{\boldsymbol{g}}\right)\right]\left(1-e^{-\frac{t}{\tau}}\right) + \vec{\boldsymbol{v}}_{\boldsymbol{p,0}}e^{-\frac{t}{\tau}} \quad (2.6)$$

where $\vec{\boldsymbol{v}}_{\boldsymbol{p,0}}$ is the initial velocity of the particle. For a 1 μm iron particle in air at standard temperature and pressure, $\tau = 0.024$ ms; the time steps used in the numerical model were 1 ms, two orders of magnitude larger. Therefore, the time dependent terms in (2.6) can be neglected, and the particle velocity is given by equation (7):

$$\vec{\boldsymbol{v}}_{\boldsymbol{p}} = \vec{\boldsymbol{v}}_f + \tau\left(\frac{\mu_0\chi}{\rho_{\boldsymbol{p}}}\vec{\boldsymbol{H}}\nabla\vec{\boldsymbol{H}} + \vec{\boldsymbol{g}}\right) \quad (2.7)$$

The second term of Eq. (2.7) represents the magnetic and gravitational forces on the particle, and is proportional to d^2 since $\tau = \frac{m}{3\pi\mu d} = \frac{\rho_p}{18\mu}d^2$.

The theoretical model described above considers only the motion of individual particles, and for simplicity, neglects particle interactions due to magnetization or electrical charges on the particles. Magnetic interactions would cause the particles to be attracted to each other, forming aggregates. Electrical charges would have the opposite effect, causing the particles to repel. These interactions would affect the size distribution of particles in the flow as they respectively promote and oppose the formation of aggregates. The effects of humidity are similarly not considered here. In the airways, the relatively humidity would be near 100%. This would result in stronger attachment of particles in aggregates due to capillary forces, and possibly screening of electric charges on the particles. For the particle density in the aerosol flow considered here, it is sufficient, as a first approximation, to consider only individual, non-interacting particles as in this model.

2.2 Numerical Model

A particle tracing code was developed to predict the trajectories of an initial distribution of particles representing the particle distribution in the experiments. The trajectories of the particles over discrete time steps of 1 ms were established using the second order Runge-Kutta method. The particle velocity $\vec{v}_p(\vec{x})$ was calculated using Eq. (2.7) with values of $\vec{H}$, $\nabla\vec{H}$ and $\vec{v}_f$ at each position $\vec{x}$. The magnetic field strength $\vec{H}$ was determined using finite element analysis, described below. The fluid velocity $\vec{v}_f$ was determined experimentally (see next section) and used as input for the code. The trajectories were used to predict the collection efficiencies of the magnets used in the experiments.

Finite element analysis was performed using the ANSYS finite element package to determine the magnetic field for the apparatus. Ten node quadratic tetrahedral elements were used to solve for the magnetic scalar potential at the nodes. The field intensities at the element centroids were computed by taking the gradient of the magnetic scalar potential numerically. The permanent magnets (25.4 mm diameter, 3.2 mm thick, neodymium-iron-boron) were modeled in a 100 × 200 × 500 mm air volume (see Figure 2.1). The size of the air volume required to obtain accurate results was determined by comparing results of the finite element analysis with different air volume sizes to flux values measured for a single permanent magnet (see Figure 2.2). Magnetic flux measurements were performed with a gaussmeter (F.W. Bell Model 5080).

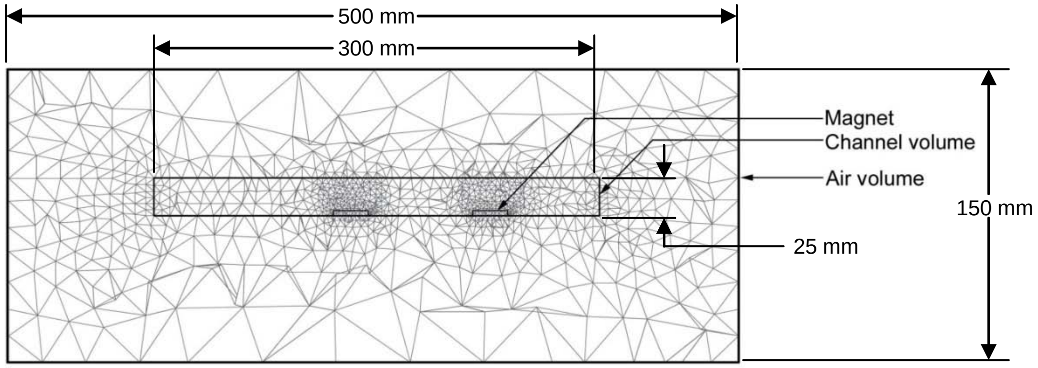

Figure 2.1: Finite element mesh for the experimental apparatus in the two permanent magnet configuration.

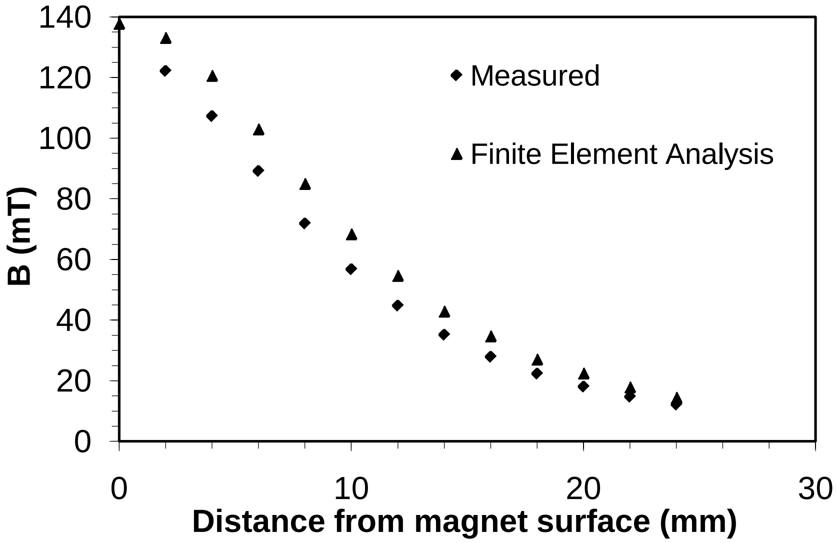

Figure 2.2: Comparison of finite element results and measured values for magnetic flux perpendicular to permanent magnet face along center axis.

A 25 × 50 × 300 mm air volume was defined within the larger air volume (see above) to represent the aerosol channel of the experimental apparatus (see Figure 2.1). At the upper surface of the smaller volume, where the magnetic field gradient is small, element size was 10 mm. At the surface of the magnets, 0.5 mm elements were used. In a cylindrical region around the magnets, 50 mm in diameter and 50 mm high, the element size was set to 2 mm. The small element sizes near the magnets were necessary to accurately model the large field gradient near the magnet.

A magnetostatic, scalar potential analysis was performed using the ANSYS finite element software package to determine the magnetic field in the magnetic field geometries used. Within the magnet volumes, a residual induction value of 1.11 T was set, typical for the Nd-Fe-B material. Continuity boundary conditions were set at all of the air volume boundaries shown in Figure 2.1. The relative magnetic permeability of the magnetic material was 1.05. The mesh was generated using the standard meshing algorithm in the ANSYS package. Around the magnets, additional manual mesh refinement was performed to provide sufficient detail for the interpolation algorithm; this was done by trial and error until satisfactory results were achieved. A sample of the ANSYS code used in the model is given in Appendix A.

The magnetic field strength calculated using finite element analysis is used in the particle tracing code to determine the velocity at each particle position. For each position, the code searches the finite element results to locate the four points closest to the particle position. The magnetic field strengths at these points were used to calculate the magnetic field strength by interpolation, and to determine the field gradient at the particle position. Sample C code for the particle tracing code is given in Appendix A.

2.3 Experimental Model and Methodologies

The airways in the tracheobronchial region consist of a series of branching tubes, the largest being the trachea (approximately 25 mm in diameter). The typical air speed in the trachea is 0.4 m/s [9]. The tubes are lined with a cellular epithelium containing glands that secrete a 5 – 10 μm thick layer of mucus that is moved up the airway by cilia in order to remove foreign particles.

The above physiological system was modeled by flows of air and water in opposite directions inside of an acrylic channel (25 mm × 50 mm, 300 mm long, see Figure 2.3). Deposition of particles in the channel due to gravity was thus negligible, since the length of the channel is much less than the average settling distance due to gravity, i.e. 3.8 m for the particles used (1 – 3 μm carbonyl iron spheres from Alfa Aesar). The particles chosen because they could correspond to the magnetic cores of 6 – 10 μm therapeutic particles with polymer shells, and because they require no additional preparation, e.g. freeze-drying, for dispersion in a dry powder aerosol.

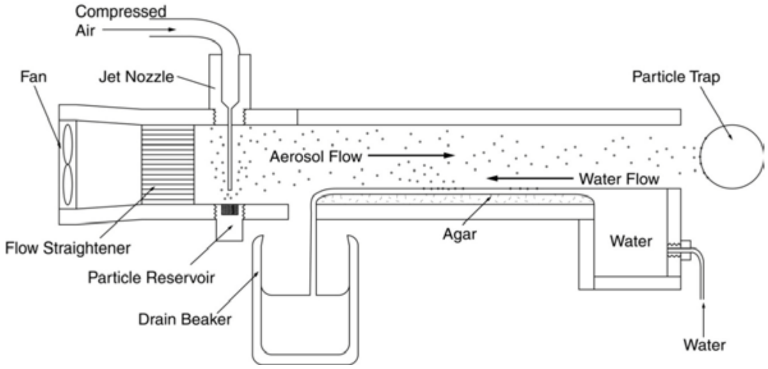

Figure 2.3: The experimental apparatus. The apparatus consists of an acrylic channel, 25 mm × 50 mm, 300 mm long. The aerosol was generated using a 95 m/s jet of compressed air from a 17 Ga. needle, and the particles entrained in the air flow produced by the fan. The particle trap consisted of a 75 mm long, 25.4 mm internal diameter copper tube with permanent magnets inside. A 0.1 mm/s flow of water atop an agar bed at the bottom of the channel was used to simulate mucus flow. The water flow was produced by a peristaltic pump.

The aerosol was produced by deaggregation of iron particles, using a jet of air [10], which were entrained in the main flow of air produced by a fan (see Figure 2.3). Those particles that did not deposit in the channel were caught at the end by a particle trap, whereas particles deposited in the channel and removed by the water flow were caught in a beaker. The water was allowed to flow for 15 minutes after the aerosol was passed through the channel in order to see if any particles were removed. By collecting all of particles that passed through the channel, the collection efficiency of the magnets could be determined. The mass of iron particles dispersed was 31 ± 3 mg, giving a maximum particle volume fraction of 4×10^{-5} (based on the size of the aerosol generator section of the apparatus).

The agar bed served two purposes: to facilitate the flow of water as a thin film, since agar is very hydrophilic, and to facilitate measurement of the amount of particles deposited in the channel. After each experiment, the agar in the channel was divided into four sections. Each section was carefully removed to avoid loss of particles and placed in a beaker of water. The beakers were heated on a hot plate until the agar melted. The iron particles were held in the beaker with a permanent magnet as the water and melted agar were poured out. The particles were then rinsed, dried, and weighed using an analytical balance (Sartorius Model BL210S, 0.1 mg resolution). The particles from the particle trap and drain beaker were washed into beakers, separated, and weighed similarly.

The air velocity profile in the channel (Figure 2.4) was measured using particle Doppler anemometry. The air flow was made laminar using a flow straightener. The disruption of the velocity profile due to the jet used to disperse the aerosol particles was assumed to be the minimal. The air flow in the channel from the fan was 0.47 L/s; the air flow from the jet was 0.08 L/s for 0.2 s, increasing the air flow by only 3% over one second. The velocity of the air at each particle position was determined by interpolating from the velocity profile (Figure 2.4). Mucus clearance was simulated with a 0.1 mm/s flow of water atop an agar bed (see Figure 2.3). In reality, the flows of air and mucus are much more complex. The simplifications described were made to examine the parameters affecting aerosol deposition, and for verification of the numerical model.

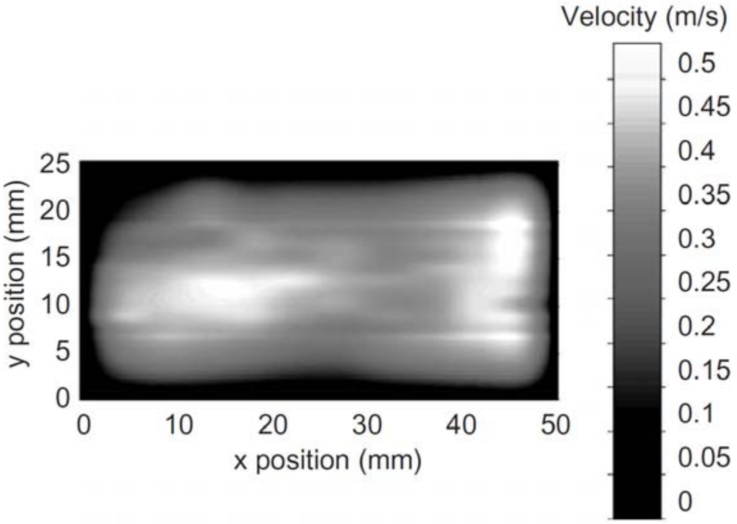

Figure 2.4: The air velocity profile over the 25 mm × 50 mm cross section of the channel. The velocity profile was measured by particle doppler anemometry, which uses laser beams to measure the velocity of a fine mist of water droplets in a flow at a given point; the droplets follow the streamlines of the flow. The velocity profile measurements showed that at all points the velocity was parallel to the long axis of the channel. The average velocity was 0.34 m/s.

Using the setup described above, two sets of experiments were conducted. In the first set, the magnetic field was applied using electromagnets in a magnetic circuit; the channel was placed between the pole pieces of the circuit, as shown in

Figure 2.5(a). In the second set of experiments, permanent magnets were placed in the channel underneath the agar layer, as shown in Figure 2.5(b).

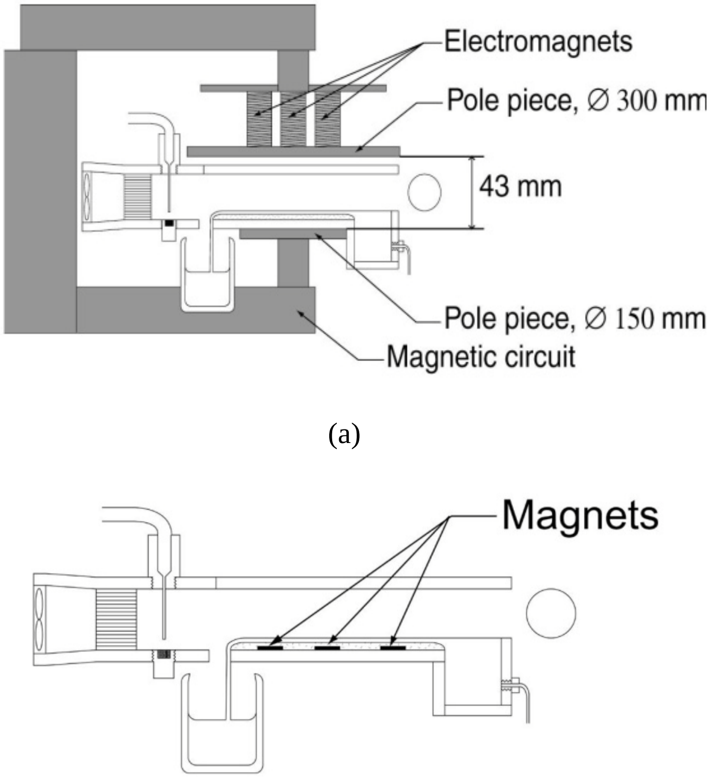

(a)

(b)

Figure 2.5: (a) The experimental apparatus in between the pole pieces of the magnetic circuit. The three permanent magnets had a magnetomotive force of 4000 ampere-turns, with 35 mm diameter 1018 steel cores. The magnetic circuit was also made of 1018 steel, and had a square cross-sectional area of 2500 mm^2. (b) The apparatus with permanent magnets (3 permanent magnet configuration shown). The magnets were 25.4 mm diameter, 3.2 mm thick neodymium-iron-boron magnets.

2.4 Results and Discussion

Collection efficiencies were calculated for each section of the apparatus. The collection efficiency (CE) for a section was defined as the percentage of the total particles deposited in the section. The collection efficiency for each experimental configuration was averaged over three replicate experiments; the results are shown in Figure 2.6(a). The sections of the apparatus were numbered as shown in Figure 2.6(b). In the magnetic circuit configuration, less than 10% of the particles were retained in the channel. With the permanent magnet configurations, overall CE of 48 - 87% were achieved (CE depended on the number of magnets used. The graph in Figure 2.6(a) shows the collection efficiency for each section (see Figure 2.6(b)).

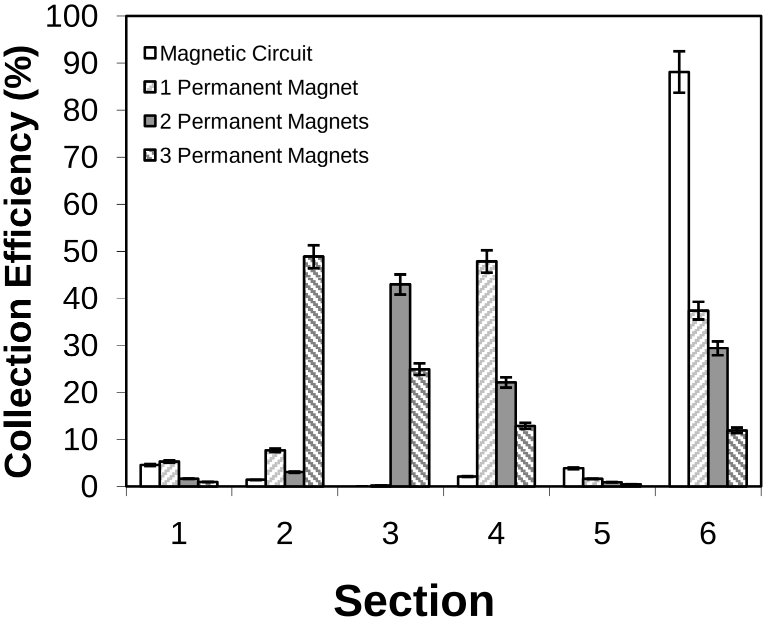

(a)

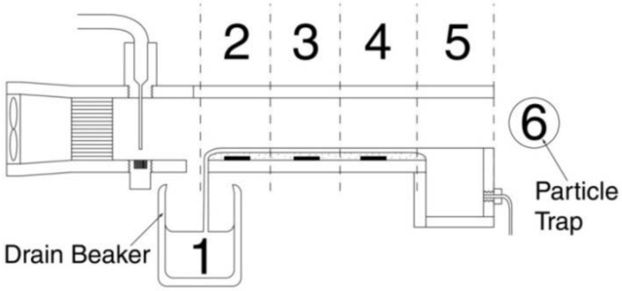

(b)

Figure 2.6: (a) Experimental particle collection efficiencies for each channel section. Collection efficiency for section 3 in the magnetic configuration was 0%. In the single permanent magnet configuration, the magnet was placed in section 4. In the two magnet configuration, the magnets were in sections 3 and 4. In the three magnet configuration the magnets were in sections 2, 3, and 4. (b) Channel section numbering (3 permanent magnet configuration shown).

The collection efficiencies predicted numerically corresponded within 12% of the experimental results in the three magnet configuration. For the two magnet configuration, the predicted CE corresponded within 10%, and for a single magnet, within 4%. The numerically predicted collection efficiencies were based on the trajectories of 900 particles, 1 – 3 μm in diameter, distributed over the cross section of the channel entrance. Figure 2.7 shows that collection efficiencies predicted using the numerical model tended to be less than the actual collection efficiencies. Particle aggregation was a likely source of error in the numerical results. In the experiments, particle aggregates could have been produced by collisions in the aerosol flow, or by particles adhering in the particle reservoir before dispersal. The aggregates would have larger effective diameters than single particles, causing the particle tracing code to underestimate the magnetic force on some of the particles (see section 2.1). An explanation for the larger deviations between the numerical and experimental results in the two and three magnet configurations is that the error may be due to the formation of larger (aggregated) particles in the aerosol due to the magnetic field. Preferential deposition of the larger particles in section 3 for the two magnet configuration and section 4 for the three magnet configuration would produce the observed deviation from the numerical results.

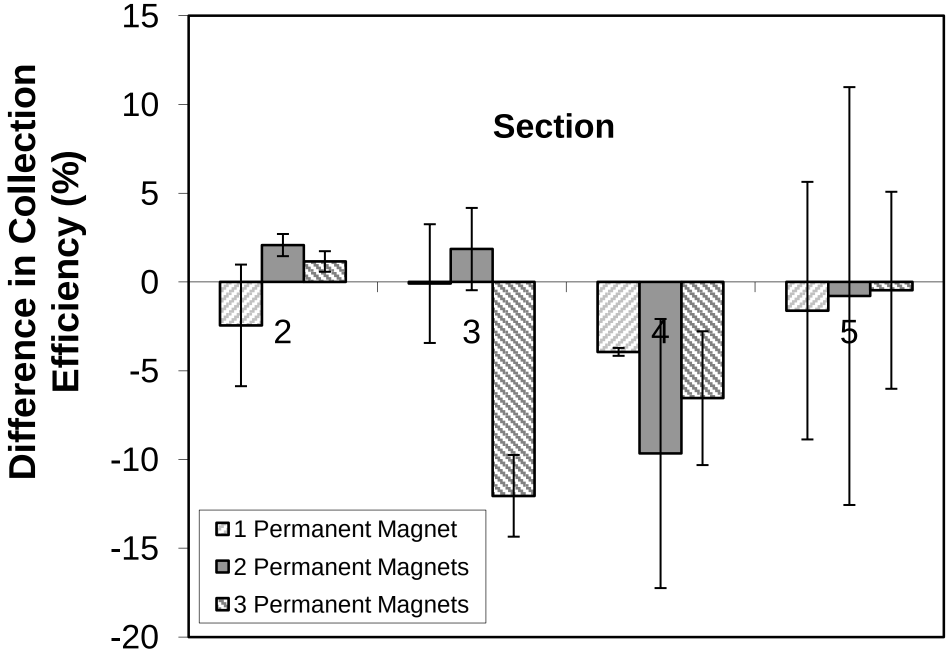

Figure 2.7: Difference between numerical and experimental collection efficiencies in the three permanent magnet configurations. The error bars represent the standard deviation of the experimental measurements.

The difference in the collection efficiencies between the permanent magnet and magnetic circuit results illustrates the importance of the magnetic field gradient. The collection efficiency for a single permanent magnet was twenty times that of the magnetic circuit, despite the size of the bottom pole piece (150 mm diameter) being much larger than the size (25.4 mm diameter) of a permanent magnet. At the midpoint of the channel away from the edges of the pole pieces, the magnetic field strength was 36 mT. At the same point above a permanent magnet, the field strength was 45 mT, only 10 mT higher. The field gradient for electromagnet was 0.03 mT/mm, while for the permanent magnet the field gradient was 3 mT/mm, one hundred times higher, which made the single permanent magnet more effective than the magnetic circuit.

The results show that the overall collection efficiency for the channel increases with more permanent magnets. The individual collection efficiency of each added magnet decreases, however (see Figure 2.8). This is because the particle concentration of the aerosol decreases as particles are deposited. This is clearly illustrated in the numerical results shown in Figure 2.9; it shows that the particle concentration in the region near the magnets decreases along the channel length, i.e. the number of particles available for deposition is reduced (fewer trace lines seen in Figure 2.9 as distance from the channel entrance increases). Figure 2.9 also shows that the particle concentration decreases more in the lower half of the channel where the magnets are placed than in the upper half, i.e. fewer trace lines are seen in the bottom half of Figure 2.9 after ~150 mm along the channel compared to the upper half.

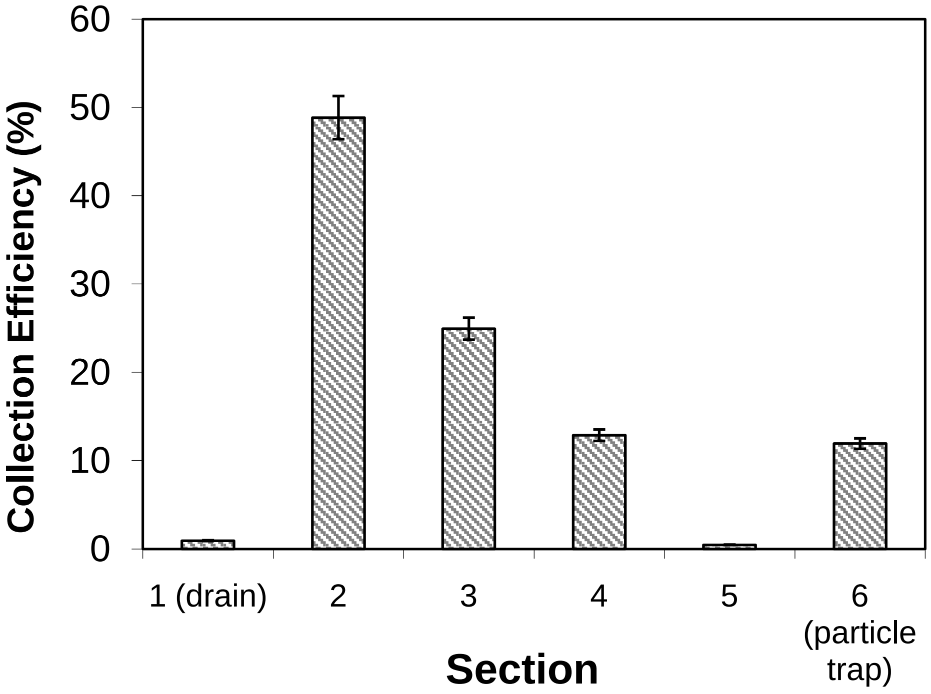

Figure 2.8: Collection efficiency results in the three magnet configuration. The total collection efficiency for the three permanent magnet configuration was 87%.

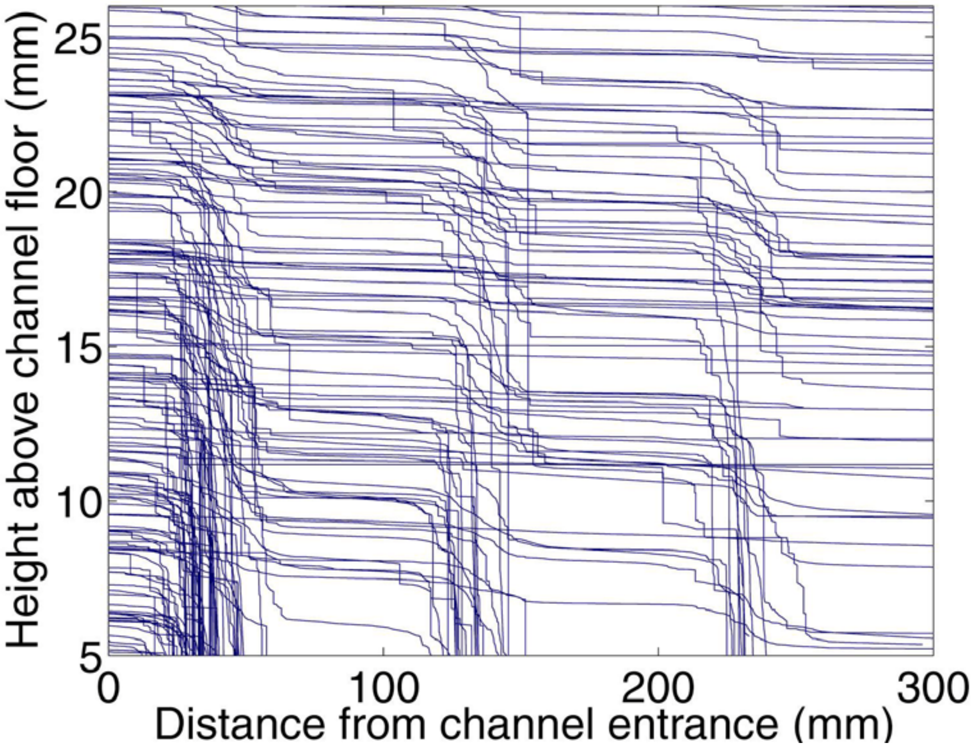

Figure 2.9: Particle trajectories (shown with hairline trace-lines) as predicted by the particle tracing code for the three magnet configuration. Nine hundred particles with diameters from 1 – 3 μm are distributed randomly along the cross section of the channel entrance. Two hundred seventy-seven particles left the channel uncaptured, representing a 69% collection efficiency predicted numerically.

Overall, the results of this model study show promise in application of magnetic targeting for aerosolized delivery of chemotherapeutic agents; it demonstrates in principle the potential of such strategy, for the first time, to target aerosolized drugs for lung cancer treatment. These results give insights into the design requirements for a magnetic aerosol targeting system. A high magnetic field strength and gradient is desirable for this purpose. The high gradient region of the magnetic field should be as large as possible. The particle concentration should also be considered. To maximize the collection efficiency, particles should be removed from all regions of the aerosol flow, for example by applying the magnetic field from various directions. Of course further studies to address the effects of fluid flow, e.g. as a result of coughing or geometry of the airways should be studied. Plans are to represent a more realistic mucociliary clearance mechanism by using frog palates. Regarding the numerical study, Eq. (2.2), can be modified using various correction factors to account for Brownian motion of particles less than 1 μm in diameter, as well as for non-spherical particles, particle clusters, and wall effects. These corrections could be used to extend working conditions of the numerical model beyond those considered in this chapter and result in better agreement between the experimental results and numerical predictions.

2.5 Conclusions

The results of this chapter demonstrate *in vitro* the possibility of magnetically targeting aerosols for chemotherapy. Magnetically targeted site-specific deposition was achieved, and the deposited particles were not removed by the simulated clearance mechanism. The particles used, 1 – 3 μm iron spheres, could correspond to the ferromagnetic cores of therapeutic particles. A numerical model was also developed to predict the trajectories of the aerosol particles. The numerical model was validated using the experimental results. The results of the experiments showed that magnetic field gradient and aerosol particle concentration are important considerations for magnetic targeting of aerosols.

2.6 References

1. Spencer, H. Pathology of the Lung. 4th Ed. Oxford : Pergamon Press, 1985.

2. Scheuch, G., Stahhofen, W. and Heyder, J. 1996. An approach to deposition and clearance measurements in human airways. J. Aerosol Med., Vol. 35, pp. 35-41.

3. Dikanskii, Y.I. and Kiselev, V.V. 1998. Magnetosensitive aerosols and prospects of their application. Magnetohydrodynamics, Vol. 34, pp. 212-215.

4. Merrison, J., *et al*. 2002. Simulation of the martian aerosol at low wind speeds. J. Geophys. Res., Vol. 107, pp. 16.1-16.8.

5. Lübbe, A.S. and Alexiou, C., Bergemann, C. 2001. Clinical applications of magnetic drug targeting. J. Surg. Res, Vol. 95, pp. 200-206.

6. Goodwin, S., *et al*. 1999. Targeting and retention of magnetic targeted carriers (MTCs) enhancing intra-arterial chemotherapy. J. Magn. Magn. Mater., Vol. 194, pp. 132-139.

7. Liu, J., Flores, G.A. and Sheng, R. 2001. In-vitro investigation of blood embolization in cancer treatment using magnetorheological. J. Magn. Magn. Mater, Vol. 225, pp. 209-217.

8. Gerber, R. and Birss, R.R. High Gradient Magnetic Separation. England : Research Studies Press, 1983.

9. Finlay, W.H. The Mechanics of Inhaled Pharmaceutical Aerosols: An Introduction. London : Academic Press, 2001.

10. Wang, Z.L., Lange, C.F. and Finlay, W.H. 2004. Use of an impinging jet for dispersion of dry powder inhalation aerosols. Int. J. Pharm., Vol. 275, pp. 123-131.

Chapter 3: Factors affecting magnetic retention of particles in the upper airways: an *in vitro* and *ex vivo* study*

The purpose of this chapter is to study the retention of magnetic particles deposited from aerosol on the airway surface using a magnetic field. As will be discussed, the mechanism particle retention at the airway surface is very different than in intravenous applications. There are two aspects of magnetically targeted aerosol drug delivery that must be considered, deposition and retention. The previous chapter showed the feasibility of magnetic particle deposition from aerosol with a magnetic field, using an *in vitro* model [1]. In this chapter, large-scale retention of deposited particles is considered.

Magnetic particle retention in the conducting airways is necessary for the development of a targeted aerosol drug delivery system for the treatment of lung cancer in this region. Delivery of chemotherapy drugs in the form of an aerosol has the potential to reduce the side effects of chemotherapy by bypassing the circulatory system. For this form of delivery to be effective, the drug particles must be deposited and retained at the cancerous regions of the airways to prevent damage to healthy tissue.

There is a great deal of research in the literature on targeted delivery of magnetic particles in the circulatory system and to tumors in various regions of the body [2-4]. Previous studies have focused on the retention of particles in the circulatory system using magnetic fields [5], development of magnetic stents [6], and particle embolization to cut blood flow to tumors [7]. The behavior of

---

* A version of this chapter has been published. Ally, Amirfazli, Roa 2006. Journal of Aerosol Medicine. 19: 491-509.

nonmagnetic particles at the airway surface has also been studied on a microscopic scale in [8]. This chapter is the first study of magnetic particle retention in the conducting airways. For the purpose of this chapter, the conducting airways considered are the trachea and bronchi only. The clearance mechanism in the conducting airways is significantly different from blood flow in a vessel, as it consists of a highly non-Newtonian surface flow propelled by cilia instead of pressure.

The conducting airway surface is characterized by a layer of viscoelastic mucus that flows atop a watery periciliary layer (Figure 3.1). The mucus layer is typically ~5-10 μm thick; the thickness of the periciliary layer is ~5-7 μm [9]. The mucus layer is propelled toward the larynx by the beating action of the cilia on the underlying cellular epithelium. In a healthy adult, the mucus transport rate in the trachea is approximately 7-14 mm/min [10]. The mucus thickness and transport velocity can vary dramatically depending on the health of the airways.

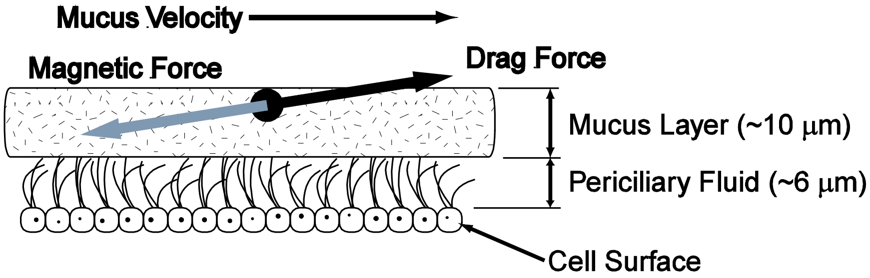

Figure 3.1: A simplified schematic of the surface of the conducting airways. The mucus layer sits atop a watery periciliary layer, and is propelled by the beating of cilia.

The mucus clearance mechanism is the natural defense of the conducting airways against inhaled particles such as dust and bacteria. Particles that deposit in the conducting airways are entrained in the mucus layer and removed. Particles deposited in the trachea and bronchi area may be cleared in as little as 1 hour in healthy subjects [11]. In this chapter, magnetic force is investigated as a means to overcome particle clearance and hold future drug-laden particles at a target site (Figure 3.1). Such particles would have to be made magnetically susceptible by incorporation of a magnetic material such as iron or iron oxide in their formulation. Therapeutic magnetic microparticles have been used in previous studies for treatment of cancer in humans, and their iron content was considered safe [2].

3.1 Theoretical Background

For particles to be retained at the conducting airway surface, the magnetic force on the particles must be greater than the drag force due to the flow of mucus around the retained particles (Figure 3.1). Due to the fact that the particles form large aggregates upon deposition, these forces cannot be accurately computed without a model of aggregate geometry. In the case of drag forces, various empirical corrections for aggregate geometry have been determined. Such approximations are, to the authors' knowledge, not available for magnetic forces. The factors affecting the particle forces, aside from the particle geometry can, however, be identified from the expressions for the drag and magnetic forces on spherical particles. For this reason, the equations for calculation of drag and magnetic force on a spherical particle are examined in this section.

The drag force on initially deposited particles causes them to move along with the mucus layer as a result of the mucus flow. A suitably designed aerosol drug particle should be generally less than approximately 10 μm aerodynamic diameter to pass through the mouth and throat area and deposit in the conducting airways. For spherical particles of this size immersed in a Newtonian fluid at flow rates within the range of those found in the airways, the drag force is governed by the Stokes equation for drag on a sphere:

$$\vec{\boldsymbol{F}}_{\boldsymbol{D}} = -3\pi\eta d\vec{\mathbf{v}}_{\boldsymbol{rel}} \qquad (3.1)$$

where $\vec{\boldsymbol{F}}_{\boldsymbol{D}}$ is the drag force, d is the particle diameter, η is the fluid viscosity, and $\vec{\boldsymbol{v}}_{\boldsymbol{rel}}$ is the relative velocity of the particle with respect to the fluid. For partially immersed particles, the drag force depends upon these same parameters, although the scaling factor will be different. The drag force on a partially immersed particle is given by [12]:

$$\vec{\boldsymbol{F}}_{\boldsymbol{D}} = -3\pi\eta d\vec{\mathbf{v}}_{\boldsymbol{rel}}\, y(\theta) \qquad (3.2)$$

where y is a scaling parameter depending on the particle contact angle θ. Particles deposited on the airway surface are, at least initially, partially immersed, as shown by Schürch *et al*. [8]. For drag due to a Stokes flow of a viscoelastic fluid, such as the non-Newtonian liquids used in these experiments, flowing past a sphere, the drag force is calculated by applying a correction factor to the above expressions. The same parameters that determine the drag force on a sphere in a Newtonian fluid, i.e. particle size, relative velocity, and steady-state viscosity of the fluid, thus also determine the drag force in a viscoelastic fluid [13]. For low shear rates, viscoelastic liquids such as mucus or the mucus stimulant used in these experiments can be compared to Newtonian liquids using their apparent low-shear rate viscosity.

The drag force must be balanced by the magnetic force on the particles. For a paramagnetic sphere that is small enough to be considered a point in the magnetic field, i.e. the field strength and gradient do not vary over the particle diameter, the magnetic force is given by the following equation [14]:

$$\vec{\boldsymbol{F}}_{\boldsymbol{M}} = \mu_0 \chi V_p \vec{\boldsymbol{H}} \nabla \vec{\boldsymbol{H}} \qquad (3.3)$$

where $\vec{\boldsymbol{F}}_{\boldsymbol{M}}$ is the magnetic force, μ_0 is the magnetic permeability of vacuum, χ is the magnetic susceptibility of the particle, V_p is the particle volume, and $\vec{\boldsymbol{H}}$ is the magnetic field intensity at the particle location. Note that as a result of the magnetic field term $\vec{\boldsymbol{H}} \nabla \vec{\boldsymbol{H}}$, the field must have a gradient to exert any magnetic force on a particle.

For particles with a high magnetic susceptibility, such as the iron particles used in these experiments, the magnetic force is given by a similar expression [15]:

$$\vec{\boldsymbol{F}}_{\boldsymbol{M}} = 3\mu_0 V_p \vec{\boldsymbol{H}} \nabla \vec{\boldsymbol{H}} \qquad (3.4)$$

Considering only a single particle is unrealistic. In a magnetic field, particles will aggregate, primarily due to the local distortion of the field by individual particles. The magnetic potential ϕ near a small particle in a magnetic field is given by the expression [16]:

$$\phi(r,\theta) = -H_0 r\cos\theta + \tfrac{1}{8} H_0 d^3 \left(\frac{\mu_R - 1}{\mu_R + 2} \right) r^{-2} \cos\theta \qquad (3.5)$$

where H_0 is the field strength and μ_R is the relative permeability of the particle. This expression is given in spherical coordinates (r,θ,ϕ) with the particle at the origin. As shown in Figure 3.2, the particle creates a local field gradient that will cause other particles to be attracted and subsequently forming aggregates. As the aggregates grow, they further distort the field, thus attracting more particles, until a minimum energy configuration, representing an equilibrium is formed.

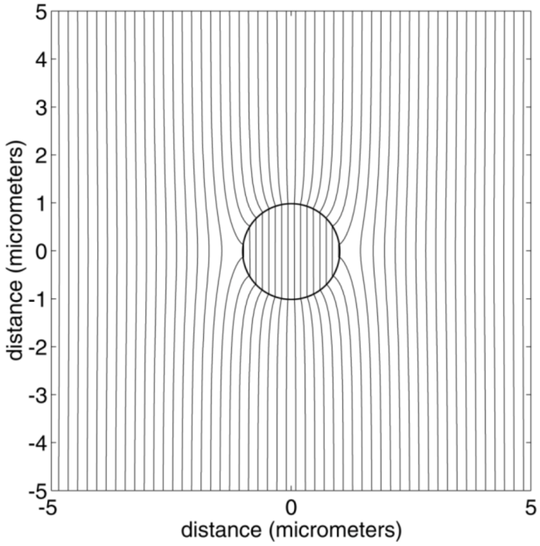

Figure 3.2: Magnetic flux lines of a uniform field distorted by a 2 μm diameter ferromagnetic sphere. The pattern of flux lines shown scales for any diameter ferromagnetic sphere in a uniform magnetic field.

Typically in the literature, aggregates are assigned an equivalent spherical diameter based on a variety of factors, including the aggregate size, particle distribution, porosity, and fractal dimension [17]. The aggregates are treated as spherical particles with the equivalent diameter to calculate the approximate drag force [18]. The drag force on aggregates is thus directly dependent on the fluid viscosity and relative particle velocity as in the case of a spherical particle.

The magnetic forces on aggregates are more difficult to compute due to the distortion of the magnetic field by the particles and nonlinearity of the expression for magnetic force. It is reasonable to assume, however, that the magnetic force on an aggregate of magnetic particles is related to the same variables as the magnetic force on a single particle, i.e. the magnetic susceptibility of the aggregate, aggregate volume, and field intensity and geometry. The difficulty in predicting the behavior of particle aggregates underlines the usefulness of experimental model studies. Whereas the models used in these experiments do not fully replicate the conditions in the human airway, the results obtained are useful in understanding the forces on magnetic particles that would occur in the actual biological system.

In order to study particle retention, two experimental models were used, an *in vitro* model and an *ex vivo* animal model. These models are both based on previous work in the literature. The *in vitro* model consists of a rectangular channel with a liquid flow along the bottom to simulate the flow of mucus in the airways (Figure 3.3(a)). Particles are deposited from an aerosol flowing in the opposite direction of the liquid through the channel [1]. A similar model was used by King *et al*. to study mucus clearance due to coughing, using a stationary mucus simulant to simulate the airway surface [19]. The *ex vivo* model consists of a mucus-depleted bullfrog (*Rana catesbeiana*) palate. This animal model has been established and used in the literature to simulate the surface of the human airway [20-22]. In these studies, however, the clearance rate of mucus is used to establish the condition of the palate tissue; there have not been any studies on the retention of particles, magnetic or otherwise, on the palate.

Considering the above governing equations, various experimental parameters were adjusted in order to determine the influence of the magnetic field, liquid viscosity and speed, and particle size on particle retention. Three different magnetic fields were applied using various arrangements of permanent magnets. The liquid viscosity in the *in vitro* model was adjusted by using three liquids, water, glycerol, and a mucus simulant, to study a broad range of viscosities and the effects of viscoelasticity in the case of the mucus simulant. The liquid speed was controlled with a peristaltic pump in the *in vitro* model. To change the mucus transport velocity in the *ex vivo* experiments, the frog palate specimens were reused (after each use in a set time interval, the mucus transport velocity decreases). To observe the effect of particle size, two types of particles were used: spherical iron particles, 1 – 3 μm in diameter, and irregular iron oxide particles, of ~180 μm characteristic size.

3.2 Materials and Methods

The *in vitro* experiments were performed using the apparatus illustrated in Figure 3.3(a). The apparatus consists of a 25 × 50 mm channel, 300 mm long. The mucus flow was simulated by a liquid flow along the bottom of the channel. The liquid flow was produced by overflowing a reservoir at one end of the channel using a peristaltic pump (Fisher Scientific Company, Ottawa, Canada), which allowed the flow rate to be adjusted; the flow rates used are given in Table

3.1. The channel walls were optical windows to allow visual observation with a camera. Experiments were performed using three different fluids, water, glycerol (Fisher Scientific), and a mucus simulant, to observe the effects of viscous drag. The mucus simulant consists of a 2%wt solution of locust bean gum (Sigma Aldrich Canada Ltd., Oakville, Canada) in water crosslinked with a solution of 4% sodium tetraborate (Fisher Scientific). This simulant has been used in the literature to model tracheal mucus clearance by coughing [19]. Water was used to test particle retention at low viscosities. Glycerol was used to observe the effects of Newtonian drag at higher viscosities. The mucus simulant was used to observe non-Newtonian drag similar to what is seen in pulmonary mucus (also a non-Newtonian fluid).

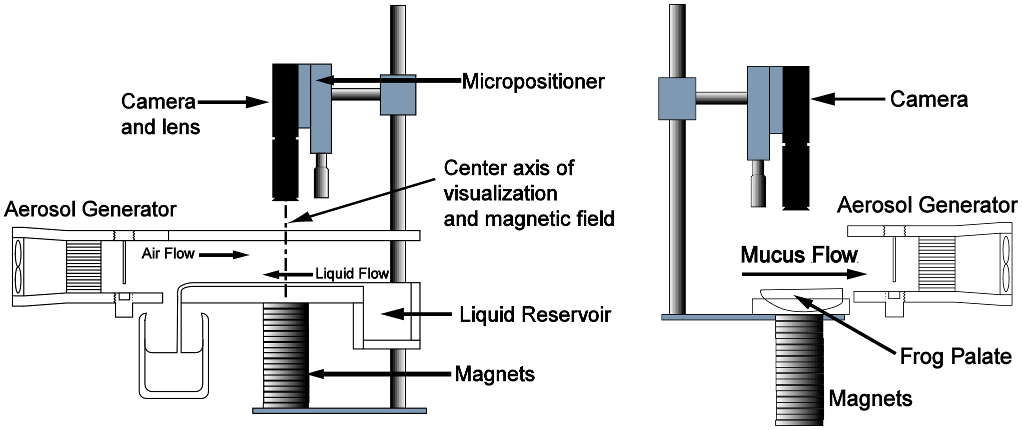

(a) (b)

Figure 3.3: (a) The in vitro experimental apparatus. The apparatus consists of an acrylic channel, 25 mm × 50 mm, 300 mm long. The aerosol was generated using a 95 m/s jet of compressed air from a 17 Ga. needle, and the particles entrained in the air flow produced by the fan. A flow of liquid along the bottom of the channel was produced by overflowing the liquid reservoir with a peristaltic pump (not shown). The liquid flow was viewed from above by a camera mounted on a micropositioner for focusing. The magnetic fields were applied by placing various magnets beneath the channel. (b) The ex vivo animal specimen apparatus. The frog palate was placed in a petri dish. A nebulizer (not shown) was used to keep the palate from drying out during experimentation.

The viscosity of the glycerol and mucus simulant were measured using a Brookefield dial viscometer and a Rheometrics RMS-800 rheometer, respectively. The viscosity of the glycerol was 1 Pa·s; for near-zero shear rates (less than 0.1 rad/s), the apparent viscosity of the mucus simulant was 3.26×10^4 Pa·s. The viscosity of human tracheal mucus was predicted by King and Macklem [23] to be in the order of 2×10^3 Pa·s at low shear rates, based on extrapolation of experimental measurements. There is a great deal of variability in reported values of apparent mucus viscosity at low shear rates, ranging from 10^1 to 10^3 Pa·s in order of magnitude. Although at higher shear rates, the behavior of the mucus stimulant and actual mucus would be non-Newtonian and elastic, for low shear rates, the measured value can be approximated as a Newtonian viscosity for the purpose of predicting the behavior of small particles at low speeds.

The aerosol was produced by dispersing spherical iron particles, 1 - 3 μm in diameter (Alfa Aesar, Ward Hill, MA, USA), using a jet of compressed air, as described by Wang *et al*. [24, 25] The aerosol particles were deposited from a flow of air in the opposite direction of the liquid flow, to simulate inhalation of an aerosol. Particles were deposited due to a magnetic field applied by placing a 25 mm diameter, 3.2 mm thick Neodymium-Iron-Boron magnet underneath the channel. The top pole of the magnet was 12 mm away from the liquid surface. This field was used to deposit particles in all experiments to ensure comparable results. The aerosol likely contained particle aggregates as well as individual particles. This would not significantly affect the experimental results, as much larger aggregates were formed upon deposition. After ~10 seconds, the magnetic field used for retention was applied. The three fields used were applied with the single disk magnet, a stack of 20 disk magnets, and a single Nd-Fe-B block magnet, 50 × 50 × 25 mm, polarized along its short axis (Dexter Magnetic Technologies, Fremont, CA, USA).

The vertical magnetic field flux densities, measured along the axis of the camera (Figure 3.3(a)) at the surface of the liquid (12 mm from the magnet pole), were 116 mT, 148 mT, and 232 mT; the respective field gradients along the camera axis were 2.5 mT/mm, 10.2 mT/mm, and 11.4 mT/mm. These values will be used to refer to the magnetic fields used in the following sections to give a relative indication of the field strengths and gradients. The magnetic field measurements were made using a gaussmeter (F.W. Bell Model 5080). The measurements were used to verify finite element model simulation results (obtained using the ANSYS finite element package) of the entire field around the magnets. Flux lines computed for each magnet are shown in Figure 3.4.

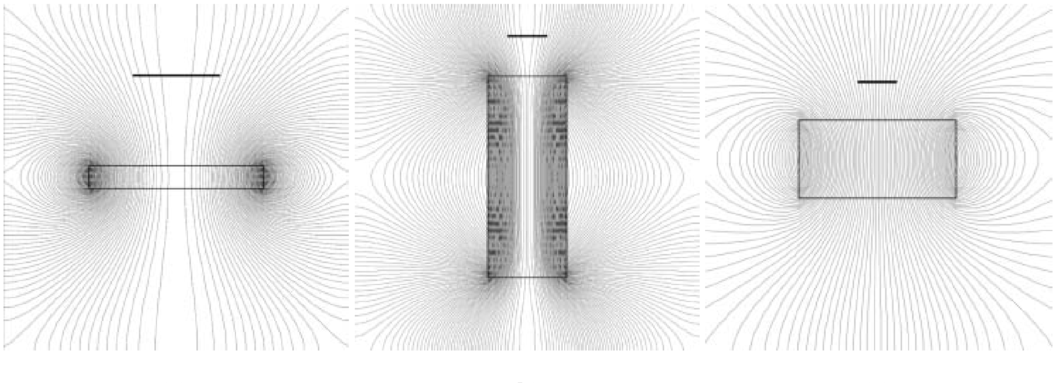

(a) (b) (c)

Figure 3.4: Magnetic flux lines of the (a) 116 mT field (single Nd-Fe-B magnet, 25 mm diameter, 3.2 mm thickness), (b) 148 mT field (20 Nd-Fe-B magnets, each 25 mm diameter, 3.2 mm thickness), and (c) 232 mT field (single Nd-Fe-B block magnet, 50 × 50 mm, 25 mm thick). The thick black line indicates the location of the region observed by the camera.

The frog palate experiments were performed similarly, with a frog palate in a petri dish replacing the channel, as shown in Figure 3.3(b). The frog palate was harvested and prepared according to the procedure described in references [19-21]. This procedure allows the palates to be used for multiple experiments, with a diminishing mucus transport rate, corresponding to diminished transport rates that would be seen in unhealthy airways. All procedures involving animals were approved by the University of Alberta Health Sciences Animal Welfare and Protection Committee.

In addition to the spherical iron particles, irregular iron oxide particles of ~180 μm characteristic size (#1 Gray Powder, Magnaflux, Glenview, IL, USA) were also tested on the frog palates and mucus simulant to study the effect of particle size. Iron oxide particles are paramagnetic, with a magnetic susceptibility of 7.2×10^{-3}. These particles were too large to aerosolize, and were deposited by sprinkling them on the liquid surface.

The particle deposition and retention in the channel and on the palates was observed using a camera looking down at the liquid surface. The field of view was 9 × 7 mm, with a resolution of 0.01 mm, centered over the geometric center of the magnet used for each experiment. Images were captured at 10 Hz for 10 s during particle deposition, and afterward at 0.1 Hz for 15 min to observe particle retention. Particle retention was characterized by a buildup of particles in the field of view. The liquid flow speed was determined by measuring the position of tracer particles in the absence of magnetic field at regular intervals using a 0.25 mm graticule (Pyser SGI, Edenbridge, Kent, UK).

3.3 Results

Figure 3.5(a), (b), and (c) show the magnetic scalar potentials at the liquid surface for each of the fields used. The figures show the field potential in the field of view of the camera in the same plane as the surface of the liquid or palate used, as computed using finite element models of the magnetic fields (ANSYS). Figure 3.6 shows the magnitude of the magnetic flux, i.e. the magnitude of the gradient of the potential field, normalized for each magnet. As the fields are radially symmetric about the camera axis, Figure 3.6 shows the variation of the magnetic field in the observed region.

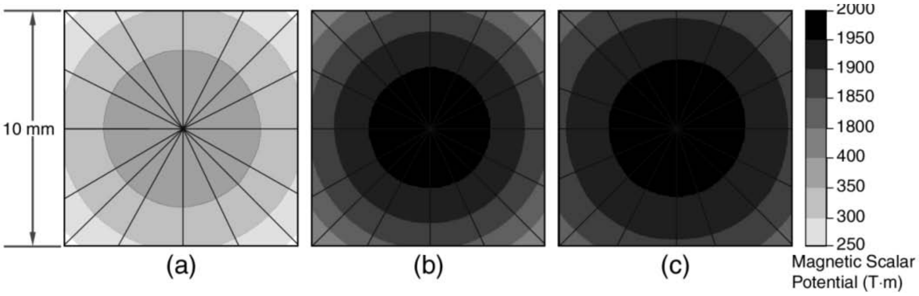

Figure 3.5: Magnetic potential lines for the (a) 116 mT field (b) 148 mT field, and (c) 232 mT field, 12 mm away from the magnet surface, viewed on the center axis. Potential contours were computed using finite element analysis. Lines on the plots show the direction of the magnetic flux.

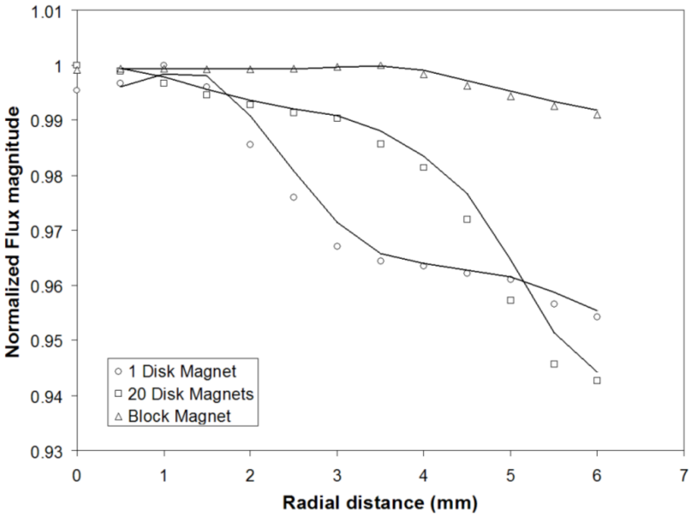

Figure 3.6: Magnitude of magnetic flux for 1 disk magnet, 20 disk magnets, and the block magnet, with respect to the radial distance from the center of the magnets. Flux densities were normalized to the maximum of each field. The data points do not converge at the center as the maximum flux location varied for each magnet. Trend lines were computed using a 2-period moving average.

Tables 3.1 and 3.2 show the results of the *in vitro* and *ex vivo* experiments, respectively. Each row of the tables gives the result of an experimental test. The first column of the table indicates the flow condition, i.e. the liquid used in the *in vitro* experiments, and the frog specimen used in the *ex vivo* animal experiments. The second column indicates the speed of the flow. The two columns for the magnetic flux density and magnetic flux gradient provide the values along the camera axis. The variation of the magnetic flux density over the observed area can be seen in Figure 3.4, which shows the flux lines for each magnet along with a line representing the observed region. The magnitude of the magnetic field strength decreases by 7% at most across the observed region.

Table 3.1: In vitro model results for retention of particles

Liquid (viscosity)	Liquid speed (mm/min)	Field strength (mT)	Field gradient (mT/mm)	Particle type	Retention
Water (0.001 Pa·s)	15	116 116 116	2.5 2.5 2.5	1-3 µm spherical iron	Yes
Glycerol (1 Pa·s)	6	116	2.5		No
	9	116			
	11.25	116			
	9	148	10.2		Yes
	27				
	36				
Mucus Simulant (3.26×10^4 Pa·s)	0.75	116	2.5		No
	2.25				
	3.75				
	0.38	148	10.2		No
	1.5				
	2.25				
	1.81	232	11.5		No
	1.7	116	2.5	~180 µm irregular iron oxide	No
	1.6	148	10.2		Yes

Table 3.2: Ex vivo frog palate model results for retention of particles

Specimen	Transport rate (mm/min)	Field strength (mT)	Field gradient (mT/mm)	Particle type	Retention
Frog 1, 3rd use	0.15	116	2.5	1-3 µm spherical iron	No
Frog 1, 2nd use	0.38				
Frog 1, 1st use	3				
Frog 2, 1st use	4.5				
Frog 3, 3rd use	0.38	148	10.2		
Frog 3, 2nd use	2.25				
Frog 3, 1st use	4.88				
Frog 4, 1st use	5.63				
Frog 5, 1st use	0.38	232	11.5		
Frog 6, 1st use	12				
Frog 7, 1st use	4	116	2.5	~180 µm irregular iron oxide	No
Frog 8, 1st use	5.35	148	10.2		Yes

3.4 Discussion

The magnetic fields used in these experiments can be considered in terms of their vertical and radial components. The vertical component of the field is the component along the camera axis (Figure 3.3(a)), mentioned previously. The flux density and gradient in this direction was 116 mT and 2.5 mT/mm for the single disk magnet, 148 mT and 10.2 mT/mm for the stack of 20 disk magnets, and 232 mT and 11.4 mT/mm for the block magnet. The vertical component of the field produces a component of the magnetic force pulling the particles down towards the pole of the magnet. This component is useful for deposition and for “sinking” of the particles at the target site.

The contours of the magnetic scalar potential (ϕ) in Figure 3.5(a), (b), and (c) show the geometry of the magnetic fields in the observed region, 12 mm away from the magnet pole faces. The potential contours are perpendicular to the magnetic field lines. In the absence of the liquid surface, the particles would deposit along the field lines. The magnetic potential contours also show there is a radial component of the magnetic field as well as a radial field gradient at the liquid surface. This means there would be a radial component of the magnetic force acting on any magnetic particles in the field, due to the tendency of the magnetized particles to move to the region of greatest flux density. Consequently, in a liquid, without any flow, the particles would tend to move toward the highest-potential region and as such the center of the field of view, due to the radial component of the magnetic force. This is the reason for the radial alignment of deposited particles seen in Figure 3.7– Figure 3.11. The tendency of a radial field to concentrate particles at its center could be useful for designing a magnetic field to retain particles in the airways, since concentrating the particles in a small region would increase aggregation and thus improve particle retention, as discussed below. Figure 3.6 shows the normalized magnitude of the magnetic flux density ($\left|\nabla\phi\right|$) 12 mm away from the magnet pole faces, with respect to the radial distance from the center of the magnet (computed using the finite element models of the magnetic fields). The flux densities were normalized to the maximum of each respective field for comparison. Figure 3.6 shows that the stronger the magnet used, the smaller the radial field gradient in the camera's field of view (9×7 mm). The radial magnetic force concentrating particles in the center of the field is therefore reduced. This indicates that to improve the field design, and hence retention, a compromise between field strength and geometry, i.e. field gradients at the target site, is necessary.

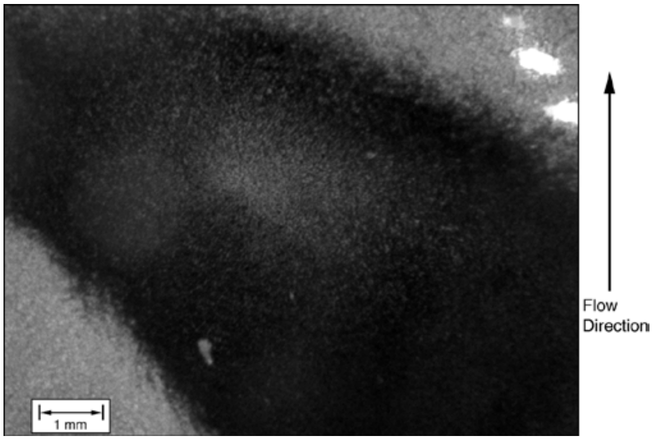

Figure 3.7: Iron particles (dark foreground) retained with the 116 mT field in water at 15 mm/min. The view shown is of the surface of the liquid, at the geometric center of the magnet.

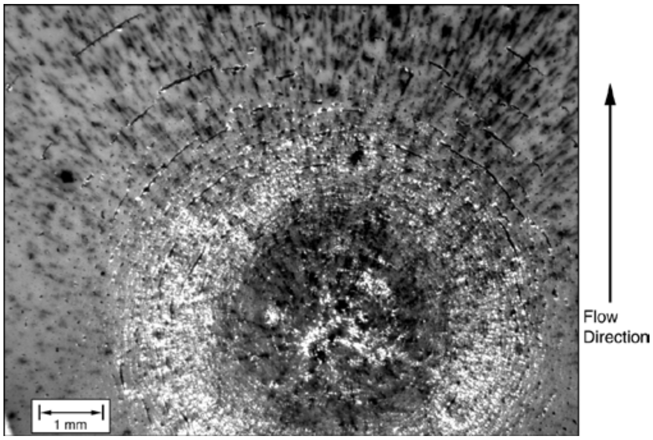

Figure 3.8: Iron particles retained with the 148 mT field in glycerol at 27 mm/min. The view shown is of the surface of the liquid, at the geometric center of the magnet.

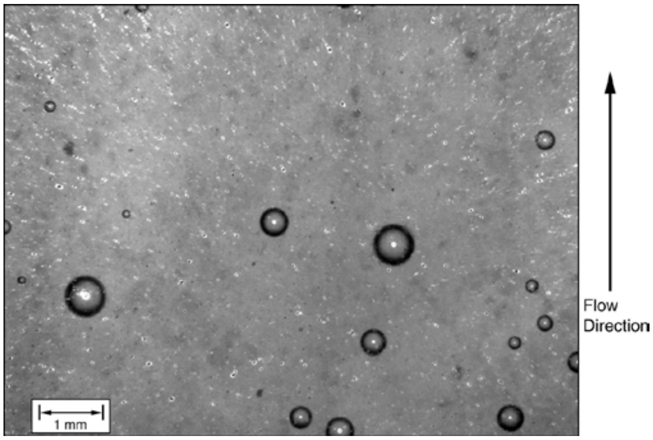

Figure 3.9: Iron particles in the mucus simulant at 1.81 mm/min with the 232 mT field. The view shown is of the surface of the liquid, at the geometric center of the magnet. The particles were not retained in this case. The dark circles in the background are air bubbles beneath the liquid surface entrained in the flow.

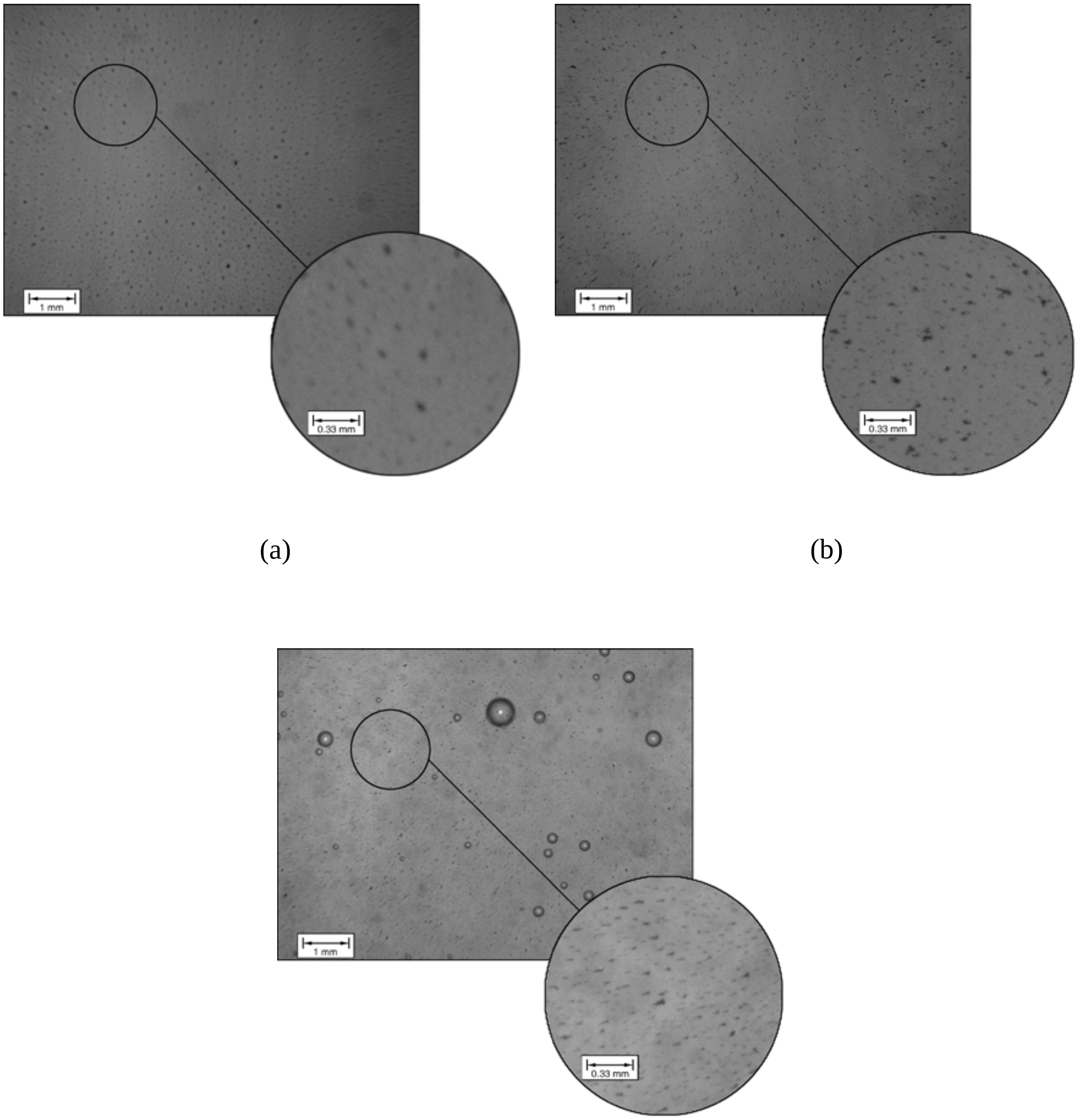

(a) (b)

(c)

Figure 3.10: Initial deposition of iron particles in (a) water, (b) glycerol, and (c) mucus simulant. The dark circles in the background of (c) are air bubbles beneath the liquid surface entrained in the flow.

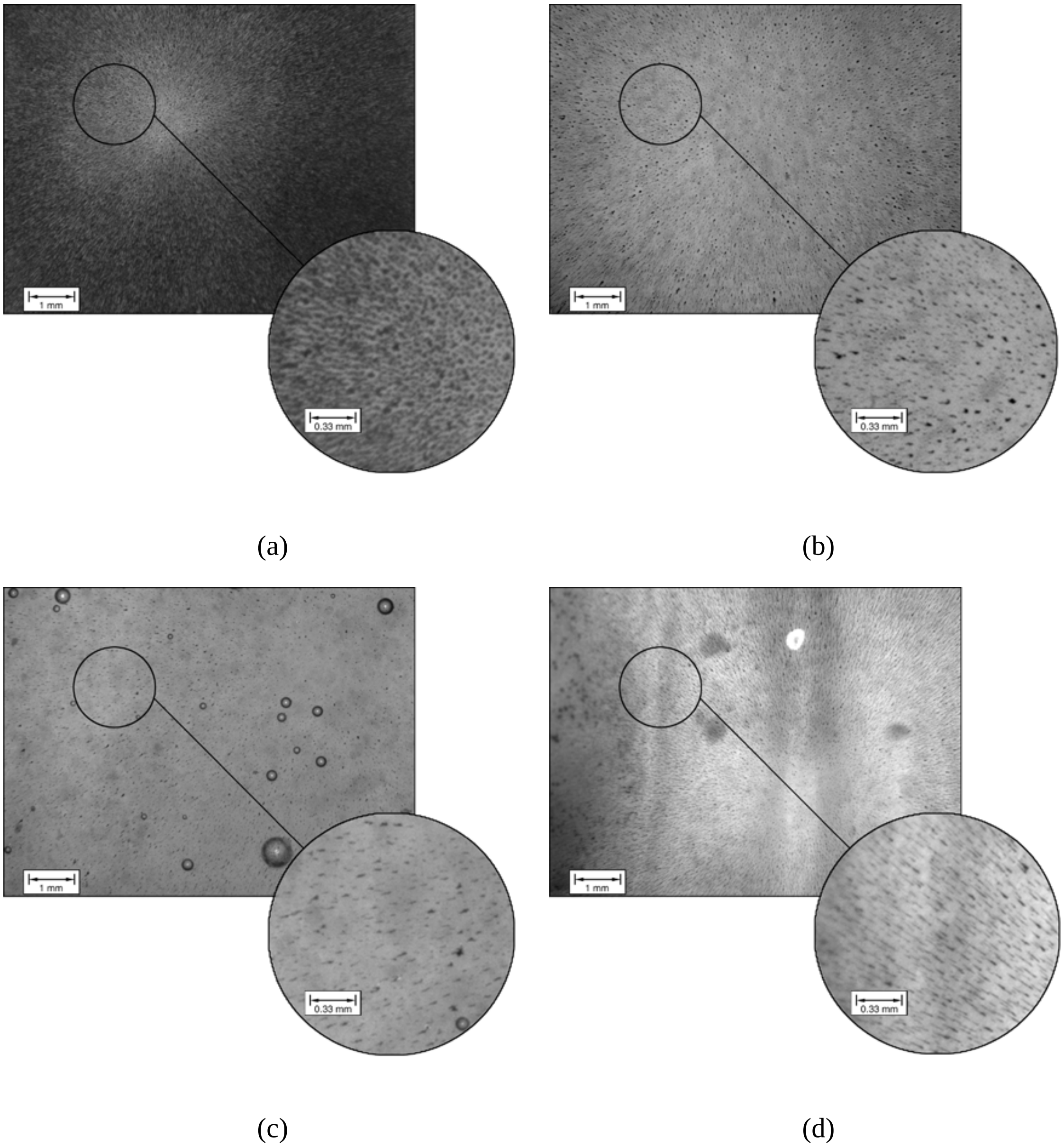

(a) (b)

(c) (d)

Figure 3.11: Aggregates formed 10 s after deposition in (a) water, (b) glycerol, (c) mucus simulant, and (d) on a frog palate.

The results for the different liquids used in the *in vitro* model show that viscosity plays a significant role in determining particle retention. In water, iron particles were retained with the weakest magnetic field (116 mT), as shown in Figure 3.7. In glycerol and the mucus simulant with the 116 mT field, the iron particles were not retained. In glycerol, with a viscosity of 1 Pa·s, iron particles were retained with the 148 mT field (Figure 3.8). In the mucus simulant, none of the applied fields held the iron particles (Figure 3.9 shows iron particles in the mucus simulant with the 232 mT field). Thus, as the viscosity increases so does the magnetic force required to retain particles. However, as equations (2.2) and (3.2) suggest, this relation between liquid viscosity and magnetic force required is not linear for a constant diameter and flow velocity, since viscosity also appears to limit particle aggregation.

Figure 3.10(a), (b), and (c) show the initial deposition of particles in water, glycerol, and mucus simulant. The aggregates deposited from the aerosol appear to be similar in size, shape, and pattern. After 10 seconds in the same magnetic field, as shown in Figure 3.11(a), (b), and (c), the particles in the water have formed large, dense aggregates, strongly aligned with the magnetic field. In glycerol, smaller aggregates formed and were aligned with the magnetic field. In the mucus simulant, no further aggregation appears to have taken place, and the particles do not show any obvious alignment with the magnetic field (Figure 3.11 (c)).

Aggregation also adds to the influence of viscosity on particle retention, since the drag force increases with surface area of the aggregate. However, magnetization, and thus magnetic force, increase with the mass, i.e. volume of the aggregate. Thus, as the aggregate grows, the ratio of magnetic force to the drag force on the aggregate increases, i.e. large aggregates are held by weaker magnetic fields than individual particles.

The aggregates formed on the frog palates (Figure 3.11(d)) appear to be closer in size and shape to those formed in glycerol, compared to those formed in the mucus simulant after ~10 seconds. This may be due to the drag on the aggregates being reduced due to wall effects, since the mucus layer on the palate is very thin. The apparent viscosity of bullfrog mucus at low shear rates is also an order of magnitude less than that of the mucus simulant, although both are much larger than that of glycerol. This difference in apparent viscosity may also account for some of the differences observed due to the effect of viscosity on aggregation and drag. It may also be possible that at the low shear rates (less than 0.1 rad/s) due to particle motion in these experiments, the mucus simulant may not be an appropriate model of tracheal mucus. Previous studies using mucus simulants to simulate tracheal mucus have focused on particle clearance by coughing. This would involve much higher shear rates, at which the simulant is considered a good model. At higher shear rates, the apparent viscosity is reduced considerably in shear-thinning non-Newtonian fluids such as tracheal mucus. At low shear rates, the viscosity of the bullfrog mucus appears much lower than the viscosity of the mucus simulant.

For the range of the liquid speed studied (0.4 – 36 mm/min), there appeared to be little effect on particle retention in the *in vitro* model. The results show (Table 3.1) that in water and glycerol, particles were retained with the 116 mT and 148 mT fields, respectively, at transport speeds even higher than the normal mucus transport rate in the human trachea. With the mucus simulant, even at flow rates much lower than what would be found in a healthy human trachea, particles were not retained. Likewise, in the *ex vivo* experiments, particles were not retained even at low transport rates (with one exception). Whereas the liquid velocity is directly related to the drag force as is the viscosity in equations (2.2) and (3.2), it is less significant due to the fact that the viscosity also limits particle aggregation as described above.

Figure 3.12(a) and Figure 3.13(a) show the surfaces of the mucus simulant and a frog palate with iron particles in the 232 mT magnetic field. The bright spots seen in the images (encircled areas) are due to rippling of the fluid surface. This rippling is due to deformation of the surface as the particles are pulled into the liquid interface, which indicates that the particles do not completely penetrate the surface. This is clearly evident since the ripples disappear (Figure 3.12(b) and Figure 3.13(b)) and the particles are cleared once the magnetic field is removed. This suggests that a possible approach to improving particle retention could be to alter the surface chemistry of the particles, e.g. by making the particles more hydrophilic, making it possible for them to penetrate the mucus layer.

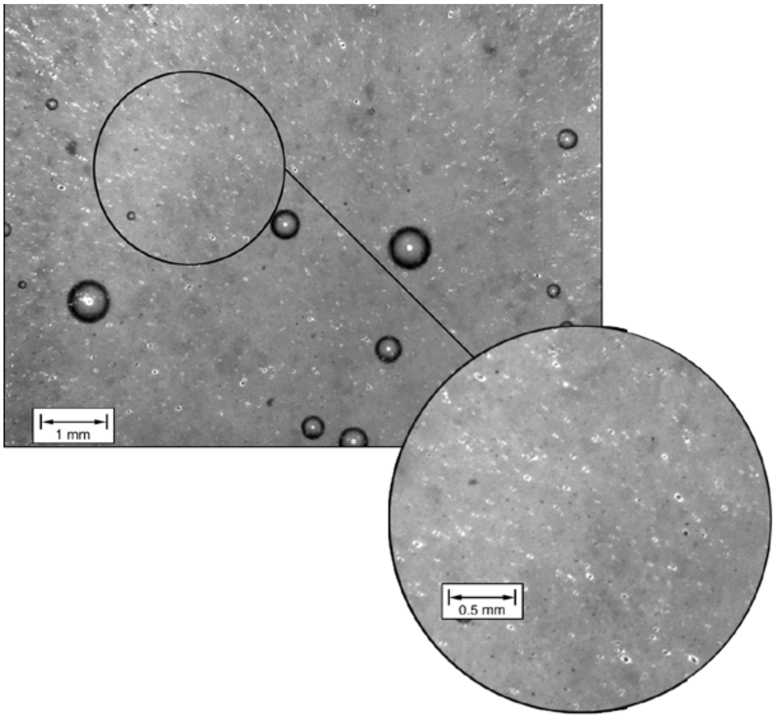

(a)

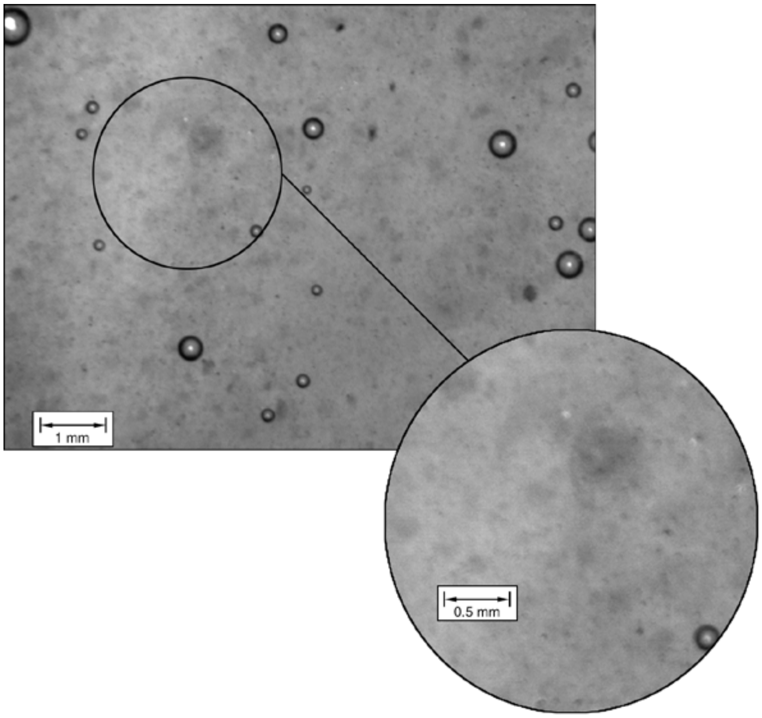

(b)

Figure 3.12: (a) Rippling of the mucus simulant in the 232 mT field, and (b) the surface of the mucus simulant after the magnetic field is removed. The large circles are air bubbles beneath the liquid surface.

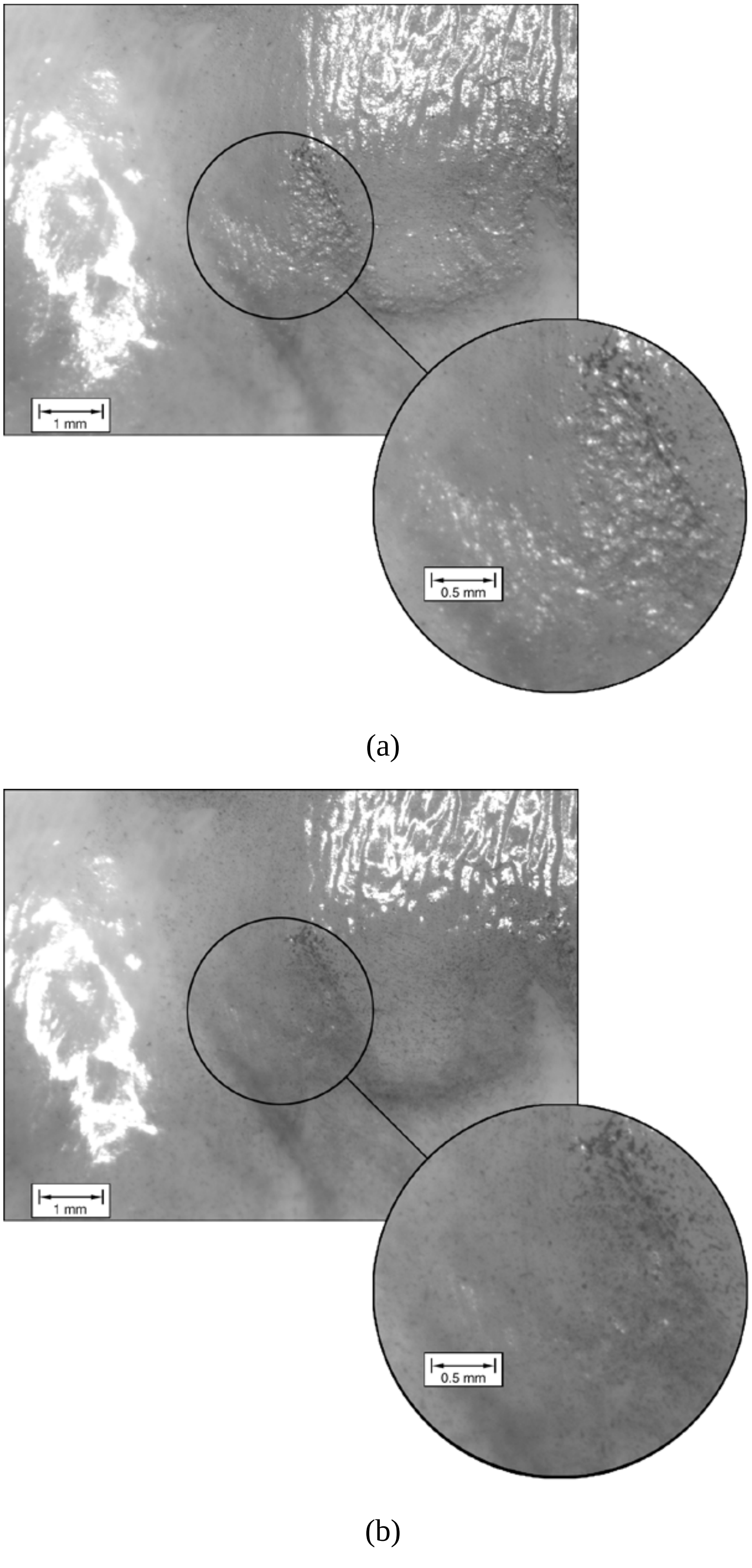

Figure 3.13: (a) Rippling of the frog palate surface in the 232 mT field, and (b) the surface of the frog palate surface after the magnetic field is removed.

The magnetic force pulling the particles and mucus layer into the tissue would likely affect the motion of the cilia in one of two ways. The rate at which the cilia in the region beat may increase, due to the ciliotactile response [9], or the cilia motion could be disrupted due to the increased loading. The cilia propel the mucus layer by beating in metachronal waves; see Sleigh *et al*. for a detailed description of mucus propulsion by cilia [9]. These waves may be disrupted by loading cilia in a region of the palate, causing them to stop or reducing their beat frequency due to increased drag on the individual cilia tips. If the loading due to the magnetic force is enough to disrupt the cilia motion in this manner, the mucus transport in the region around the particles would stop or slow down. This may be the mechanism by which the large iron oxide particles were retained. Figure 3.14 shows iron oxide particles that were successfully retained and then released by removal of the magnetic field on the palate [26]. The iron oxide particles were cleared immediately after the magnetic field was removed, which indicates that, as in the case of the smaller iron particles, they did not completely penetrate the surface. The magnetic force on the iron oxide particle aggregates was larger than on the iron aggregates in spite of the lower magnetic permeability of iron oxide, due to their size. The loading of the cilia due to the magnetic force on the iron oxide particles thus might have been sufficient to disrupt the cilia motion and prevent clearance. Iron oxide particles were also retained in the mucus simulant with the same magnetic field (148 mT). In this case, however, the particles were pulled through the liquid surface, and thus were not cleared once the magnetic field was removed. Since the particles were able to penetrate the surface of the mucus simulant, retention in this case does not shed any light on whether or not the ciliotactile effect was responsible for retention in the *ex vivo* case, as the particles apparently did not penetrate the mucus layer on the frog palate. However, it illustrates that if particles can fully penetrate the mucus layer and “sink” to the tissue level, they would be made to remain at the target site. This could be achieved using a suitably designed magnetic field with an appropriate vertical component.

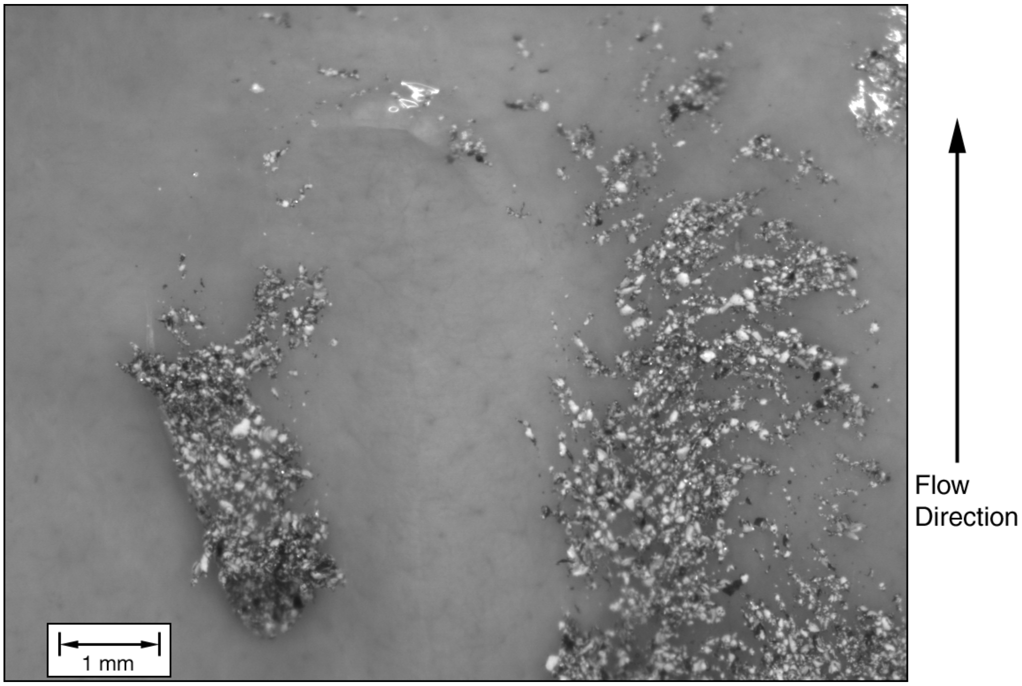

Figure 3.14: Iron oxide particles retained with the 148 mT field on a frog palate with a mucus transport rate of 5 mm/min.

Another reason the iron oxide particles were retained may have been due to their size. The magnetic force is proportional to the volume of the particle, i.e. the third power of the diameter. The drag force is proportional to the immersed surface area of the particle. Since the iron oxide particles characteristic size of ~180 μm and the mucus layer is on ~10 μm thick, only a small portion of the iron oxide particles was immersed. The aggregates formed by the iron particles, 1 – 3 μm in diameter, had a much larger proportion of their surface area immersed. The drag force on the iron aggregates was therefore larger than on the iron oxide particles as compared to the magnetic force.

These results show that viscosity is the most significant parameter in magnetic particle retention at the airway surface. Particle size is a secondary factor, however, the size of particles is limited by the required aerodynamic diameter for particles to reach the conducting airways, i.e 10 μm. One potential approach to overcome the effect of viscosity may be the use of a mucolytic agent. Mucolytic drugs are used to treat conditions such as cystic fibrosis, and are administered to the airways as an inhaled aerosol via nebulizer. A mucolytic delivered along with or prior to the drug particles could reduce the mucus viscosity at the target sites, allowing the particles to be retained by reducing the effect of the drag force and enhancing particle aggregation. The retention may also be compounded by the “sinking” of the particles into the tissue surface. This would also disrupt the mucus transport mechanism at the target site, since the cilia would not be able to push on the mucus. Such an approach may allow magnetic particles to be retained at a target site.

The results also show that particle aggregation increases the chances of retention. This, along with equations (3.3) and (3.4), suggests that increasing the magnetic field strength, regardless of the field gradient, may also improve retention. Increasing the field strength would promote particle aggregation.

Practically, the field strength is constrained by the limits of available magnetic materials, magnet designs, and the allowable magnetic field exposure for humans.

3.5 Conclusions

The results of this chapter indicate that mucus viscosity is the most significant parameter in determining whether magnetic particles can be retained by a magnetic field at a target site in the conducting airways. Particle aggregation and size was also identified as a key parameter for retention. Design of a magnetic field for increased field intensity to increase particle aggregation could also promote retention. The field geometry must also be considered in the design of a magnetic system, since a radial field that concentrates particles in a small region can also promote retention through facilitating better aggregation. The mucus transport rate did not appear to be a determining factor for particle retention as compared to the others studied.

3.6 References:

1. Ally, J., *et al*. 2005. Magnetic targeting of aerosol particles for cancer therapy. J. Magn. Magn. Mater., Vol. 293, pp. 442-449.

2. Lübbe, A.S. and Alexiou, C., Bergemann, C. 2001. Clinical applications of magnetic drug targeting. J. Surg. Res, Vol. 95, pp. 200-206.

3. Forbes, Z.G., *et al*. 2003. An approach to targeted drug delivery based on uniform magnetic fields. IEEE Trans. Magn., Vol. 39, pp. 3372-3377.

4. Grief, A.D. and Richardson, G. 2005. Mathematical modelling of magnetically targeted drug delivery. J. Magn. Magn. Mater., Vol. 293, pp. 455-463.

5. Goodwin, S., *et al*. 1999. Targeting and retention of magnetic targeted carriers (MTCs) enhancing intra-arterial chemotherapy. J. Magn. Magn. Mater., Vol. 194, pp. 132-139.

6. Chen, H., *et al*. 2004. Analysis of magnetic drug carrier particle capture by a magnetizable intravascular stent: 1. Parametric study with single wire correlation. J. Magn. Magn. Mater., Vol. 284, pp. 181-194.

7. Liu, J., Flores, G.A. and Sheng, R. 2001. In-vitro investigation of blood embolization in cancer treatment using magnetorheological. J. Magn. Magn. Mater, Vol. 225, pp. 209-217.

8. Schürch, S., *et al*. 1999. Particles at the airway interfaces of the lung. Colloids and Surfaces B, Vol. 15, pp. 339-353.

9. Sleigh, M.A., Blake, J.R. and Liron, N. 1988. The propulsion of mucus by cilia. Am. Rev. Respir. Dis., Vol. 137, pp. 726-741.

10. Morgan, L., *et al*. 2004. Scintigraphic measurement of tracheal mucus velocity in vivo. Eur. Respir. J., Vol. 23, pp. 518-522.

11. Lourenço, R.V., Klimek, M.F. and Borowski, C.J. 1971. Deposition and clearance of 2 µ particles in the tracheobronchial tree of normal subjects – smokers and nonsmokers. J. Clin. Inv., Vol. 50, pp. 1411-1420.

12. Radoev, B., Nedjalkov, M. and Djakovich, V. 1992. Brownian motion at liquid-gas interfaces. 1. Diffusion coefficients of macroparticles at pure interfaces. Langmuir, Vol. 8, pp. 2962-2965.

13. McKinley, G.H. Steady and transient motion of spherical particles in viscoelastic fluids. [book auth.] D. De Kee and R. Chhabra. Transport processes in bubbles, drops & particles, 2nd Ed. s.l. : Taylor & Francis, 2001, pp. 338-362.

14. Gerber, R. and Birss, R.R. High Gradient Magnetic Separation. England : Research Studies Press, 1983.

15. Henje, K. 1994. The traction force in magnetic separators. Measurement Science and Technology, Vol. 5, pp. 1105-1108.

16. Myint-U, T. and Debnath, L. Partial differential equations for scientists and engineers. New Jersey, USA : P T R Prentice-Hall, Inc., 1987.

17. Aziz, J.J., Serra, C.A. and Wiesner, M.R. 2003. Hydrodynamics of permeable aggregates in differential sedimentation. Environ. Eng. Sci., Vol. 20, pp. 21-31.

18. Iimura, K. and Higashitani, K. 2005. Simulation of hydrodynamic drag force on aggregates. Advanced Powder Technol., Vol. 16, pp. 87-96.

19. King, M., Brock, G. and Lundell, C. 1985. Clearance of mucus by simulated cough. Journal of Applied Physiology, Vol. 58, pp. 1776-1782.

20. Rubin, B.K., Ramirez, O. and King, M. 1990. Mucus-depleted frog palate as a model for the study of mucociliary clearance. J. Appl. Physiol., Vol. 69, pp. 424-429.

21. King, M. 1998. Experimental models for studying mucociliary clearance. Eur. Respir. J., Vol. 11, pp. 222-228.

22. Zayas, J.G., *et al*. 2004. Adaptation of an amphibian mucociliary clearance model to evaluate early effects of tobacco smoke exposure. Resp. Res., Vol. 5, p. 9.

23. King, M. and Macklem, P.T. 1977. Rheological properties of microliter quantities of normal mucus. J. Appl. Physiol., Vol. 42, pp. 797-802.

24. Wang, Z.L., Lange, C.F. and Finlay, W.H. 2004. Use of an impinging jet for dispersion of dry powder inhalation aerosols. Int. J. Pharm., Vol. 275, pp. 123-131.

25. Voss, A. and Finlay, W.H. 2001. Deagglomeration of dry powder pharmaceutical aerosols. Int. J. Pharm., Vol. 248, pp. 39-50.

26. Model studies of magnetic particle retention in the conducting airways. Ally, J., Amirfazli, A. and Roa, W. [ed.] W. Badawy and W. Moussa. Los Alamitos, USA : IEEE Publications, 2005. Proc. ICMENS 2005, Banff, Canada. pp. 182-184.

Chapter 4: Use of mucolytics to enhance magnetic particle retention at a model airway surface[*]

Targeted delivery of magnetic particles to the circulatory system and various regions of the body has been studied widely in the literature. Applications of magnetic targeting have included the used of magnetic fields to retain particles in blood vessels [1], the used of magnetic stents [2], particle embolization to restrict blood flow to tumors [3], and various other studies of magnetic targeting methods [4-6]. In contrast, magnetic targeting of particles to the airways with the long-term goal of effective treatment for cancer has been studied only very recently [7-9].

Aerosolized drug delivery to the lung bypasses the circulatory system, which can result in reduced side effects in other organs as demonstrated using an animal model [9] and also in humans [4]. However, indiscriminate delivery of drugs can have adverse effects for the lung's healthy tissue and increase costs of therapy. Treatable cancer is a region-specific ailment, and as such the most effective treatment also needs to be locale specific.

The idea of using a magnetic field to target aerosolized particles to a specfic location in the airway system was first demonstrated *in vitro* [7] and then in an *ex vivo* model [8]. From these studies, it became clear that there are two components to the targeted delivery of an aerosol; first, targeted deposition of the aerosol particles in a desired region, and second, retention of magnetic particles deposited at a target site. The focus of this chapter is on the second component.

---

[*] A version of this chapter has been published. Ally, Roa, Amirfazli 2008. Journal of Magnetism and Magnetic Materials. 320: 1834-1843.

For magnetically targeted drug delivery to the airways to be effective, the mucus clearance mechanism in the airways must be overcome to ensure that drug particles are retained in sufficient quantities in the cancerous regions of the airways, and to prevent damage to healthy tissue. Previously [8] it was found that prohibitively strong magnetic fields, greater than those produced by typical commercial Nd-Fe-B magnets, are required to retain particles at the airway surface, which may not be practical for design of a magnetic targeting system. In this chapter, mucolytics are used to reduce mucus viscoelasticity and determine whether this will allow more moderate fields to be used.

Schürch *et al*. [10] and others have studied the behavior of nonmagnetic particles at the airway surface. However, the problem of magnetic particle retention in the conducting airways has only been studied very recently [8]. In this chapter, similar to [8], the conducting airways modeled are the trachea and bronchi only.

The conducting airway surface is characterized by a layer of viscoelastic mucus that flows atop a watery periciliary layer (Figure 4.1). The mucus layer is typically ~5 – 10 μm thick; the thickness of the periciliary layer is ~5 – 7 μm [11]. The elastic component of the mucus viscoelasticity enables the mucus layer to be propelled toward the larynx by the beating action of the cilia on the underlying cellular epithelium. In a healthy adult, the mucus transport velocity in the trachea is approximately 7 – 14 mm/min [12]. The mucus thickness and transport velocity can substantially vary depending on the health of the airways.

A surfactant film has also been shown to be present at the air-liquid interface of the airways [10], reducing the surface tension of the mucus.

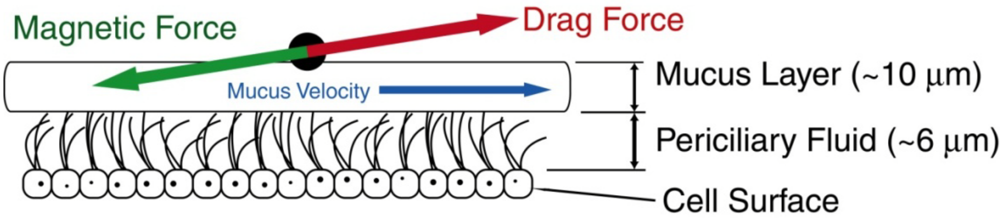

Figure 4.1: Airway surface schematic

Particles that deposit in the conducting airways are entrained in the mucus layer and removed. Particles deposited in the trachea and bronchi area may be cleared in as little as 1 hour in healthy subjects [13]. The mucociliary clearance mechanism has the specific function of clearing particles, e.g. dust or bacteria. As such, retention of magnetic particles in the airways is fundamentally different from the circulatory system, which has been widely studied.

For the particle sizes and speeds considered in these experiments, the shear rates are extremely low. Thus, although mucus is a viscoelastic fluid, for the purpose of the following discussion, the mucus viscosity may be considered as equal to the zero-shear rate apparent viscosity.

Mucus viscoelasticity has been identified as the most significant factor that must be overcome for magnetic particle retention in the airways [8]. To realize particle retention at moderate field strengths, such as those achievable with commercially available permanent magnets, a reduction of mucus viscoelasticity is needed. This could be achieved by application of mucolytics in conjunction with, or prior to, introduction of magnetically susceptible particles to the airways. In general, mucolytics are used to treat various abnormal conditions in the conducting airways such as cystic fibrosis. Mucolytics function by breaking chemical bonds in mucus, and thus reducing its viscosity and rigidity. Two mucolytic agents, dextran sulfate (DS) and N-acetylcysteine (NAC), are used in this chapter to reduce mucus viscoelasticity and study their application for particle retention using magnetic force.

4.1 Theoretical Background

Particles are retained at the airway surface when the magnetic force on the particles balances the drag force due to the moving mucus layer (Figure 4.1). In a magnetic field, magnetic particles tend to form large aggregates upon deposition; the forces on aggregates cannot be accurately computed without a model for aggregate geometry. Nevertheless, the parameters governing the drag and magnetic forces should be similar to those governing the motion of single spherical particles. The equations for the drag and magnetic forces on a spherical particle are thus presented in this section to identify the relevant parameters.

For sufficiently small spherical particles partially immersed in a Newtonian fluid, the drag force is given by [14]:

$$\vec{\boldsymbol{F}}_{\boldsymbol{D}} = -3\pi\eta d\vec{\mathbf{v}}_{\boldsymbol{rel}}\, y(\theta) \quad (4.1)$$

where $\vec{\boldsymbol{F}}_{\boldsymbol{D}}$ is the drag force, d is the particle diameter, η is the fluid viscosity, $\vec{\boldsymbol{v}}_{\boldsymbol{rel}}$ is the relative velocity of the particle with respect to the fluid, and y is a scaling factor depending upon the particle contact angle θ. In studies by Schürch *et al*. [10] it has been shown that small particles tend to be pulled into the mucus layer due to a layer of surfactant on it. Large particles and aggregates, on the other hand, would still only be partially immersed. In either case, the parameters governing the magnitude of the drag force on partially or fully immersed particles (viscosity, relative velocity, and particle size) are the same; as such, surface force effects are not considered here. The drag force in the Stokes flow regime due to a viscoelastic fluid such as airway mucus must be calculated by applying a correction factor to (4.1). However, the same parameters that determine the drag force on a particle in a Newtonian fluid, i.e. particle size, relative velocity, and steady-state viscosity of the fluid will also determine the drag force in a viscoelastic fluid [15].

The drag force must be balanced by the magnetic force on the particles for retention. For particles with a high magnetic susceptibility, such as the iron particles used in these experiments, and small enough to be considered as a point in the magnetic field, i.e. the field strength and gradient do not vary over the particle diameter, the magnetic force is given by the following equation [16]:

$$\vec{\boldsymbol{F}}_{\boldsymbol{M}} = 3\mu_0 V_p \vec{\boldsymbol{H}} \nabla \vec{\boldsymbol{H}} \qquad (4.2)$$

where $\vec{\boldsymbol{F}}_{\boldsymbol{M}}$ is the magnetic force, μ_0 is the magnetic permeability of vacuum, V_p is the particle volume, and $\vec{\boldsymbol{H}}$ is the magnetic field intensity at the particle location. As a result of the magnetic field term $\vec{\boldsymbol{H}} \nabla \vec{\boldsymbol{H}}$, the field must have a gradient to exert any magnetic force on a small particle.

Considering individual particles is unrealistic, since particles will aggregate in a magnetic field, primarily due to the local distortion of the field by individual particles. Each particle creates a local field gradient, causing other particles to be attracted and subsequently forming aggregates. The closer the particles are to one another, the greater the attraction between them due to the increased field gradient. As the aggregates grow, they further distort the field, thus attracting more particles, until a minimum energy configuration, representing an equilibrium, is formed.

The magnetic force on aggregates is difficult to compute due to the distortion of the magnetic field by the particles and nonlinearity of the expression for magnetic force. It is reasonable to assume, however, that the magnetic force on an aggregate of magnetic particles is related to the same variables as the magnetic force on a single particle, i.e. the magnetic susceptibility of the aggregate, aggregate volume, and field intensity and geometry.

The major factors in magnetic particle retention were identified in [8]. Mucus viscoelasticity was deemed the most significant factor. The drag force on particle aggregates is directly proportional to the mucus viscoelasticity. Also, given a particular particle size distribution, concentration, and magnetic field, the aggregate size is a function of the mobility of individual particles, which is affected by the mucus viscoelasticity. Hence, the mucus viscoelasticity is significant as it has both a direct effect on aggregate drag, and an indirect effect through determining the size of the aggregates in the first place. The magnetic force on particle aggregates increases with aggregate size. Therefore, the magnetic force on particle aggregates is also indirectly affected by the mucus viscoelasticity. The magnetic field strength and gradient are also important factors, as they determine the magnetic force on the particles (or aggregates). The mucus transport rate does not appear to be a significant factor in particle retention in the airways, as the results presented in [8] did not vary for the transport rates examined over two orders of magnitude. This was further confirmed in this chapter.

Mucolytics were used in these experiments to determine if altering the viscoelastic properties of the mucus could enhance or aid in particle retention. Mucus consists of a water-based gel that derives its viscoelasticity from a three-dimensional network of crosslinked glycoproteins [17]. This network is held together by various types of bonds, including covalent, ionic, and hydrogen bonds; van der Waals forces; and physical entanglement of the glyoproteins [17]. Mucolytics reduce the viscoelasticity of mucus by altering these interactions.

The two mucolytics used were N-acetylcysteine (NAC) and dextran sulfate (DS). N-acetylcysteine is a direct-acting mucolytic that functions by reducing disulfide bonds, decreasing the amount of cross-linking of the mucus, and thus reducing both the viscosity and elasticity of the mucus [18]. In some cases, NAC has been shown to reduce mucus viscoelasticity excessively, reducing mucus clearance [17]. Dextran sulfate is a nondestructive mucolytic that interferes with ionic charge interactions and hydrogen bonding, and thus reduces mucus viscosity and elasticity without reducing the length of the polymer chains [17, 18].

4.2 Methods

The *ex vivo* model used in this chapter to simulate the airway surface is the excised bullfrog (*Rana catesbeiana*) palate. This animal model is used extensively in the literature to simulate the surface of the human airway [19]. Both the chemical structure of the mucus and ciliary motion are similar to that in human airways [20].

The procedures used to harvest the frog palates are based on [19] and [20]. The *Rana catesbeiana* palates were harvested after pithing by decapitating the frogs and removing the lower jaw. The palates were washed with saline solution and then left for two days at 4°C to allow the mucus transport rate to slow to values similar to those in human airways. Due to the possibility of permanent effects of the mucolytics applied on palate clearance, each palate was only used for a single experiment. All procedures involving live animals were approved by the University of Alberta Animal Protection and Welfare Committee.

The palates were treated with mucolytics prior to particle deposition. The concentrations of NAC and DS were 20%wt and 65%wt, respectively, both in water. The concentrations used are based on typical values for each mucolytic found in the literature for studies of mucus clearance [17, 21]. In each experiment, 1 mL of the mucolytic tested was applied as a 4×4 array of drops, spaced approximately 0.5 cm apart on the palate surface. Water was also used for control experiments to determine the effect of adding liquid to the palate, aside from any mucolytic effects. Particles were deposited, as described below, on the palate five minutes after application of the mucolytic.

The experimental apparatus is shown schematically in Figure 4.2. The palate was placed on a petri dish, and observed from above with a CCD camera and lens. The camera field of view was 12 mm × 10 mm. Magnetic fields were applied by placing magnets below the petri dish. Particles were captured from aerosol onto the palates using a magnetic field, as demonstrated in [7]. The motion of the particles on the palates was observed by capturing images from the camera. Images of the deposition phase of the experiments were captured every 0.1 s for 10 s. Images of the retention phase were captured every 10 s for 20 minutes. If particles were retained, the magnetic field was removed after the retention phase to observe whether or not the particles were cleared. A nebulizer was used during the experiments to prevent the palates from drying out. The nebulizer was temporarily switched off during particle deposition to prevent interference with the aerosol flow.

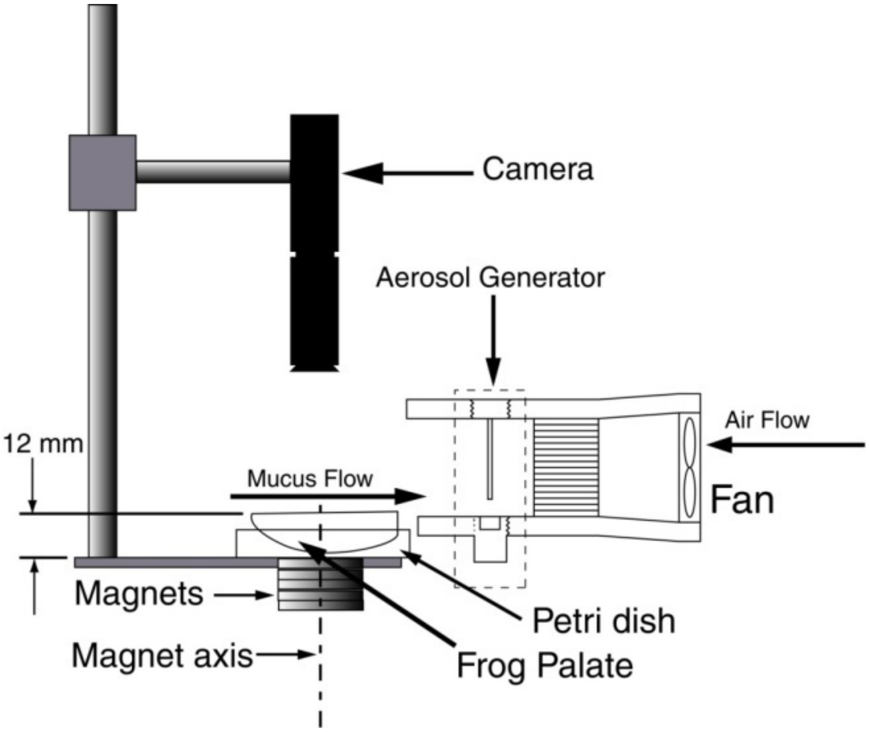

Figure 4.2: Experimental Apparatus

The magnetic fields were applied using disk-shaped (25 mm diameter, 3 mm thickness) neodymium-iron boron magnets. For deposition of particles, a single magnet was placed below the petri dish in all experiments (see Figure 4.2). The axis of the magnet was aligned with the camera axis, so that the center of the field was at the center of the camera's field of view. For retention of particles, a single magnet and a stack of twenty disk magnets were used in various experiments. The distance between the pole of the magnets and the palate surface was maintained at 12 mm for all experiments (Figure 4.2). For the two magnets used, the relative strength of the magnetic force pulling the particles into the palate surface is indicated by the field strength and gradient of the magnetic field along the magnet axis, 12 mm from the magnet pole. For the single disk magnet, the field strength was 116 mT, and the gradient along the axis was 2.5 T/m. For the stack of twenty magnets, the field strength was 148 mT, and the gradient was 10.2 T/m. These values will be used in the discussion to characterize the magnetic fields, however, they are only a relative indication of field strength, and in fact vary over the palate surface.

The magnetic fields used in these experiments can also be considered in terms of their axial and radial components. The axial component of the field is the component along the camera axis and symmetry axis of the magnets (Figure 4.2). The axial component of the field is responsible for the magnetic force pulling the particles towards the pole of the magnet, and thus into the palate surface. The radial component of the magnetic field is perpendicular to the axial component, directed toward the center of the magnetic pole in the observed plane. The radial component of the magnetic force acts on any magnetic particles in the field, resulting in the magnetized particles moving to the region of greatest flux density. Without any liquid flow, the particles would tend to move toward the highest-potential region i.e. the center of the field of view. As such, the radial component of the magnetic force increases particle aggregation. Both components of the magnetic force are important for particle retention, as discussed in the next section.

The particles used in the experiments were iron spheres, with an average diameter between 1 and 3 μm according to the manufacturer's specifications (Alfa Aesar). The particle size distribution in the aerosol was likely significantly different due to particle aggregation. The aerosol was produced by dispersing the particles with a jet of compressed air, as described in [22] and [23]. The particles were entrained in a flow of air passing over the palate produced by the fan, simulating inhalation (see Figure 4.2). For deposition, the 116 mT magnetic field was used to cause particles to deposit on the palate. This field was used for deposition in all experiments to aim for consistent particle deposition on the palate. In a number of experiments the 116 mT field was used for retention as well, and the magnet was left in place. For experiments without any magnetic field or with the 148 mT field, the single magnet was removed, and in case of the 148 mT field replaced with the stack of twenty magnets. The amount of time required to switch the magnets was less than 10 s, which is negligible with respect to the mucus clearance rates observed. The particle concentration in the region of interest was thus not changed significantly, although the aggregate structure was disrupted and re-formed when switching magnets.

The mucus transport rate was measured prior to each experiment, before applying any mucolytic, by placing a 1 mm × 1 mm piece of waxed paper on the palate, and capturing images every second of its movement. A 0.25 mm pitch grid was superimposed over the captured images to measure the distance traveled.

4.3 Results

Table 4.1 shows the results of the control experiments where palates were treated with water instead of a mucolytic, in order to control for the effect of adding a liquid to the palate surface. The water added wetted the mucus layer, and appeared to be absorbed into the palate surface. With no magnetic field and with the 116 mT field applied, the clearance of particles from the palates did not appear affected by the addition of water. In both these cases, particles were cleared from the palate. Addition of 1 mL water to the palate surface in the absence of a magnetic field did not appear to have any effect on mucus transport.

Table 4.1: Results of control experiments using water with and without a magnetic field

Specimen #	**Initial transport rate (mm/min)**	**Transport rate after water applied (mm/min)**	**Field Strength (mT)**	**Field Gradient (mT/mm)**	**Results**
1	4.5	4.5	0	0	particles cleared
2	3.0	3.0	0	0	particles cleared
3	5.5	5.5	0	0	particles cleared
4	6.0	not measured	116	2.5	particles cleared
5	14.0	not measured	116	2.5	particles cleared
6	9.0	not measured	116	2.5	particles cleared

Table 4.2 summarizes the results of control experiments with mucolytic-treated palates with no magnetic field applied for retention. These results show the effect of the mucolytics on mucus transport. The application of mucolytics to the palates resulted in similar absorption as seen when water was added. Significant disruption of mucus transport was observed when palates were treated with NAC. Without any magnetic field applied, clearance of deposited particles from the palate appeared weak and non-directional after application of NAC. The particles in these cases tended to circulate randomly on the palate surface.

Table 4.2: Results of control experiments where a mucolytic is applied without a magnetic field

Specimen #	**Mucolytic**	**Initial transport rate (mm/min)**	**Tranport rate after mucolytic applied (mm/min)**
7	NAC	10.5	weak and nondirectional
8	NAC	12.0	weak and nondirectional
9	NAC	4.5	weak and nondirectional
13	DS	2.5	2.8
14	DS	12	12
15	DS	7.6	8.2

The results of experiments with the mucolytics and a magnetic field applied are presented in Table 4.3. With the 116 mT magnetic field applied to the NAC-treated palates, particles were clearly retained, as illustrated in Figure 4.3. Examining a series of images similar to Figure 4.3(a) and Figure 4.3(b), it was concluded that the motion of particles after deposition primarily resulted in aggregation due to the magnetic force between particles; the aggregates themselves were also aligned with the magnetic field. Since a magnetic field is used to deposit particles on the palate, aggregates begin to form during the deposition process, hence the initial appearance of the particle aggregates as short lines aligned with the magnetic field used for deposition. Movement of particles, as seen without a magnetic field applied to NAC-treated palates did not occur, indicating that the applied magnetic field of moderate strength was sufficient to immobilize the particles for a weakened mucus transport mechanism. After the magnetic field was removed, no particle motion was observed (Figure 4.3(c)). Since retention was observed with the 116 mT field, higher magnetic fields were not tested with NAC-treated palates.

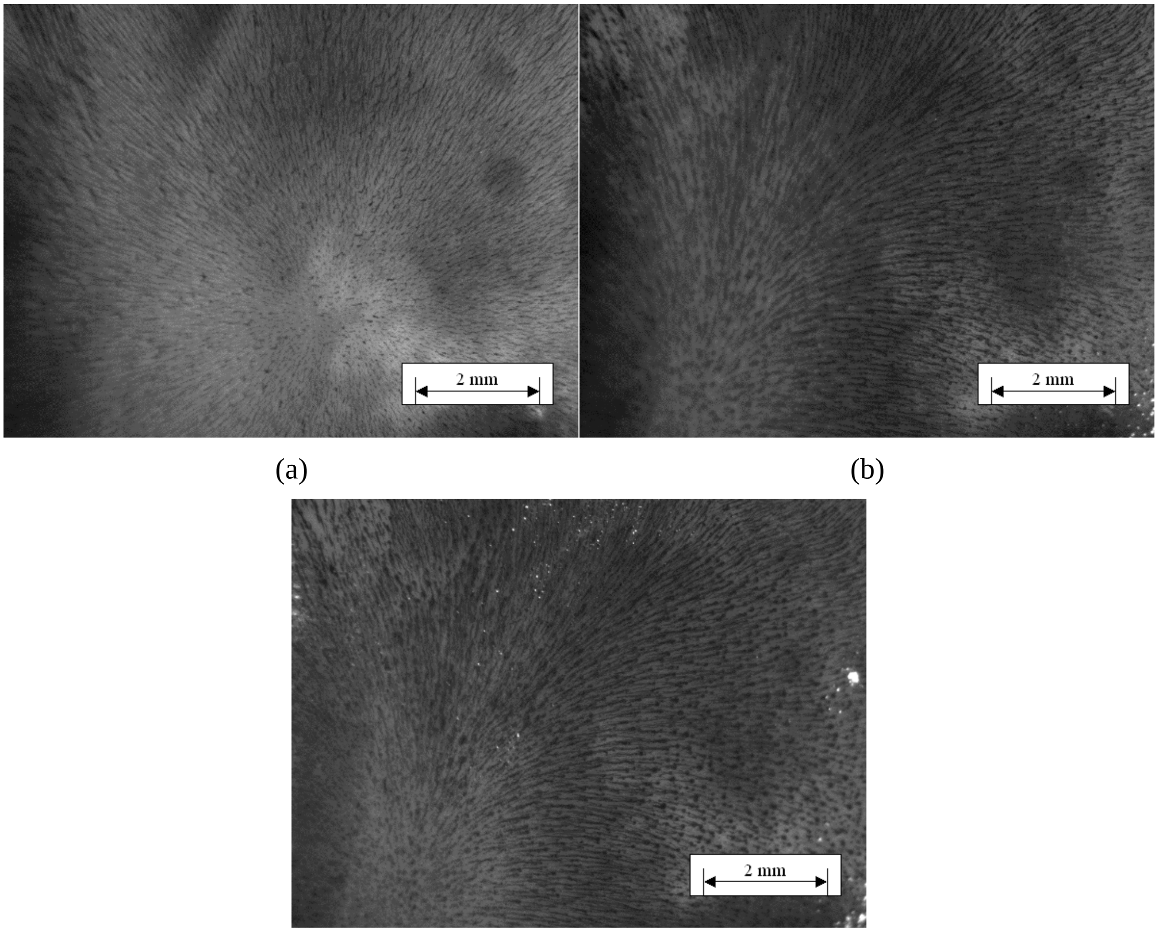

(a) (b)

(c)

Figure 4.3: Particles (dark spots dotting images shown) deposited on a NAC-treated palate (a) 10 s after deposition, (b) 5 minutes after deposition, and (c) 3 minutes after the magnetic field was removed. The white spots are reflections due to rippling of the mucus on the palate surface.

Table 4.3: Results of application of magnetic field to mucolytic-treated palates

Specimen #	**Initial transport rate (mm/min)**	**Field Strength (mT)**	**Field Gradient (mT/mm)**	**Mucolytic**	**Results**
10	5.6	116	2.5	NAC	particles retained
11	4.5	116	2.5	NAC	particles retained
12	7.6	116	2.5	NAC	particles retained
16	3.8	116	2.5	DS	particles cleared
17	12.8	116	2.5	DS	particles cleared
18	1.5	116	2.5	DS	particles cleared
19	3.0	148	10.2	DS	particles retained
20	0.5	148	10.2	DS	particles cleared
21	2.3	148	10.2	DS	small amount of particles retained

In the case of the DS-treated palates, with the 116 mT field applied, no particle retention was observed, as was the case with untreated palates. When a 148 mT field was used, the results seen were not consistent. The retention of particles seems to be related to the area density of particles initially deposited on the palate surface. In the case of specimen 19, the initial particle deposition is denser (per unit area) than for specimens 20 and 21, as shown in Figure 4.4.

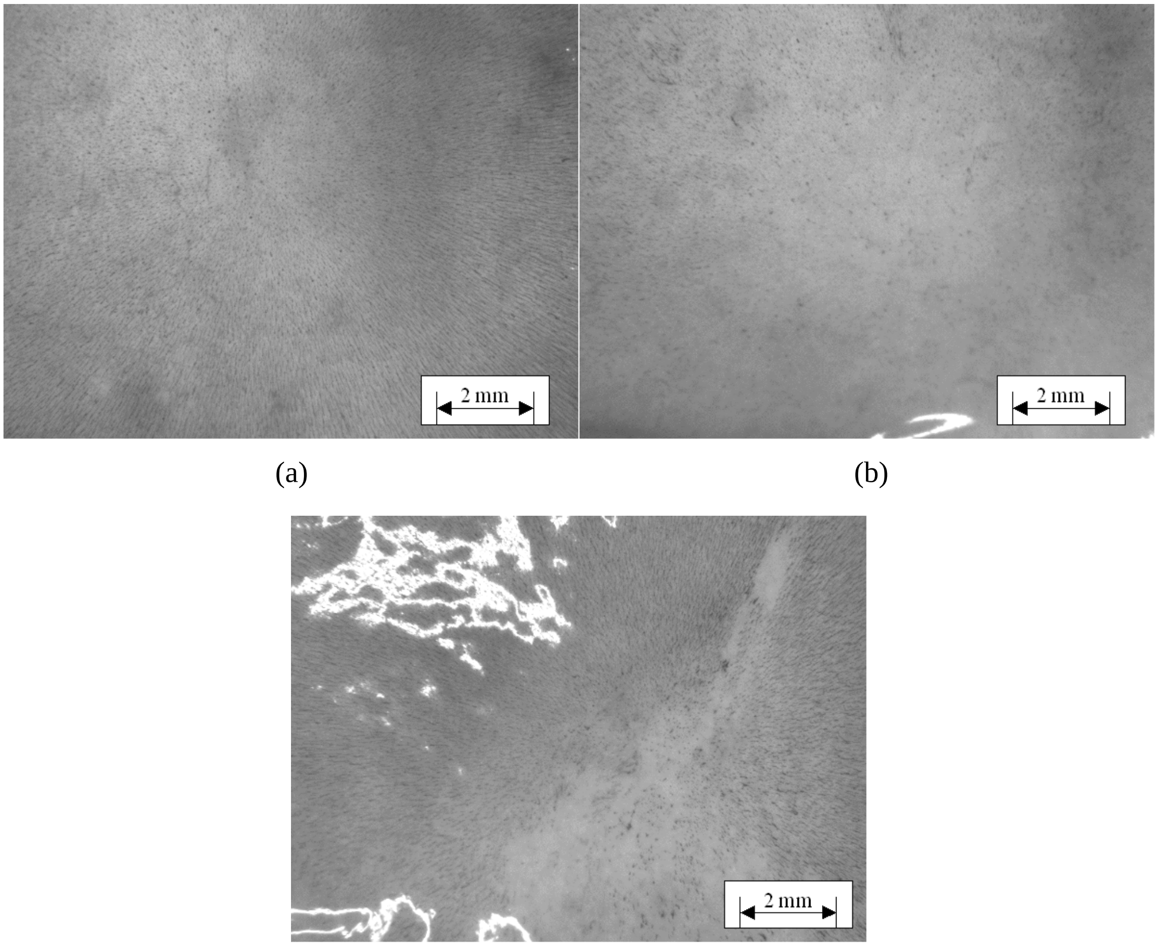

(a) (b)

(c)

Figure 4.4: Initial particle deposition on specimen (a) 19, (b) 20, and (c) 21. The images show the differences of the initial deposition of the particles (dark spots). The white spots are reflections due to rippling of the mucus on the palate surface.

4.4 Discussion

These random, circulating motions of particles on the NAC-treated palates show that the ciliated surfaces of the palates was still active, but that effective mucus clearance could not be achieved due to the reduction of the mucus viscoelasticity resulting from application of NAC. This is consistent with the effects of NAC reported in the literature [17]. The coupling between the mucus layer motion and ciliary motion is a result of mucus elasticity [24], since the mucus elasticity allows the cilia to push on the mucus layer, as discussed previously. The DS-treated palates did not exhibit the disruption of mucus transport seen in the NAC-treated palates. With no magnetic field applied, the mucus transport rate appeared unaffected by the addition of DS. In the literature, dextran sulfate is associated with slightly enhanced mucus transport [17], so the results in Table 4.2 are somewhat consistent with the available information. Overall, the results of the control experiments shown in Table 4.1 and Table 4.2 suggest that in order to immobilize (hold) particles at the airway surface, an external means, e.g. a magnetic field is required.

The effect of NAC on the mucus viscoelasticity can be seen from the size of the particle aggregates formed on the NAC-treated palates. The size of the aggregates formed by the deposited particles is an indicator of mucus viscoelasticity, as discussed previously. The aggregates formed on the NAC-treated palates were generally larger than those seen on untreated palates. This can be seen by comparing Figure 4.5(a) and Figure 4.5(b). Whereas the number of aggregates is somewhat greater in Figure 4.5(a), the size of individual aggregates is larger in Figure 4.5(b). Further aggregation of the particles was observed during the retention phase of the experiments with the NAC-treated palates (cf. Figure 4.3(a) and Figure 4.3(b)). Comparing the aggregates formed on the NAC-treated palates to previous *in vitro* results in [8], the aggregates were most similar in size to those formed by particles deposited on the liquid surface of a model using glycerol as the clearing liquid (Figure 4.5(c)). This indicates that the NAC reduced the viscoelasticity of the mucus significantly. This reduction in mucus viscosity is the most likely cause of the non-directional motion of the mucus layer observed in the absence of a magnetic field mentioned above. A magnetic field is still required in spite of the disruption of the clearance mechanism, as in actual airway conditions, this disruption would only be temporary.

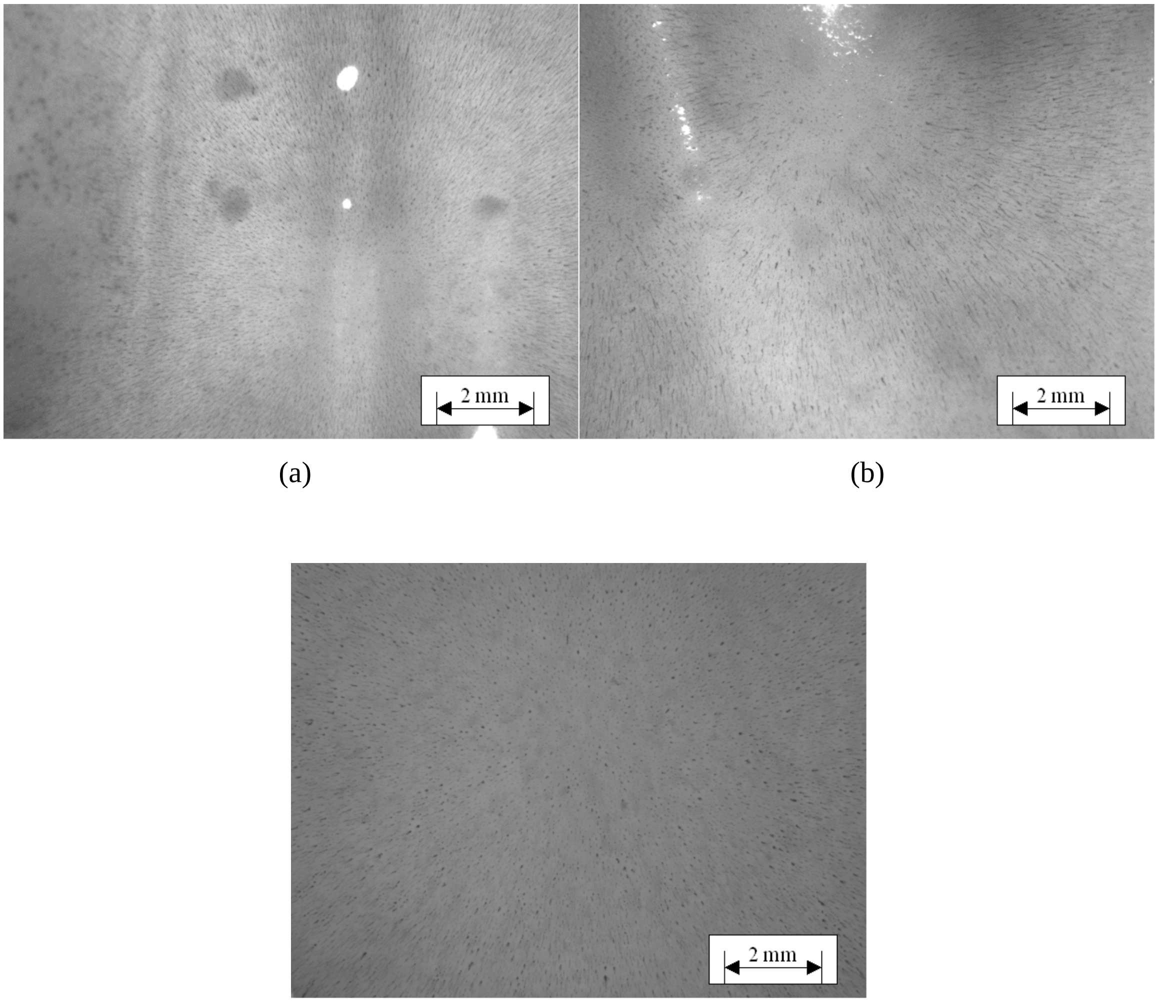

(a) (b)

(c)

Figure 4.5: Particle aggregates (dark spots) formed 10 s after deposition on (a) an untreated palate, (b) a NAC-treated palate, and (c) an in vitro glycerol flow using the 116 mT magnetic field. The white spots are reflections due to rippling of the mucus on the palate surface.

The retention of magnetic particles can be considered as a combination of the effects of the axial and radial components of the magnetic force on the particles and particle aggregates. The axial component of the magnetic force pulls the particles into the palate surface, toward the magnet pole. This causes loading of the cilia beneath the mucus layer, which contributes to particle retention; it is argued that such loading can lead to disruption of the mucociliary clearance mechanism [24]. The radial component of the magnetic force causes particles to move towards the point of maximum field strength, at the center of the magnetic fields used in these experiments. This tends to draw particles from peripheral regions of the magnetic field to the center of the field, forming larger aggregates, as seen by comparing the apparent particle densities Figure 4.3(a) and Figure 4.3(b). This aids in particle retention as the increased aggregate size leads to higher magnetic force and subsequently increased loading of the cilia. The increased magnetic force also allows the drag force to be overcome by the radial component of the magnetic force. The combined effects of the two components of the magnetic force suggest two possible mechanisms for the observed immobilization of particles on the NAC-treated palates. First, it is possible that the mucociliary clearance mechanism is completely disrupted as follows: The particle aggregates were larger on NAC-treated palates than on untreated palates, and thus the magnetic force on the aggregates would also have been larger. This would increase the load of the mucus layer on the cilia, overcoming the ability of the cilia to propel the mucus layer. The mucus layer is pulled towards the tissue (due to the axial component of the magnetic force acting on the particle aggregates), resulting in a larger portion of each cilium being pushed into the mucus layer, reducing the effectiveness of the ciliary motion. The disruption of ciliary motion could also alter the hydrodynamic interactions between nearby cilia, resulting in uncoordinated beating of the cilia and thus ineffective mucus transport even after the magnetic field was removed. This could explain the non-clearance of particles after the magnetic field was removed. Consequently, the axial component of the magnetic force would result in stoppage of mucociliary clearance as the cilia could not move effectively to propel the mucus layer. A second explanation is that the particle aggregates were pulled through the mucus layer into the periciliary layer and thus were not re-entrained into the flow of mucus after that magnetic field was removed. If the particles are pulled through the mucus layer into the tissue beneath, this could be quite beneficial for drug delivery purposes. Further experimental study is required to determine whether or not penetration of the mucus layer by the particle aggregates actually occurs.

The inconsistency observed in the results for the DS-treated palates may be due to variations in the initial particle concentration. Increasing the particle concentration initially deposited on the palate leads to larger particle aggregates, since the average distance between deposited particles is reduced for increased concentrations. Inter-particle magnetic forces increase as the distance between particles decreases, and thus the more concentrated the initial deposition of particles is, the larger the aggregates formed, and the greater the magnetic force on the aggregates. The drag force is also greater on larger aggregates, however, the increase in magnetic force is more significant since the magnetic force increases with particle volume, i.e. the cube of the diameter, whereas the drag force increases with particle diameter. In [8], such variations in initial concentration showed no effect in retention of particles on untreated palates using the 148 mT magnetic field. The effect of the variations in initial particle concentration in this case can be attributed to the reduction of the mucus viscoelasticity by DS. Reduction of the mucus viscoelasticity enhances particle retention by reducing the drag force on the particles, and by allowing larger particle aggregates to develop. Since the magnetic force on the aggregates increases with size, large aggregates are more likely to be retained than small aggregates. Since the only difference between the DS-treated palate and 148 mT and all other experiments is the mucolytic used and magnetic field applied after deposition, it is likely that the initially deposited area concentration of particles varied in all cases. Only in the particular case of the DS-treated palates in the 148 mT magnetic field did the combination of the magnetic field and the reduced mucus viscoelasticity due to DS appears to produce a condition where particle retention is sensitive to the initial particle concentration.

The particle aggregates formed after deposition on the DS-treated palates were smaller than those formed on the NAC-treated palates. Also, after deposition, there did not appear to be any further aggregation on the DS-treated palates. This implies that DS did not reduce the mucus viscoelasticity to the extent that NAC did, as does the fact that DS did not disrupt the mucus transport as did NAC (see Table 4.2).

In the case of specimen 19 where the particles were retained on the DS-treated palate using the 148 mT field, the particles began to clear from the palate after the 148 mT field was removed. This indicates that the mucus transport mechanism was still operating, and that the retention observed was due primarily to the balance between the magnetic and drag forces on the particles, and not due to the disruption of the mucus transport mechanism (as with the NAC-treated specimen). The particle clearance after the magnetic field was removed also indicates that the particles did not penetrate the mucus layer.

4.5 Conclusions

This chapter has shown that the administration of mucolytics in conjunction with magnetic particles allows the particles to be retained on the frog palate surface by moderate magnetic fields. This result suggests that the use of mucolytics has the potential to allow magnetic particle retention in the airways with moderate magnetic fields. Further investigation is required in order to determine appropriate dosages. Particles were retained by a moderate-strength magnetic field (116 mT, 2.5 T/m) on an NAC-treated palates. NAC was effective partly due to the reduction of mucus viscoelasticity, and partly due to the resulting disruption of mucus transport.

The retention mechanism observed due to Dextran sulfate was somewhat different than NAC. Particle retention on DS-treated palate depended on the concentration of initially deposited particles on the palate surface. Higher initial particle concentrations resulted in retention of particles (larger aggregates formed and acted upon by larger magnetic force), whereas low initial particle concentration did not allow particle retention. The NAC-treated palate results were independent of initial particle concentration. Further fundamental studies on the effects of particle concentration and aggregation at fluid interfaces are rare, and therefore needed as the next steps.

4.6 References

1. Goodwin, S., *et al*. 1999. Targeting and retention of magnetic targeted carriers (MTCs) enhancing intra-arterial chemotherapy. J. Magn. Magn. Mater., Vol. 194, pp. 132-139.

2. Chen, H., *et al*. 2004. Analysis of magnetic drug carrier particle capture by a magnetizable intravascular stent: 1. Parametric study with single wire correlation. J. Magn. Magn. Mater., Vol. 284, pp. 181-194.

3. Liu, J., Flores, G.A. and Sheng, R. 2001. In-vitro investigation of blood embolization in cancer treatment using magnetorheological. J. Magn. Magn. Mater, Vol. 225, pp. 209-217.

4. Lübbe, A.S. and Alexiou, C., Bergemann, C. 2001. Clinical applications of magnetic drug targeting. J. Surg. Res, Vol. 95, pp. 200-206.

5. Forbes, Z.G., *et al*. 2003. An approach to targeted drug delivery based on uniform magnetic fields. IEEE Trans. Magn., Vol. 39, pp. 3372-3377.

6. Grief, A.D. and Richardson, G. 2005. Mathematical modelling of magnetically targeted drug delivery. J. Magn. Magn. Mater., Vol. 293, pp. 455-463.

7. Ally, J., *et al*. 2005. Magnetic targeting of aerosol particles for cancer therapy. J. Magn. Magn. Mater., Vol. 293, pp. 442-449.

8. Ally, J., Amirfazli, A. and Roa, W. 2006. Factors affecting magnetic retention of particles in the upper airways: an in vitro and ex vivo study. Journal of Aerosol Medicine, Vol. 19, pp. 491-509.

9. Dames, P., *et al*. 2007. Targeted delivery of magnetic aerosol droplets to the lung. Nat. Nanotechnol., Vol. 2, pp. 495-499.

10. Schürch, S., *et al*. 1999. Particles at the airway interfaces of the lung. Colloid Surf. B, Vol. 15, pp. 339-353.

11. Sleigh, M.A., Blake, J.R. and Liron, N. 1988. The propulsion of mucus by cilia. Am. Rev. Respir. Dis., Vol. 137, pp. 726-741.

12. Morgan, L., *et al*. 2004. Scintigraphic measurement of tracheal mucus velocity in vivo. Eur. Respir. J., Vol. 23, pp. 518-522.

13. Lourenço, R.V., Klimek, M.F. and Borowski, C.J. 1971. Deposition and clearance of 2 μ particles in the tracheobronchial tree of normal subjects – smokers and nonsmokers. J. Clin. Inv., Vol. 50, pp. 1411-1420.

14. Brownian motion at liquid-gas interfaces. 1. Diffusion coefficients of macroparticles at pure interfaces. Radoev, B., Nedjalkov, M. and Djakovich, V. 1992, Langmuir, Vol. 8, pp. 2962-2965.

15. McKinley, G.H. Steady and transient motion of spherical particles in viscoelastic fluids. [book auth.] D. De Kee and R. Chhabra. Transport processes in bubbles, drops & particles, 2nd Ed. s.l. : Taylor & Francis, 2001, pp. 338-362.

16. Henje, K. 1994. The traction force in magnetic separators. Measurement Science and Technology, Vol. 5, pp. 1105-1108.

17. King, M. and Rubin, B.K. 2002. Pharmacological approaches to discovery and development of new mucolytic agents. Adv. Drug Deliv. Rev., Vol. 54, pp. 1475-1490.

18. Fuloria, M. and Rubin, B.K. 2000. Evaluating the efficacy of mucoactive aerosol therapy. Respiratory Care, Vol. 45, pp. 868-873.

19. King, M. 1998. Experimental models for studying mucociliary clearance. Eur. Respir. J., Vol. 11, pp. 222-228.

20. Rubin, B.K., Ramirez, O. and King, M. 1990. Mucus-depleted frog palate as a model for the study of mucociliary clearance. J. Appl. Physiol., Vol. 69, pp. 424-429.

21. Sudo, E., Boyd, W.A. and King, M. 2000. Effects of dextran sulfate on tracheal mucociliary velocity in dogs. J. Aerosol Med., Vol. 13, pp. 87-96.

22. Wang, Z.L., Lange, C.F. and Finlay, W.H. 2004. Use of an impinging jet for dispersion of dry powder inhalation aerosols. Int. J. Pharm., Vol. 275, pp. 123-131.

23. Voss, A. and Finlay, W.H. 2001. Deagglomeration of dry powder pharmaceutical aerosols. Int. J. Pharm., Vol. 248, pp. 39-50.

24. Silberberg, A. Rheology of mucus, mucociliary interaction and ciliary activity. [book auth.] C.J. Brokaw and P. Verdugo. Mechanism and Control of Ciliary Movement. New York, USA : Alan R. Liss, Inc., 1982.

Chapter 5: Magnetophoretic measurement of the drag force on partially immersed microparticles at air-liquid interfaces*

The flow around a moving sphere fully immersed in a fluid at low Reynolds numbers, i.e. Stokes flow, is one of the best-characterized in fluid mechanics. In the case of a sphere moving along the interface of two fluids, however, the problem becomes much more difficult since there is no analytical solution to the Stokes equation in this situation. The drag force on a particle moving along an interface cannot be calculated analytically for arbitrary contact angles (i.e. arbitrary positions across the interface; see Figure 5.1). Additional complications arise when surfactants are present at the interface. The excess of surfactant molecules will lead to surface viscosity at the interface, increasing the drag force [1]. The disturbance of the surface concentration of surfactant molecules by a moving particle at the interface will also cause a Marangoni force opposing the particle motion [2]. The Marangoni force is in turn counterbalanced by the transport of surfactant molecules from the high concentration region to the low concentration region in a bid to cancel out the disturbance caused by the particle motion. The complexity of these interactions between the moving particle, fluid, and surfactant transport are such that numerical or experimental methods are required to determine the drag force on particles moving along an interface.

---

*A version of this chapter has been accepted for publication. Ally, Amirfazli 2010. Colloids and Surfaces A.

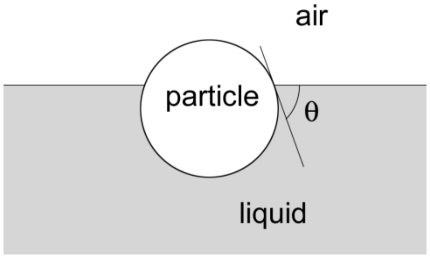

Figure 5.1: A solid, spherical microparticle at an air-liquid interface. The three-phase contact angle θ, which is measured through the liquid phase, determines the immersion depth of the particle in the liquid.

The motivating application for this study is to better understand the motion of magnetic particles in the human airway for the purpose of magnetic drug targeting [3-5]. For this application, the drag coefficient of particles moving along the airway surface has been shown to be of considerable importance [3, 6]. The drag force of the particles at the airway surface affects both the retention of individual particles as well as the formation of particle aggregates, which are more easily retained [6].

The motion of microscopic particles in a fluid is typically dominated by viscous forces, i.e. the Reynolds number is much less than 1, and the inertia of the particles can be neglected. In this case, the following well-known expression for the drag force can be derived analytically from the Stokes equation, $\nabla \boldsymbol{p} = \eta \nabla^{2} \vec{v}$, in which p is pressure and $\vec{v}$ is the fluid velocity:

$$\vec{\boldsymbol{F}}_{\boldsymbol{D}} = -6\pi\eta a\vec{U} \qquad (5.1)$$

In Equation (5.1), $\boldsymbol{a}$ is the particle radius, η is the bulk fluid viscosity, and $\vec{\boldsymbol{U}}$ is the particle velocity with respect to the fluid far from the particle.

If the particle is at an interface, i.e. is not fully immersed, as shown in Figure 5.1, there is no analytical solution to the Stokes equation that allows an expression for the drag force to be determined, for contact angles other than 0, 90, or 180° [7]. If surfactants are present, particles straddling an interface will also be subject to additional interfacial forces due to the surface tension gradient that occurs as the particle motion distorts the surrounding surfactant concentration. In some cases, the interfacial forces are dominant, and the protrusion of the particle into the subphase can be neglected. In [8], the motion of particles in biological membranes was studied by modeling the particles as discs in a viscous membrane of finite thickness over a subphase with a different viscosity. A similar, more detailed model was used in [9], which included the motion of the fluid in the subphase. These models neglect the part of the particle that is immersed in the liquid phase. The part of the particle in the liquid phase must be modeled as well, to predict drag forces accurately.

Danov *et al*. were the first to model a three-dimensional particle that protrudes into the subphase [10]. Danov *et al*. solved for the drag force in the case of pure liquids (i.e. nonviscous and incompressible interface), and for liquids with a surfactant or membrane layer using constant shear and dilatational viscosity terms to account for surface properties, and assuming the interface is compressible [10]. Results are given in [10] for particles with contact angles between 20° and 90°. In this model, the effect of the Marangoni force was neglected. An improved model was developed in [11], which includes the Marangoni effect and surfactant diffusion by using the Gibbs elasticity of the interface in their model. These calculations are only valid for small disturbances in the surfactant concentration, i.e. small Peclet numbers. Also, in [11], the bulk viscosity and bulk surfactant concentration are neglected.

Fischer *et al.* [12] used different approach from [10], solving for the forces on the immersed part of the particle and at the contact line separately for viscous interfaces, with the assumption that the interface is incompressible. The solution in [12] was for contact angles between 0° and 180°, as well as for immersed particles in the liquid near to the interface.

Previous works have focused on diffusion from the surface alone, e.g. [11], and may overestimate the effect of Marangoni forces by neglecting convective transport of the surfactant molecules. Convective transport would also introduce a velocity-dependent component of the resistance to particle motion, which has not been investigated in the literature.

Currently available solutions in the literature are not suitable for calculating drag forces on particles at the airway surface due to the complexity of the properties of airway mucus. The airway surface is lined with a layer of viscoelastic mucus with a surfactant layer on top of it. The mucus has a unique combination of properties that enables it to function as a part of the clearance mechanism for inhaled particles. Mucus is highly viscoelastic, with a low shear rate viscosity of approximately 1 Pa·s [13], and also has a low surface tension (~25 mN/m) due to a layer of surfactant at the surface [14]. This study attempts to address the lack of experimental results in the literature that are applicable to the airway. The liquids used in this study – water, silicone oil, and solutions of water and sodium dodecyl sulfate (SDS) – were chosen to reflect different aspects of mucus properties in isolation, in order to model the behavior of particles at the air-liquid interface in the airway on a basic level.

Various numerical models have been developed to predict the drag force on particles at fluid interfaces. These works have generally considered only ideal or simplified cases, either experimentally or theoretically [10, 15, 16] such as pure water, surfactant concentrations well above the CMC, and low particle velocities due to Brownian motion. These results cannot be generalized to apply to conditions at the airway surface which include the effects of surfactants below CMC, low particle contact angles, particle drag in bulk viscoelastic fluids, and higher particle velocities. This work investigates drag force on particles at an air-liquid interface moving along the interface experimentally.

5.1 Theoretical Background

5.1.1 Purely viscous drag

In most cases, for small particles, the particle will not distort the interface as the Bond number is small. The Bond number is given by:

$$Bo = \frac{\rho g a^2}{\gamma} \qquad (5.2)$$

where ρ is the particle density, g is the acceleration due to gravity, and γ is the surface tension or the air-liquid interface. In this work, the Bond number is on the order of 1×10^{-6} for the systems studied (see Section 5.2), so the interface around a particle is considered flat, i.e. the particle is displaced into the liquid phase to form the appropriate three phase contact angle. It is shown in [12] that if a contact line is formed, the particle will not be able to rotate. If the interface can be treated as flat, the particle immersion depth is a function of the particle three-phase contact angle, as shown in Figure 5.1. For such a case, Radoev *et al.* proposed the following expression for the drag force on a particle at an interface [7]:

$$\vec{\boldsymbol{F}}_{\boldsymbol{D}} = -6\pi\eta a\vec{U}y(\theta) \qquad (5.3)$$

in which the dependence on the contact angle is represented by the function $y(\theta)$. In the case of purely viscous resistance to particle motion, the drag coefficient of a particle at the interface will depend only on the extent of particle immersion.

Danov *et al.* solved the problem of the flow around a particle straddling an interface of a pure liquid numerically by formulating the problem in terms of the velocity and vorticity of the flow [10]. The drag coefficient was given in the form:

$$\vec{\boldsymbol{F}}_D = f\pi\eta a\vec{U} \qquad (5.4)$$

where the parameter *f* varies with the contact angle. Danov *et al.* found values of *f* for contact angles from 20 - 90°, obtaining values from approximately *f* = -4.2 for a contact angle of 20° to *f* = -3 for 90° [10]. The value for 90° corresponds to the particle being half-immersed (f = -3), and is half the drag force on a fully immersed particle (*f* = -6; see Equation (2.2)) [10]. Experimentally, the predicted values have been shown to be consistent for contact angles of 49, 53, and 82° in water (a low viscosity liquid) [15].

5.1.2 Surface viscosity

Interfaces with surfactants will have different properties from the bulk fluid due to the excess of molecules at the interface. This excess and the intermolecular interactions will cause molecules at the interface to have a shorter mean free path than molecules in the bulk fluid. As a result, the rate at which momentum is diffused through the interface will be faster, i.e. the viscosity of the interface will be greater than that in the bulk fluid. When surfactants are present, particles moving along the interface will experience additional drag force due to the surface viscosity, in addition to the drag force due to bulk viscosity. Surface viscosities may range from 10^{-8} to 10^{-5} kg/s [1]. A sample calculation in [1] shows that for a surface viscosity of 10^{-8} kg/s and assumed 1 nm interface thickness, the equivalent kinematic viscosity of the interface will be 100 kg/(m·s), 1000 times that of water. An interface with surfactants present may also be elastic, due to repulsion between like-charged heads or tails of the surfactant molecules. If the surfactant molecules are not in a condensed phase, the interface will be compressible. For a particle moving along an interface, surface viscosity and elasticity will provide additional resistance. These effects are captured in the surface dilatational and shear viscosities used in the models in [10, 12, 16]. The use of constant shear and dilatational viscosities for the surface may not accurately account for properties that are time or velocity dependent, however.

5.1.3 Marangoni resistance

Additional resistance to particle motion will also occur due to Marangoni forces. As a particle moves along an air-liquid interface with surfactants, the particle motion causes a region of high surfactant concentration in front of the particle (due to compression) and low concentration in its wake. This increases the surfactant concentration in front of the particle and decreases it in the wake, causing a region of low surface tension in front of the particle and high surface tension behind. The surface tension gradient causes a Marangoni force which opposes the particle motion. As the particle moves, convection and diffusion of the surfactant work to restore the uniform concentration. The extent of the Marangoni force opposing the particle motion depends on the surfactant concentration and the rate at which surfactant transport cancels out the surface tension gradient around the particle. Surfactant transport may occur: 1) along the interface, between the front of the particle (high concentration) to the particle wake (low concentration); 2) between the disturbed regions at the interface near the particle and the surrounding interfacial region; 3) between the disturbed region around the particle and the bulk liquid. Surfactant transport may occur by diffusion, due to the concentration gradient around the particle or due to convection as a result of the surface tension gradient and particle motion.

Dmitrov *et al.* [2] attempted to determine the effect of the Marangoni resistance from first principles, based on a perturbation analysis of the distortion of the surface concentration of surfactant by the particle motion. Surfactant transport by diffusion was considered in all three cases described above. In the analysis of [2] the surfactant resistance is related to the Marangoni number:

$$\boldsymbol{Ma} = \frac{\left(-\Gamma\,\partial\gamma/\partial\Gamma\right)\left(\partial\Gamma/\partial C\right)}{D\eta} \qquad (5.5)$$

where Γ is the surface concentration of the surfactant, *C* is the bulk surfactant concentration in the liquid, and *D* is the bulk diffusion coefficient of the surfactant. The Marangoni number reflects the relative strength of surface tension forces with respect to viscous forces. The relationships for the drag force derived in [2] are only valid for purely diffusive surfactant transport, i.e. small values of *Ma*. If *Ma*>1, the surfactant transport will be convection limited. For SDS in water, the analysis in [2] is only valid for concentrations <3 µM. This value is calculated using the Langmuir isotherm to estimate SDS surface concentration [17] and the data obtained in [18] for the variation in the surface tension of SDS solutions with concentration. This value indicates that for the SDS concentrations considered in this study (see Section 5.2.1), the surfactant transport is both by convection and diffusion, therefore experimental measurements of the drag force are required.

5.1.4 Drag force measurement

The drag force on particles moving along air-liquid interfaces was determined experimentally by trajectory analysis of particle motion in a known magnetic field (see next section). The magnetic force on a particle can be determined from the particle properties (magnetic susceptibility and size) and the magnetic field strength and gradient. The analysis is simplified by aligning the magnetic field with the interface so that the particle motion is entirely in the plane of the interface. By the Stokes approximation, the particle inertia is negligible, so the magnitude of the drag force will be equal to that of the magnetic force on the particle. The magnetic force $\vec{\boldsymbol{F}}_{\boldsymbol{M}}$ on a spherical particle is given by the following expression [19]:

$$\vec{\boldsymbol{F}}_{\boldsymbol{M}} = \frac{4}{3}\pi\mu_0 a^3 \chi \vec{H}\nabla\vec{H} \tag{5.6}$$

where μ_0 is the magnetic permeability of free space, χ is the particle magnetic susceptibility, and $\vec{H}$ is the magnetic field intensity. No demagnetizing factor is required in the above expression because, as described below, the effective magnetic susceptibility of the particles is measured experimentally and used to calculate magnetic force.

Using the Stokes approximation for particles in low-Reynolds number flows, the drag force can be equated to the magnetic force on the particle. The parameter *f* from Equation (5.4) can be determined from the particle velocity, given the particle trajectory and position relative to the magnetic field:

$$\vec{\boldsymbol{F}}_M = -\vec{\boldsymbol{F}}_D = -f\pi\eta a\vec{U} \tag{5.7}$$

$$-f\pi\eta a\vec{U} = \frac{4}{3}\pi\mu_0 a^3 \chi \vec{H}\nabla\vec{H} \tag{5.8}$$

$$f = -\frac{4\mu_0 a^2 \chi \vec{H}\nabla\vec{H}}{3\eta\vec{U}} \tag{5.9}$$

In the literature, the drag coefficient is expressed in terms of a drag force ratio β, i.e. the ratio of the parameter *f* for a partially immersed particle to the value of *f* = -6 for a fully immersed particle [10, 15]. As such, for the purposes of this study, β is given by the following expression:

$$\beta = \frac{2\mu_0 a^2 \chi \vec{H} \nabla \vec{H}}{9\eta \bar{U}} \qquad (5.10)$$

The viscous component of the drag force will also depend on the particle contact angle, which was also measured (see below) for comparison of the experimental results to those in [10].

5.2 Materials and Methods

5.2.1 Liquids used

The liquids used in the experiments were chosen to reflect various aspects of the mucus in the airways (in isolation). Measurements were performed using distilled, deionized water for comparison to existing data in the literature and confirmation of the experimental method. Aqueous solutions of the surfactant sodium dodecyl sulfate (SDS; 0.13 mM – 16.2 mM) were studied to better understand the effects of surfactants. SDS, a soluble, single-component surfactant was chosen because its adsorption behavior is well-characterized, which is necessary for these experiments given the limited data available in the literature on particle motion at interfaces. Although lung surfactant is an insoluble, multi-component surfactant, particle behavior at interfaces of SDS solutions serves as a first approximation particle behavior at the a-ir-liquid interfaces of the airways.

Silicone oils (500 cSt, 1000 cSt) were used to study the particle drag in a high-viscosity, low surface tension liquid, in the absence of surfactant effects. The viscosities of the silicone oils were measured by falling ball viscometry. The velocity of a 2 mm diameter silicon carbide ball falling due to gravity in each of the silicone oils was measured, and the viscosities were calculated using Equation (2.2), with the drag force being equal to the weight of each ball. The measured viscosity of the 500 cSt silicone oil was 0.40 ± 0.06 Pa·s; the measured viscosity of the 1000 cSt silicone oil was 0.82 ± 0.08 Pa·s.

5.2.2 Magnetic fields

The magnetic fields in the experiments were applied using a cylindrical neodymium-iron-boron (Nd-Fe-B) magnet, 6 mm in diameter and 25 mm long. The magnetic flux density along the center axis of the magnet was determined as a function of distance from the magnet pole face by measuring with a gaussmeter (FW Bell model 5020), and is shown in Figure 5.2. The flux density gradient was determined by interpolation of the measured flux density values. For the small observed regions in these experiments (<150 μm diameter field of view), the magnetic field and gradient were assumed to be uniform. The magnet field was varied by changing the distance between the magnet pole face and the field of view. The three distances used were 12, 10, and 6 mm; the field strengths and gradients for each are given in Table 5.1.

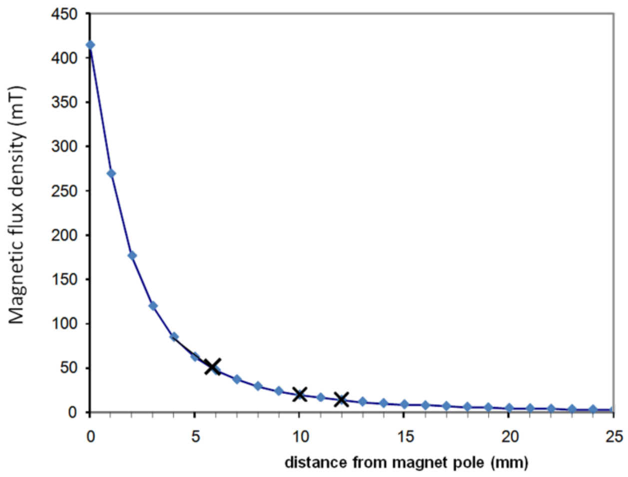

Figure 5.2: The magnetic flux density along the central axis of a 6 mm diameter, 25 mm long Nd-Fe-B magnet. The crosses on the graph at 6, 10, and 12 mm indicate the locations used in the experiments. The line is to guide the eye, the diamond symbols indicate measured data.

Table 5.1: Measured magnetic field strength and gradient at experiment locations

Distance from magnet (mm)	Flux density (mT)	Flux density gradient (T/m)
12	14	2.3
10	21	3.7
6	48	12.8

5.2.3 Particles

The particles used in the experiments were polystyrene particles that contain magnetite, making them magnetically susceptible. The particles are smooth surface polystyrene particles (PMS40) from Spherotech Inc., USA. The measured average diameter of particles was 4.8 ± 0.5 µm, based on the settling measurements described below and microscopic measurements from the image data collected (the error value is based on the standard deviation of the measurements). According to the manufacturer, the particles consist of a polystyrene core coated with a layer of magnetite nanoparticles, and then a layer of smooth polystyrene at the surface. As a result of this distribution of magnetic material, the particle magnetic susceptibility varies with size, as is likely with particles to be used in any application of magnetic targeting.

5.2.4 Magnetic susceptibility measurements

Since the magnetic susceptibility of the particles must be known to calculate the magnetic force, characterization of the particles was done by observing the trajectories of particles settling with a magnetic field applied perpendicular to gravity, as illustrated in Figure 5.3. This measurement was necessary as typical data available from particle manufacturers or in the literature pertains to the magnetization of bulk particle samples, not individual particles. Bulk values of magnetic susceptibility are influenced by the interaction of the magnetic fields of the particles comprising the sample, and will differ substantially from the values of individual particles.

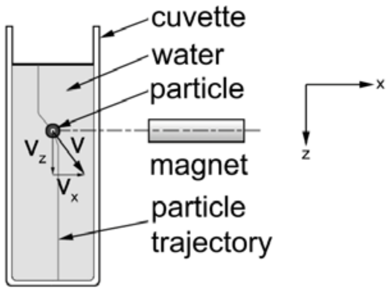

Figure 5.3: Schematic of the method used for determining particle magnetic susceptibility. The lens and camera used for observation of the particles are not shown.

For the magnetic susceptibility measurements, the particles were observed as they passed through an approximately 0.3 × 0.3 mm region, 12 mm from the magnet pole at its center, and aligned with the central axis of the magnet. The magnetic field and gradient in this region were assumed to be uniform, producing a horizontal force on the particles, perpendicular to the settling direction (hence the change in the particle trajectory; see Figure 5.3). Since the particles were fully immersed in the liquid (distilled, deionized water), the magnetic force and thus susceptibility can be determined from the observed trajectories. The particles were initially dispersed in the water before it was poured into the cuvette. The observed region was at the center of the cuvette, so the walls did not influence the particle motion. The particles were observed using a 10× microscope objective connected to a CCD camera with incident lighting. This was accomplished by initially focusing the camera on the magnet pole, and then moving the magnet using a micropositioner, such that the field of view was aligned to the center of the magnet (based on diameter) and then moving the magnet pole 12 mm away. The magnetic susceptibility is determined by equating the magnetic and drag forces (Equations (5.6) and (2.2)) in the horizontal (x) direction, giving the expression:

$$\chi = \frac{9\eta V_x}{2\mu_0 a^2 H_x \frac{\partial H_x}{\partial x}} \qquad (5.11)$$

where V_x is the horizontal component of the particle velocity and H_x is the horizontal component (i.e. only component along the central axis) of the magnetic field. The particle radius is determined similarly by equating the gravitational force on the particle to the vertical (z) component of the particle velocity:

$$a = \sqrt{\frac{9\eta V_z}{2\Delta\rho g}} \qquad (5.12)$$

where $\Delta\rho$ is the difference between the water and particle densities (to account for buoyancy), V_z is the vertical component of the particle velocity, and g is the acceleration due to gravity.

5.2.5 Experimental procedure

A schematic of the experimental apparatus is shown in Figure 5.4. Particle motion was observed at an inverted air-liquid interface through a 40× objective lens (Zeiss LD Plan-Neofluar, 0.6 numerical aperture) on a confocal inverted microscope (Zeiss Axiovert 200). The liquid samples were held above the objective lens from a silanized glass syringe cut midway along its barrel. For the experiments with SDS solutions, particles were added to the liquid prior to the liquid being held in the syringe, and then allowed to settle at the interface due to gravity. For the silicone oil samples, particles were placed at the interface using ~2 µL of ethanol as a carrier, and the ethanol allowed to evaporate. The typical separation distance between particles was initially ~10 particle diameters; as particles were depleted over the course of the experiments, this distance increased.

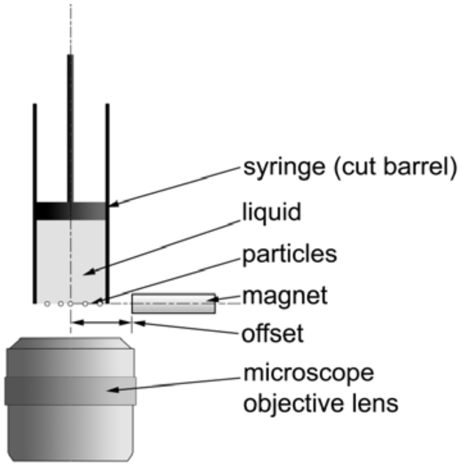

Figure 5.4: Schematic of the experimental apparatus used to observe particle trajectories.

Once the particles were at the interface, the magnetic field was applied by placing the permanent magnet in a fixture mounted to the objective lens. The fixture was mounted to the lens such that the center axis of the magnet was aligned with the objective field of view and focal plane, at distances 12 mm, 10 mm, or 6 mm from the magnet pole face to allow different amounts of magnetic force to be applied. The apparatus in Figure 5.4 was made entirely of non-magnetic material, and therefore did not distort that magnetic field. The objective lens contained a steel spring, but it was located near the base of the objective, however, and did not interfere with the magnetic field.

Images of the particles moving due to the magnetic field were captured using a CCD camera, and analyzed to determine the particle velocities. The images were captured at a known frequency (0.1 Hz for the water/SDS experiments, 0.03 Hz for the silicone experiments). Particles were tracked over several images to measure the displacements of their centers by pixel counting, and the velocity was determined by dividing by the elapsed time. Images were also captured before and after the magnet was inserted to ensure no other particle motion was present. Upon removal of the magnet, the particle motion stopped immediately.

In conducting such experiments, caution should be exercised as the most significant source of error in the particle trajectories is interaction between particles. The particles distort both the magnetic field and the liquid flow around them. The range of these distortions increase with particle size, which means the presence of large particle aggregates would cause more significant errors in the observed trajectories. Errors due to particle interactions were minimized by excluding particles closer than 10 particle diameters to any other particle; this reduces the error in particle velocity to less than 5% [20]. Also, particles with trajectories that deviated from the magnet axis were excluded. Deviation from the direction of the magnet axis would indicate some additional force acting on the particles, e.g. due to the motion of large particle aggregates outside of the observed field of view. These deviations disappear shortly after the initial application of the magnet, as large aggregates are pulled to the apparatus wall faster than individual particles due to the increased magnetic force they experience. Trajectory data was collected after the large aggregates had been cleared from the observed region. The initial particle density in the experiments was approximately 1 particle per 250 μm^2.

5.2.6 Particle contact angle measurements

To determine the viscous components of the drag coefficients of the particles, and to compare them to values found in the literature, the contact angles of the particles with the sample liquids in air must be determined; see Equation (5.3). This was done primarily using the film trapping method developed by Hadjiiski *et al.* [21]. Particles were observed sitting in a thin (< 3 μm) liquid film, such that interference fringes could be seen due to the liquid meniscus around the particle. A sample image showing the fringes around a particle in water is shown in Figure 5.5.

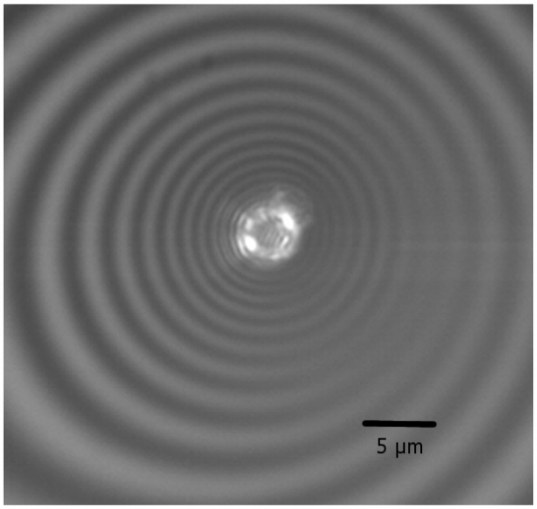

Figure 5.5: Interference fringes around a PMS40 polystyrene particle in a layer of water, used to calculated contact angle by the film trapping method.

As described in [21], the meniscus profile was determined from the spacing of the interference fringes. Based on this profile and the observed particle size, the contact angle was determined by fitting the Laplace equation, solved using the fourth order Runge-Kutta method, to the measured data points in order to determine the particle contact angle. The lateral resolution of the images for the objective lens and light source used was 0.3 μm. This corresponds to the error in the fringe and particle radii. By comparing curve fit solutions for the maximum positive and negative errors in particle radius and fringe position, a maximum error value of ±4° in the contact angle was determined.

These measurements were performed for the water/SDS solutions and the silicone oils. Contact angle measurements were also performed with silicone oil drops on a layer of spin-coated polystyrene using a CCD camera fitted with a 5× magnification lens. These measurements were performed due to uncertainty in using the film trapping method with extremely low contact angles.

5.3 Results and Discussion

5.3.1 Particle magnetic susceptibility measurement

The magnetic susceptibility of the particles was measured using the particle settling method described above. A linear relationship between the particle magnetic susceptibility and diameter was found, as shown in Figure 5.6. The linear relationship between the susceptibility and particle diameter reflects the distribution of magnetite in the particles in a layer or shell beneath the particle surface. The amount of magnetite is proportional to the square of the particle diameter (surface area) whereas the particle volume is proportional to the particle diameter cubed, leading to a linear relationship between the magnetic susceptibility and particle diameter. This data was used as a reference to determine the magnetic susceptibilities of observed particles based on their diameters.

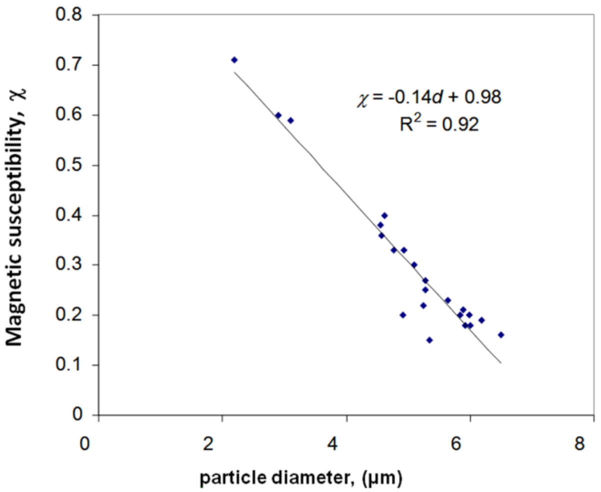

Figure 5.6: Plot of individual PMS40 particle magnetic susceptibility as a function of diameter

5.3.2 Water drag force ratios

The experiments with water served as a verification of the trajectory analysis method used in the experiments. The measured contact angle of the polystyrene particles and air/water interface was 63°. The average measured drag coefficient ratio was 0.62 ± 0.12 with the magnet at 12 mm, and 0.63 ± 0.03 with the magnet at 10 mm. Based on the Student's t-test, there was no statistical difference between the two sets of values. The measured drag coefficient ratio corresponds well to the value of 0.62 calculated in [10] for a liquid with zero surface viscosity. The ratio of the average velocity in the 10 mm case to that in the 12 mm case was 2.2, corresponding well to the ratio of 2.3 between the magnetic fields. This is expected for the purely viscous drag, since the particle velocities are directly proportional to the magnetic force. This agreement shows the validity of the method used in this study for measuring the drag coefficients.

5.3.3 Silicone oil drag force ratios

The contact angles of polystyrene and the silicone oils were measured using two different techniques: film trapping [21] and drop shape analysis. The measured values are given in Table 5.2. The film trapping method gave (immediate) contact angles of 12 ± 4° and 15 ± 4° for the 500 cSt and 1000 cSt samples, respectively. The contact angles of drops of silicone oils with a polystyrene film spin-coated on a glass coverslip were also measured by drop shape analysis. The initial/immediate contact angle was 10 ± 3° for the 500 cSt samples and 13 ± 3° for the 1000 cSt samples; after an hour, the drops completely wetted the polystyrene, i.e. the contact angle was 0°. This time-dependence occurs because, although the liquids completely wet the polystyrene, wetting is not immediate due to high viscosity of the silicone oils (500 cSt and 1000 cSt). Since the contact line of the particles is much smaller than that of the silicone oil droplets, and since they are freely displaced into the interface to form their three-phase contact angle, it can be assumed that they are completely wetted immediately. The difference in force ratios between 0° and 20°, encompassing the range seen in Table 5.2 is 4% [10, 20]; as such any resulting error from the assumption that the particles are completely wetted will be smaller than that of the drag coefficient measurement.

Table 5.2: Polystyrene particle/silicone oil contact angles

Method	**500 cSt silicone oil contact angle (°)**	**1000 cSt silicone oil contact angle (°)**
Film trapping	12 ± 4	15 ± 4
Drop shape analysis (immediate)	10 ± 3	13 ± 3
Drop shape analysis (after 1 hour)	0	0

The measured drag force ratio was 0.71 ± 0.1 for 500 cSt silicone oil and 0.75 ± 0.04 for 1000 cSt silicone oil. Since the silicone oils contain no surfactants, the drag on the particle is due solely to viscous forces. A t-test shows no statistically significant difference between the force ratios, which shows that the particle contact angles were similar for both liquids; this reflects the similar surface tension values of the liquids. For a fully immersed sphere in a given liquid, the value of β should be 1. As the particle moves further into the liquid phase away from the interface, the measured value of β should approach this value. Even if the particles are completely immersed in the liquid phase, i.e. 0° contact angle, the particles will remain just above the interface due to gravity, as shown schematically Figure 5.4 and observed in experiments. In the case of a sphere directly above the interface, the value of β should be less than 1, due to the boundary condition at the interface [20].

For particle contact angles between 0° and 20° there is no experimental data available in the literature. Drag coefficients for contact angles in this range are calculated in [12] but not in [10]. In [20], a β value of 0.72 for a contact angle of 0° is determined analytically. For a contact angle of 20°, [10] gives a β value of 0.75. In [12], the predicted β values for contact angles of 0 and 20° are 0.79 and 0.78, respectively, based on the given equations fitted to the numerical results. The measured values of 0.71 and 0.75 are consistent with the theoretical results for contact angles falling into this range.

Previous studies, e.g. [15], have only used water and surfactant solutions for verification of theoretical models of the drag on particles at interfaces [10, 12]. The results here show that the models can also be used to predict drag forces at much higher bulk viscosities, on the order of the viscosity of airway mucus. Also, since particles depositing in the airway are typically completely wetted by the mucus due to the surfactant layer [14], the accuracy of the theoretical results for contact angles less than 20° supports the use of these models for predicting the bulk viscosity component of particle drag in the airways.

5.3.4 SDS solutions

The contact angles for the particles with the SDS solutions are given in Table 5.3. The measured particle contact angles with the SDS solutions increased with the surfactant concentration. This is counterintuitive, as particle contact angles are typically expected to decrease with lowering of liquid interfacial tension. The reason for this may be that the particles are initially immersed and stored in the surfactant solutions. The surfactant may have adsorbed onto the particle surface, making it more hydrophobic, hence the observed increase in contact angle with surfactant concentration. A similar mechanism was used to hydrophobize particles in [15] with the surfactant cetyltrimethylammonium bromide (CTAB). One may think that the length of time the particles are stored in the surfactant solutions may affect the contact angle. However, any dependence of contact angle on the storage time of the samples would not affect the results of the experiments, as the contact angle and drag force measurements were performed concurrently using the same samples.

Table 5.3: SDS solution contact angles with polystyrene particles

SDS concentration (mM)	Contact angle (°)
0	63 ± 4
0.13	63 ± 4
0.25	63 ± 4
0.50	63 ± 4
1.0	62 ± 4
2.0	64 ± 4
4.0	86 ± 4
6.0	98 ± 4
8.0	106 ± 4
12	92 ± 4
16	95 ± 4

The particle contact angle affects the contribution of the bulk viscosity since it determines the immersed surface area of the particle. Based on the results in [10], the change in contact angle and corresponding change in viscous drag only accounts for, at most, 20% of the change in the force ratio over the range of contact angles in Table 5.3. As such, the differences seen in the force ratios at various SDS concentrations, plotted in Figure 5.7, are largely due to surface effects. As seen in Figure 5.7, the additional resistance is of the same order of magnitude as the viscous component of the drag force, which has a maximum possible value of β = 0.72 for a completely wetted particle, as discussed above.

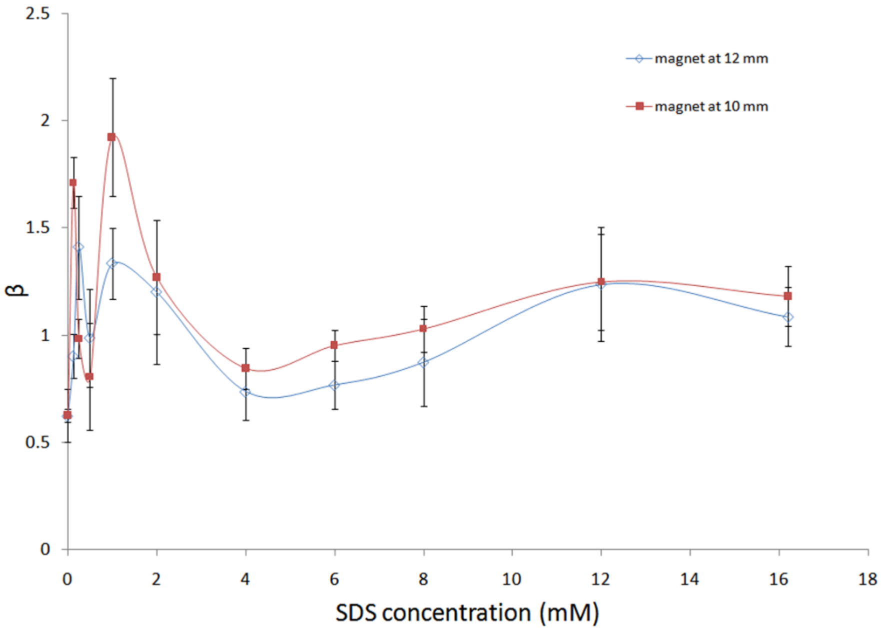

Figure 5.7: Drag force ratio as a function of SDS concentration for magnetic fields at the 12 mm (14 mT, 2.3 T/m) and 10 mm (21 mT, 3.7 T/m) positions.

The measured values of the force ratio β fluctuate with increasing SDS concentration. The fluctuations are not explained by statistical uncertainty, as t-tests between the results for concentrations from 0 – 4 mM show that the differences between values in this range are statistically significant when comparing pairs of data points. Considering the surface resistance in terms of distortion of surfactant concentration discussed above, at 0.13 mM, the difference in surfactant concentration across the particle should be higher than at 0.5 mM, as such the resistance force is larger. At 4 mM concentration, the difference in surfactant concentration is less than that in all other cases involving surfactant. The difference in surfactant concentration between the front and wake of a particle is related to the pressure distribution around the particle due to the particle motion, and the rate at which transport of the surfactant cancels out the concentration gradient. Convection of surfactant from the front to wake of the particle will also act against the concentration gradient. In cases where the surface resistance is low, i.e. at 4 mM, this may mean that the diffusion and convection processes act against the concentration gradient faster than in other cases. After 4 mM, the resistance rises with the surfactant concentration up to 12 mM, after which it levels off, as the force ratios at 12 mM and 16 mM are the same based on a Student’s t-test of the average values.

The CMC of SDS in water is 8.1 mM [18]; this value may be slightly lower in practice due to minute salt concentrations. Above the CMC of a surfactant solution, increase in the bulk concentration causes the formation of micelles; the number of free surfactant molecules at the interface, which causes the surface tension to change, i.e. the Marangoni effect, remains constant. Since there is no statistically significant difference in the drag force ratios above the CMC, the most significant surfactant transport must take place at the interface rather than to/from the bulk solution. If transport of the surfactant molecules to/from the bulk liquid were significant, there would be an observed difference in the drag force ratios above the CMC.

As discussed in Section 5.1.3, the magnitude of the Marangoni force depends on the difference in surfactant concentration between the regions in front of and behind the particle. To estimate the magnitude of the change in concentration, consider an order of magnitude analysis of the force required to produce the observed resistance to particle motion in the 2 mM case with the magnet at the 10 mm position. The 2 mM case is considered here instead of the 4 mM because it had the largest resistance and will provide an upper limit estimate of the concentration change. Similarly, in this analysis it is assumed that the additional drag force is entirely due to the Marangoni effect, also in order to provide an upper limit estimate of the concentration change. Based on data for the relationship between SDS concentration in water [18] and the Langmuir isotherm for SDS surface concentration [17], the derivative of surface tension with respect to surface concentration of SDS at a concentration of 2 mM is -755 Nm/mol. For simplicity, it is assumed that the reduced surface tension in front of the particle is the same on the entire front half of the contact line, and that the increased surface tension in the wake is uniform over the rear half of the contact line. The necessary surface tension difference across the particle required to produce the measured force ratio is 5.5×10^{-8} N/m. Dividing by the derivative of surface tension [18] with respect to surface concentration [17] at 2 mM gives a surface concentration difference of 7.3×10^{-11} mol/m^2 across the particle. Using the Langmuir isotherm to estimate the surface concentration of SDS in the 2 mM solution gives a value of 1.8×10^{-5} mol/m^2, six orders of magnitudes greater than the maximum surface concentration difference estimated above. This suggests that the interface should be treated as incompressible, as in [12].

Given the minute difference in surfactant concentration across a particle required to produce the observed resistance, it may be that minor surface-active impurities in the liquid phase may be responsible for the non-monotonic behavior of the drag force ratio with respect to surfactant concentration shown in Figure 5.7. Dodecanol in particular is the most significant impurity occurring in SDS solution even when all normal precautions in handling and storage of the surfactant and solutions are followed [22].

Dodecanol is a common agent in commercially available SDS, and also forms naturally over time due to hydrolysis of SDS in solution. Typically the amount of dodecanol in an SDS solution prepared without any special purification is on the order of 1% by weight of the amount of SDS (Ward et al. give a typical value of 10 μM dodecanol in 6 mM SDS [22]). Although the presence of dodecanol will lower the surface tension and CMC of SDS solutions [18, 23], the amount of dodecanol and resulting effects are often smaller than the experimental error values (<5%) and the effects are neglected. In the case of surface viscosity, however, the effects of dodecanol are much more significant due to its high surface activity. This is the case even for small quantities of dodecanol. Lu et al. showed, using neutron reflection studies, that the ratio of dodecanol to SDS at the interface of SDS solutions below CMC containing 0.5% by weight dodecanol was 1.4 [24]. For solutions of SDS between 0.5×10^{-4} M and 6×10^{-3} M concentrations, dodecanol increases the total amount of adsorbed material at the interface – both SDS and dodecanol [24]. This is because dodecanol, in addition to being adsorbed at the interface, also forms complexes with SDS molecules that are more easily adsorbed at the interface than individual SDS molecules [24]. This leads to an increase in the surface viscosity. Above the CMC, the effects of dodecanol are minimal, as the dodecanol molecules are incorporated into the SDS micelles [24]. This can also add to the reason for the uniformity of the results above CMC and their agreement with other results in the literature [15].

The non-monotonicity of the curves in Figure 5.7 may also be corroborated by the fact that the presence of dodecanol in SDS solutions has been shown to make the properties of the interface non-monotonic. The presence of a surface active contaminant will lower the surface tension of a liquid; in the case of dodecanol and SDS, the dodecanol also causes a minimum below the CMC [24]. The surface viscosity will also have a peak below the CMC [25]. The position of the surface tension minimum and surface viscosity peak will depend on the concentration of dodecanol; these two source of non-uniformity, resulting from the presence of dodecanol, can corroborate the behavior of the curves in Figure 5.7.

The drag force on the particles with the 10 mm magnetic field applied was consistently higher than with the 12 mm field applied, based on a t-test of the results. For each value of SDS concentration, the same sample was used for the 10 mm and 12 mm measurements, so the difference between the two measurements at each concentration cannot be the result of different amounts of dodecanol. This shows that the drag coefficient is velocity dependent. As such, timescale of surfactant transport is similar to that of particle motion. This result also shows that the use of constant surface viscosity terms as in [10] may not be appropriate in situations where particle velocity varies.

The velocity dependence in surface resistance, along with the persistent issues with the presence of dodecanol discussed above, may also explain the wide range in surface viscosity measurements of SDS solutions found in the literature [26]. In most of these measurements, the surface viscosity of SDS is calculated with the assumption that the surface viscosity is constant. Typically, velocity dependence and Marangoni effects are neglected, for example, in studies using Brownian motion to determine surface viscosity [16]. Dodecanol contamination may also be a common problem, as purification procedures used in the literature vary from minimal [15] to extensive [18]. The results here may have some relevance to the airway in that they show the sensitivity of surfactant-induced resistance to surfactant concentration and composition. The surfactant in the airways also has multiple components with varying surface activity [27]; variations in composition could produce differences similar to those between concentrations in Figure 5.7.

In terms of magnetic drug particle retention in the airways, the variation of surface resistance with velocity is particularly important as it would strongly affect the aggregation of particles at the interface. Magnetic particle aggregation occurs largely because of the local magnetic field gradients created near to magnetic particles as they distort the applied external field. As a result, the closer the particles are to one another, the greater the magnetic attraction between them, and faster they aggregate together. The speed of the particles increases as they approach one another. The size of the particle aggregates formed immediately after deposition in the airway has been shown to be a determining factor for particle retention [3]. As the particles move closer together, the magnetic attraction between them grows stronger, and the particle velocity increases. If the resistance to the particle motion also increases as they move closer to one another, this would limit the rate of particle aggregation. As such, smaller aggregates will form, requiring stronger magnetic fields to retain the particles at the airway surface.

Aside from the effect of surfactants on particle aggregation, the results also show that the surfactant can more than double the resistance to particle motion (e.g. at 2 mM concentration). The surfactant in the airway will greatly increase the resistance to particle motion relative to the mucus flow, increasing the magnetic force required to hold the particle in place. If multiple surfactants are present, as was the case with dodecanol and SDS, the resistance will not increase uniformly with surfactant concentration. This may also be true of surfactants in the airways, as lung surfactant has multiple components.

The results suggest that the Marangoni effect plays a significant role in the additional resistance particle motion along the interface. This would explain the dependence of the resistance on the particle speed, as well as fluctuations due to the presence of dodecanol in the SDS solutions. The importance of the Marangoni effect and the apparent incompressibility of the interface suggest that the physical basis of the theoretical model developed in [12] is more appropriate to the case of drag force with a surfactant layer considered here that of [10]. In the case of pure liquids, however, the experimental results were closer to those of [10], as are the analytical solutions for contact angles of 0, 90, and 180°.

5.4 Conclusions

The results of experiments show that for air-liquid interface without surfactants present, the existing theoretical models [10, 12] accurately predict the drag force on particles moving along the interface. This was demonstrated using water, which also confirmed the applicability of the method used by agreement with other results in the literature. The results of the experiments with silicone oil showed that the theoretical results in [10] can be extrapolated to contact angles of less than 20°, and that [10] and [12] are valid for a wide range of viscosities, allowing the bulk viscosity component of the drag on a particle at the air/liquid interface of the airways to be predicted.

The experiments with SDS showed that surfactants greatly increase the resistance to particle motion of the interface. This is likely due to the Marangoni force caused as the particle distorts the surface concentration. The resistance was found to increase non-uniformly with surfactant concentration, which may be explained by the presence of dodecanol in the surfactant solutions. The surface resistance was also found to be dependent on particle velocity. From an applied perspective, this would limit the size of aggregates formed by magnetic particles in the airways, increasing the magnetic field required to retain the particles at the target site.

5.5 References

1. Hiemenz, P.C. and Rajagopalan, R. Principles of Colloid and Surface Chemistry, 3rd Ed. USA: Marcel Dekker Inc., 1997.

2. Dimitrov, K., Avramov, M. and Radoev, B., 1994. Brownian motion at liquid-gas interfaces, 3. Effect of insoluble surfactants. Langmuir, Vol. 10, pp. 1596-1599.

3. Ally, J., Amirfazli, A. and Roa, W. 2006. Factors affecting magnetic retention of particles in the upper airways: an in vitro and ex vivo study. J. Aerosol Med., Vol. 19, pp. 491-509.

4. Amirfazli, A. 2007. Magnetic nanoparticles hit the target. Nat. Nanotechnol., Vol. 2, pp. 467-468.

5. Dames, P., et al. 2007. Targeted delivery of magnetic aerosol droplets to the lung. Nat. Nanotechnol., Vol. 2, pp. 495-499.

6. Ally, J., Roa, W. and Amirfazli, A. 2008. Use of mucolytics to enhance magnetic particle retention at a model airway surface. J. Magn. Magn. Mater., Vol. 320, pp. 1834-1843.

7. Radoev, B., Nedjalkov, M. and Djakovich, V., 1992. Brownian motion at liquid-gas interfaces. 1. Diffusion coefficients of macroparticles at pure interfaces. Langmuir, Vol. 8, pp. 2962-2965.

8. Saffman, P.G. and Delbruck M., 1975. Brownian motion in biological membranes. Proc. Natl. Acad. Sci., Vol. 72, pp. 3111-3113.

9. Stone, H.A. and Ajdari, A., 1998. Hydrodynamics of particles embedded in a flat surfactant layer overlying a subphase of finite depth. J. Fluid Mech., Vol. 369, pp. 151-173.

10. Danov, K., *et al*. 1995. Influence of the surface viscosity on the hydrodynamic resistance and surface diffusivity of a large Brownian particle. Journal Colloid Interface Sci., Vol. 175, pp. 36-45.

11. Dimova, R., *et al.* 2000. Drag of a solid particle trapped in a thin film or at an interface: influence of surface viscosity and elasticity. Journal Colloid Interface Sci., Vol. 226, pp. 35-43.

12. Fischer, T.M., Dhar, P. and Heinig, P. 2006. The viscous drag of spheres and filaments moving in membranes or monolayers. J. Fluid Mech., Vol. 558, pp. 451-475.

13. King, M., Brock, G. and Lundell, C. 1985. Clearance of mucus by simulated cough. J. Appl. Physiol., Vol. 58, pp. 1776-1782.

14. Schürch, S., et al. 1999. Particles at the airway interfaces of the lung. Colloid Surface B, Vol. 15, pp. 339-353.

15. Petkov, J.T., Danov, K.D. and Denkov N.D. 1996. Precise method of measuring the shear surface viscosity of surfactant monolayers. Langmuir, Vol. 12, pp. 2650-2653.

16. Sickert M., Rondelez, F. and Stone, H.A. 2007. Single-particle Brownian dynamics for characterizing the rheology of fluid Langmuir monolayers. Europhys. Lett., Vol. 79, pp. 66005-p1-p6.

17. Chang, C-H. and Franses, E.I. 1995. Adsorption dynamics of surfactants at the air/water interface: a critical review of mathematical models, data, and mechanisms. Colloid Surface A, Vol. 100, pp. 1-45.

18. Mysels, K.J. 1986, Surface tension of solutions of pure sodium dodecyl sulfate. Langmuir, Vol. 2, pp. 423-428.

19. Henje, K. 1994. The traction force in magnetic separators. Meas. Sci. Technol., Vol. 5, pp. 1105-1108.

20. Happel, J. and Brenner, H. Low Reynolds number hydrodynamics: with special applications to particulate media, 2nd Ed. The Hague: Martinus Nijhoff Publishers, 1973.

21. Hadjiiski, A. *et al*. 1996. Film trapping technique: precise method for three-phase contact angle determination of solid and fluid particles of micrometer size, Langmuir, Vol. 12, pp. 6665-6675.

22. Ward, R.N., Davies P.B. and Bain, C.D. 1997. Coadsorption of sodium dodecyl sulfateand dodecanol at a hydrophobic surface. J. Phys. Chem. B, Vol. 101, pp. 1594-1601.

23. Lu, J.R., Thomas, R.K. and Penfold, J. 2000. Surfactant layers at the air water interface: structure and composition. Adv. Colloid Interfac., Vol. 84, pp. 143-304.

24. Lu, J.R. *et al.* 1995. The composition and structure of sodium dodecyl sulfate-dodecanol mixtures adsorbed at the air-water interface: a neutron reflection study. Journal Colloid Interface Sci., Vol. 174, pp. 441-455.

25. Karakashev, S.I. and Nguyen, A.V. 2007. Effect of sodium dodecyl sulphate and dodecanol mixtures on foam film drainage: Examining influence of surface rheology and intermolecular forces. Colloids Surface A, Vol. 293, pp. 229-240.

26. Stevenson P. 2005. Remarks on the shear viscosity of surfaces stabilised with soluble surfactants. Journal Colloid Interface Sci., Vol. 290, pp. 603-606.

27. Schürch, S., Lee, M. and Gehr, P. 1992. Pulmonary surfactant: surface properties and function of alveolar and airway surfactant. Pure Appl. Chem., Vol. 64, pp. 1745-1750.

Chapter 6: Microsphere tensiometry to measure the force required to penetrate air-liquid interfaces*

6.1 Introduction

The purpose of the experiments in this chapter is to measure the force required to detach microparticles from the interfaces of air and various liquids, i.e. the adhesion force of microparticles to air-liquid interfaces. This type of interaction between particles and interfaces is important in froth flotation processes, which are extensively used in the mining industry [1]. As such, previous studies have focused on water and surfactants used in mineral processing [1, 2]. In this chapter, however, the motivating application is the use of magnetic fields to target and retain drug particles in the human airway [3]. Liquid properties and interface configurations are chosen to reflect this application.

Magnetic targeting is a potentially beneficial approach for enhancing drug delivery to the airways of the lung [4]. Due to the mucus clearance mechanism in the airways that removes inhaled particulate matter, particle retention at target sites in the airways is necessary for effective drug delivery [5]. One strategy that has been suggested to retain particles is to use magnetic fields to pull particles deposited at the target site through the mucus layer lining the airway into the tissue beneath [3]. To do this, the particles must be pulled from the interface of the mucus layer lining the airways by an applied magnetic field.

The human airway is lined with a layer of mucus, typically 5-10 μm thick [6], that is constantly being moved toward the oropharynx in order to remove

---

* A version of this chapter has been submitted for publication. Ally, Vittorias, Amirfazli, Kappl, Bonaccurso, McNamee, Butt 2009. Langmuir.

inhaled particles. As described in [6], the mucus sits atop a layer of ciliated epithelium; the beating of the cilia in the watery, periciliary liquid between the mucus and cell lining propels the mucus layer.

Airway mucus consists of a thick, viscoelastic gel with a layer of surfactant at its surface [7]. The thickness of the mucus layer in the trachea is typically ~10 μm. This is similar to the optimal diameter of inhaled drug particles for deposition in the airways. Particles depositing in the airway will initially be pinned at the interface of the mucus layer.

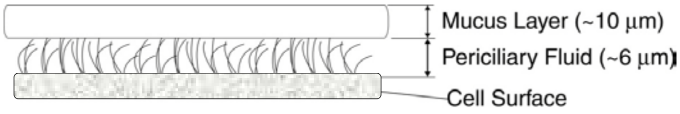

Figure 6.1: Schematic of the airway surface lining in the trachea.

The force required to remove particles from air-liquid interfaces was investigated in [8] for interfaces of bubbles and drops by Scheludko *et al*. It was assumed that only the capillary force, i.e. surface tension, must be overcome to detach a particle from an interface. In [8] the maximum adhesion force of a particle to an interface is predicted theoretically from the surface tension and geometry of the interface. Surface tension was determined experimentally by measuring the adhesion force between the particle and interface by tensiometry; the interface geometry was measured optically. The particles used in [8] were 2 mm diameter glass spheres from the melted end of a 0.3 mm diameter glass fiber; the glass was hydrophilic with a contact angle (CA) of ~7° with water, which was the only liquid used. Scheludko *et al*. were unable to measure the influence of CA hysteresis as the electric balance used was not sufficiently sensitive [8].

Pitois and Chateau [2] used a similar approach to [8] for calculating and measuring the work of detachment of similarly sized particles (0.15 – 0.5 mm diameter) from air-water interfaces. Although the theoretical development in [2] included buoyancy and gravitational forces, these were not considered as they are insignificant for particles <100 µm in diameter. Pitois and Chateau [2] were able to measure the contact angle hysteresis, and incorporated it into their predictions of the work of detachment by using the receding contact angle in their calculations, leading to good agreement with their experimental results. The work of detachment was determined in [2] by integrating the force-distance curve of the particle motion, i.e. the force on the particle and the distance of the particle from its equilibrium position at the interface. It was found that, when the contact line was pinned, the force-distance relationship was linear.

The force on a spherical particle due to the surface tension of an axisymmetric interface is given by the expression [8]:

$$P = 2\pi\gamma R_0 cos\psi_0 \quad (6.1)$$

where γ is the surface tension of the interface, R_0 is the radius of the contact line, and ψ_0 is the value at the contact line of the angle ψ between the interface and center axis of the particle (see Figure 6.2). The maximum force P_m as a particle of radius R is detached from the interface of a bubble is shown in [8] to be:

$$P_m = 2\pi\gamma R \cos^2(\theta/2) \quad (6.2)$$

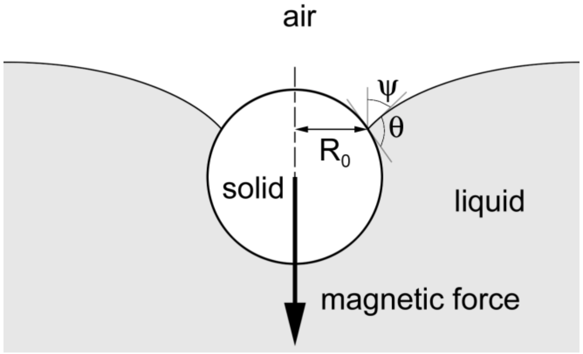

Figure 6.2: A particle being pulled into a liquid interface by a magnetic force

Atomic force microscopy (AFM) has been used extensively to study the interaction of particles (also called colloidal probes) and interfaces. Preuss and Butt measured the contact angles of microparticles with the air-liquid interface of 0.5 mM KCl using the colloidal probe technique [9]. In [9], solid particles were attached to AFM cantilevers. The AFM was used to bring the particle into contact with the interface of an air bubble to measure the force on the particle. Similar experiments can also be performed with liquid drops [10]. Particle contact angles and detachment forces are determined from the resulting force-distance curves. This method of using solid particles attached to cantilevers has become a popular method of studying particle behavior at interfaces, although most previous studies have only measured the particle contact angle.

Previous studies of the interaction of solid particles and air-liquid interfaces have used the interfaces of air bubbles or liquid drops much larger than the particle diameter. In such cases, the particles used are typically sufficiently small that the capillary force on the particle is stronger than the gravitational force, and the particle can be freely displaced into the interface to take an equilibrium position without formation of a notable meniscus.

In a liquid film such as the mucus layer, if the particle size is similar to or greater than the film thickness, there will be a meniscus of notable curvature formed around the particle. Formation of a curved meniscus around a particle will result in a pressure difference across the air-liquid interface, as predicted by the Laplace equation:

$$\Delta P = \gamma \left(\frac{1}{R_1} + \frac{1}{R_2} \right) \quad (6.3)$$

In Equation (6.3) above, ΔP is the pressure difference across the interface, R_1 and R_2 are its principal radii of curvature of the meniscus. If the particle is pulled into the interface, e.g. by a magnetic force, this would result in additional changes to the meniscus curvature and thus the pressure across the interface according to Equation (6.3).

For microparticles, the particle contact angle can be affected by line tension [11]. As such, contact angle measurements made using other systems, e.g. a sessile drop on a planar substrate, may not necessarily be relevant. Neither [2] nor [8] have considered line tension in their derivation of Equation (6.1). For simplicity, line tension is also not considered in the present analysis.

In addition to the Laplace pressure, when a particle is pushed into or pulled out of a liquid film, there may also be additional hydrodynamic resistance due to restricted flow of liquid, i.e. restricted film drainage, within the film layer due to the constrained geometry (limited amount of liquid present), and in the case of the airways, viscoelasticity of the mucus. These hydrodynamic effects have not been measured in previous studies as they are not significant in the air bubble or liquid drop interface configurations due to the unconstrained liquid phase (large liquid volume relative to particle size) and low-viscosity liquids used. In the present experiments, various liquids were used to study the effects of different mucus properties independently.

To study the effects of Laplace pressure and film hydrodynamics, the force on a particle as it was pulled from a liquid film was measured using atomic force microscopy. The configuration of a thin liquid film on a rigid substrate (Figure 6.3(a)) was selected for experimental and practical reasons. Realistic modeling of more complicated features of the airway surface such as the dual (mucus and periciliary) layers or compliant cell lining was not attempted as this would make interpretation of the results difficult, since this type of system is not investigated hitherto and a basic understanding is needed first. Experiments were also performed using the air-liquid interfaces of air bubbles for comparison. The bubble configuration represents the case of a completely compliant cell lining, in which the particle can be freely displaced into the liquid. A schematic of the bubble configuration is shown in Figure 6.3(b).

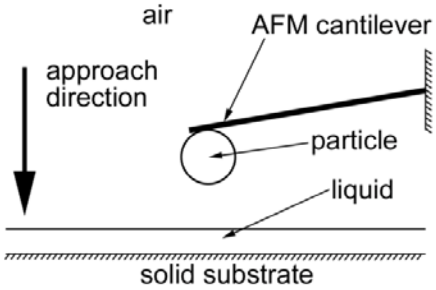

(a)

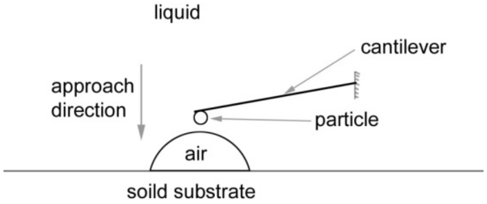

(b)

Figure 6.3: Schematic of the (a) liquid film and (b) bubble configurations used in these experiments

In the liquid film configuration selected for the experiments, the detachment force is measured as the particles are pulled from the interface into the air phase, in contrast to the proposed application of pulling particles from the interface into the liquid phase. For the simplified film configuration used here, pulling the particle into the air phase will still result in similar formation of a meniscus and corresponding film drainage as pulling it into the liquid phase, but the film drainage will be in the opposite direction, i.e. the liquid will flow toward the particle instead of away. As pulling the particle out of the film is easily accomplished in practice and hydrodynamic effects have not been studied before, this approach is sufficient to provide an order-of-magnitude understanding of the effect of hydrodynamic and meniscus formation on the force required to remove a particle from an interface. To provide more insight into hydrodynamic effects, measurements were performed with different cantilever speeds to study the effect of particle retraction speed. In the bubble experiments, the detachment force was measured similarly, as particles are detached from the interface into the liquid layer. In this respect (detachment from the interface into the liquid phase), the bubble configuration is closer to the proposed application, but would not capture any hydrodynamic effects that occur due to the constrained film configuration. By comparing measurements of interfaces in these two interface configurations, the extent of the hydrodynamic effects can be determined.

6.2 Materials and Methods

An atomic force microscope (AFM; JPK NanoWizard) was used to measure the force on particles (attached to the end of a tipless AFM cantilever) as they were brought into contact with and detached from the air-liquid interfaces. The AFM module is mounted on an inverted optical microscope (Zeiss Axiovert 200), which allows visual observation of the sample and cantilever. When using an AFM, the deflection of a microscopic cantilever is measured using an optical lever system to amplify the cantilever deflection and convert it to a voltage signal using a photodetector. The voltage signal is converted into deflection values using the system sensitivity, which is determined by pressing the cantilever against a rigid surface. The deflection of the cantilever can be converted to a force value using the spring constant of the cantilever, giving a force-position curve as the particle is moved into and out of an interface. Cantilever sensitivity and spring constant measurements were performed after each set of interface measurements using the thermal fluctuation method. These measurements are summarized in Table 6.1; in some cases, repeatable stiffness values were not obtained and the manufacturer's specified nominal value was used instead.

Table 6.1: Cantilever sensitivity and stiffness; italicized text indicates nominal values were used.

liquid	**configuration**	**run #**	**sensitivity (nm/V)**	**stiffness (N/m)**
water	film	1	32.89	5.71
water	film	2	32.89	5.71
10 000 cSt silicone	film	1	-	3.78
10 000 cSt silicone	film	2	64.70	1.55
10 000 cSt silicone	film	3	46.50	4.83
10 cSt silicone	***film***	***1***	***43.38***	***4.50***
10 cSt silicone	film	2	39.06	3.95
10 cSt silicone	***film***	***3***	***43.38***	***4.50***
5 cSt silicone	film	1	46.50	4.83
5 cSt silicone	film	2	66.96	1.15
5 cSt silicone	film	3	59.20	1.06
water	***bubble***	***1***	***31.71***	***4.50***
water	bubble	3	33.26	4.43
water	bubble	4	38.24	4.99
1 mM SDS	bubble	1	31.80	3.68
1 mM SDS	bubble	2	34.12	3.50
1 mM SDS	bubble	3	33.32	4.47
1 mM SDS	bubble	4	32.75	6.19
2 mM SDS	bubble	1	34.72	2.56
2 mM SDS	bubble	2	37.58	4.90
2 mM SDS	***bubble***	***3***	***45.19***	***4.50***
4 mM SDS	***bubble***	***1***	***21.34***	***4.50***
4 mM SDS	bubble	2	34.72	2.56
4 mM SDS	bubble	3	37.50	3.74
mucus simulant	thick film	1	43.38	1.63
mucus simulant	thick film	2	42.75	1.12

Colloidal probes were fabricated by sintering polystyrene particles (PMS40, Spherotech Inc.) onto the surface of silicon cantilevers (Mikromasch UltraSharp NSC12). The procedure was as follows: particles were picked up from a glass slide using a micromanipulator with a cantilever attached, under a microscope with a 40× objective lens. This also allowed the particle diameters to be measured; only particles with diameters of 5.0 ± 0.5 μm were selected. The particles were then placed on the tip of another cantilever to which they were attached by sintering at 120°C for 30 minutes on a hot plate. Scanning electron microscope images of a sample cantilever are shown in Figure 6.4.

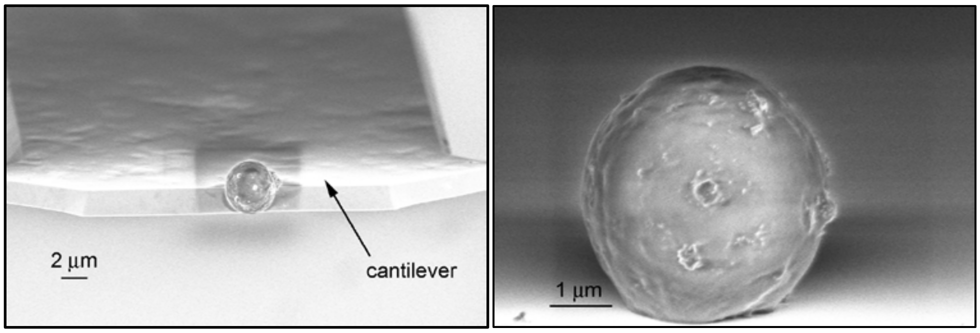

(a) (b)

Figure 6.4: (a) A colloidal probe with a sintered particle (front view), and (b) detail view of the particle (front view).

For the film experiments, the cantilevers were silanized prior to attaching the particle. This was done to prevent wetting of the cantilever by the liquid, which would break the cantilever off due to the large capillary force. The cantilevers were cleaned in an argon plasma for 10 minutes, and then silanized by exposure to fluorosilane vapor (trichloro(1H,1H,2H,2H-perfluorooctyl)silane, Sigma Aldrich) for 4 hours. The cantilevers were then kept under vacuum for 1 hour to remove any excess fluorosilane. Stability of the silane layer during sintering was not a concern. The cantilevers remained sufficiently hydrophobic after the particles were attached, as no wetting of the cantilever was observed.

In order to study the different properties of the mucus lining the airways in isolation, various liquids were used in the experiments. Water (from a Milli-Q water purification system, 18.2 MΩ resistivity) was used to provide a baseline measurement in both the film and bubble experiments. In the film experiments, silicone oils (Sigma Aldrich) were used to study the effect of increased viscosity. The silicone oil kinematic viscosities were 5, 10 and 10 000 cSt according to the manufacturer's specifications. The 5 and 10 cSt silicone oils had viscosity of similar order of magnitude to water, but low surface tension (20 mN/m), similar to the mucus layer. The viscosity of the 10 000 cSt silicone oil was similar to the apparent low shear rate viscosity of mucus, as was the low surface tension (22 mN/m). A locust bean gum (LBG)-based mucus simulant [12] was also tested to study the effect of viscoelasticity of the liquid phase. The mucus simulant consisted of a 5% locust bean gum crosslinked with 1.5% sodium tetraborate, as described in [12]. In the bubble experiments, water-SDS solutions were used (pure water, 1, 2, and 4 mM concentrations) to study interfaces with reduced surface tension. The SDS was purified by recrystallization from ethanol, and all of the glassware used in the experiments was cleaned using the RCA procedure. The silicone oils could not be used for the bubble experiments due to the potential to contaminate the AFM sample holder, and because it is impractical to immerse the sample holder in the liquid without forming air bubbles on the cantilever. The same concerns applied in the case of the locust bean gum.

Liquid films of water and silicone oil, 0.3 – 1.4 μm thick, were produced by placing a ~2 μL drop of liquid on a plasma-cleaned glass slide and allowing it to spread. Measurements were performed ~2 mm from the edge of the film formed as a result of spreading. The mucus simulant was not amenable to forming a film; in this case a 1 mm thick slice of the gel, cut with a scalpel, was used instead. In the bubble experiments, air bubbles (approximately 0.25 mm contact line diameter) were formed on the bottom of liquid-filled polystyrene petri dishes using a syringe and stainless steel needle.

The liquid samples (films and bubbles) were placed on the sample holder of the AFM, and the cantilevers mounted on the piezoelectric actuator. The piezoelectric actuator was used to extend and retract the cantilever at various speeds such that the particles on the cantilevers were brought into contact with the film and glass slide and then pulled away. The AFM was operated in closed-loop mode, in which feedback control of the piezoelectric actuator position via a strain gauge used for extension/retraction. Multiple force curves were measured for each sample and speed.

6.3 Results and Discussion

6.3.1 Force curves

Representative force curves from the liquid film interface measurements are shown in Figure 6.5 – Figure 6.9. Twenty measurements were performed in each case; for clarity, only the initial (light colored) and final (dark colored) force curves are shown, since changes over the course of the measurements were uniform. Force curves from the bubble interface measurements are shown in Figures 6.10 – 6.19. In this case, multiple measurements at various speeds showed little variation; as such, only single representative curves are shown. This can be seen by comparing the normalized adhesion forces measured in the bubble experiments at various speeds. As shown in Figure 6.14, there is less than 8% variation over scan speeds from 0.7 – 55 μm/s, and there is no trend, i.e. increase or decrease of adhesion force between the particle and bubble interface, corresponding to the cantilever speed.

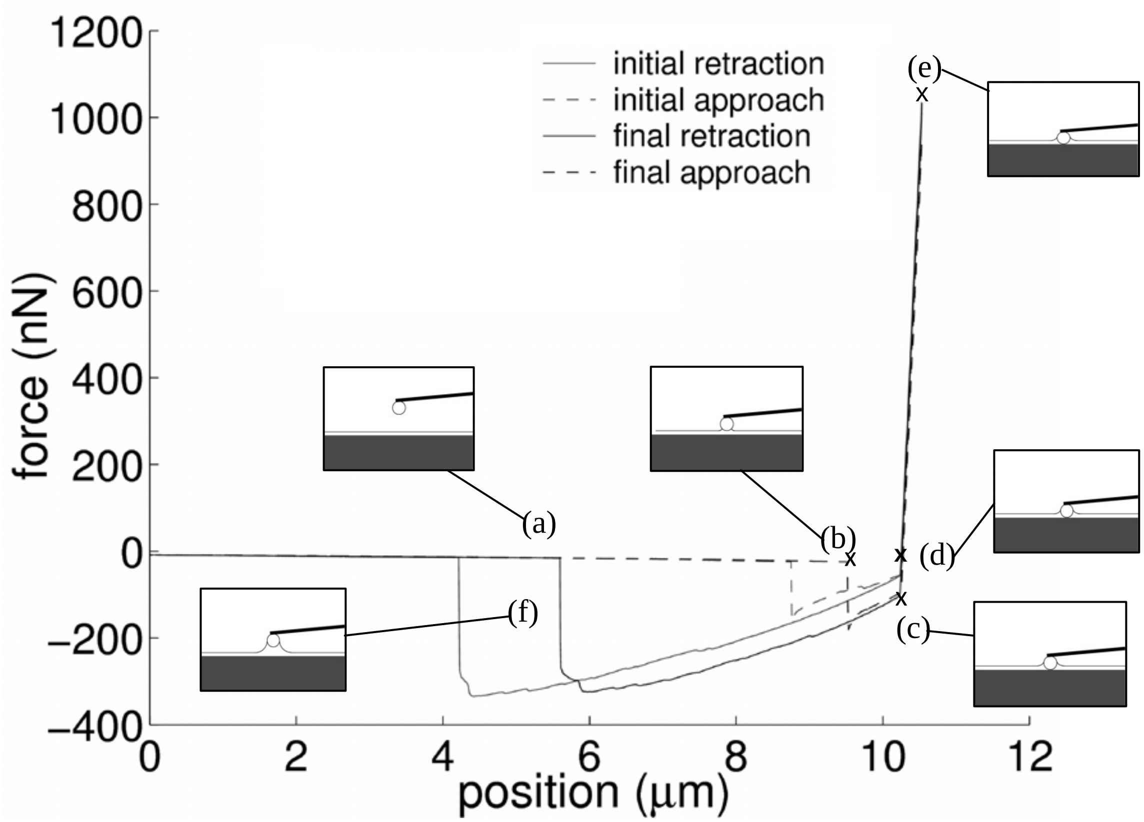

Figure 6.5: A sample force curve generated from a measurement with a water film at an extension/retraction speed of 21 µm/s. Initial film thickness was 1.5 µm. The inset figures show the shape of the interface as the solid particle is brought into contact and then pulled away from the air-liquid interface of a liquid film.

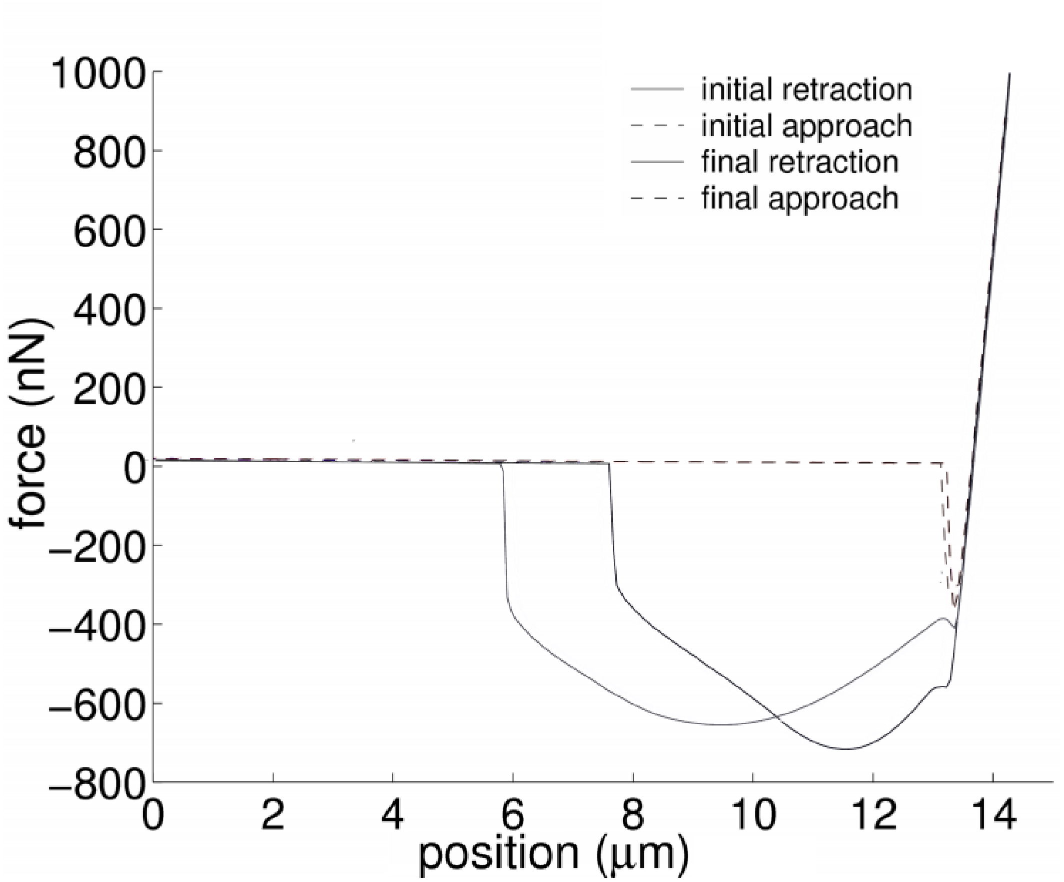

Figure 6.6: Initial and final force curves for a water film, 142 μm/s extension/retraction speed. Initial film thickness was 0.4 μm.

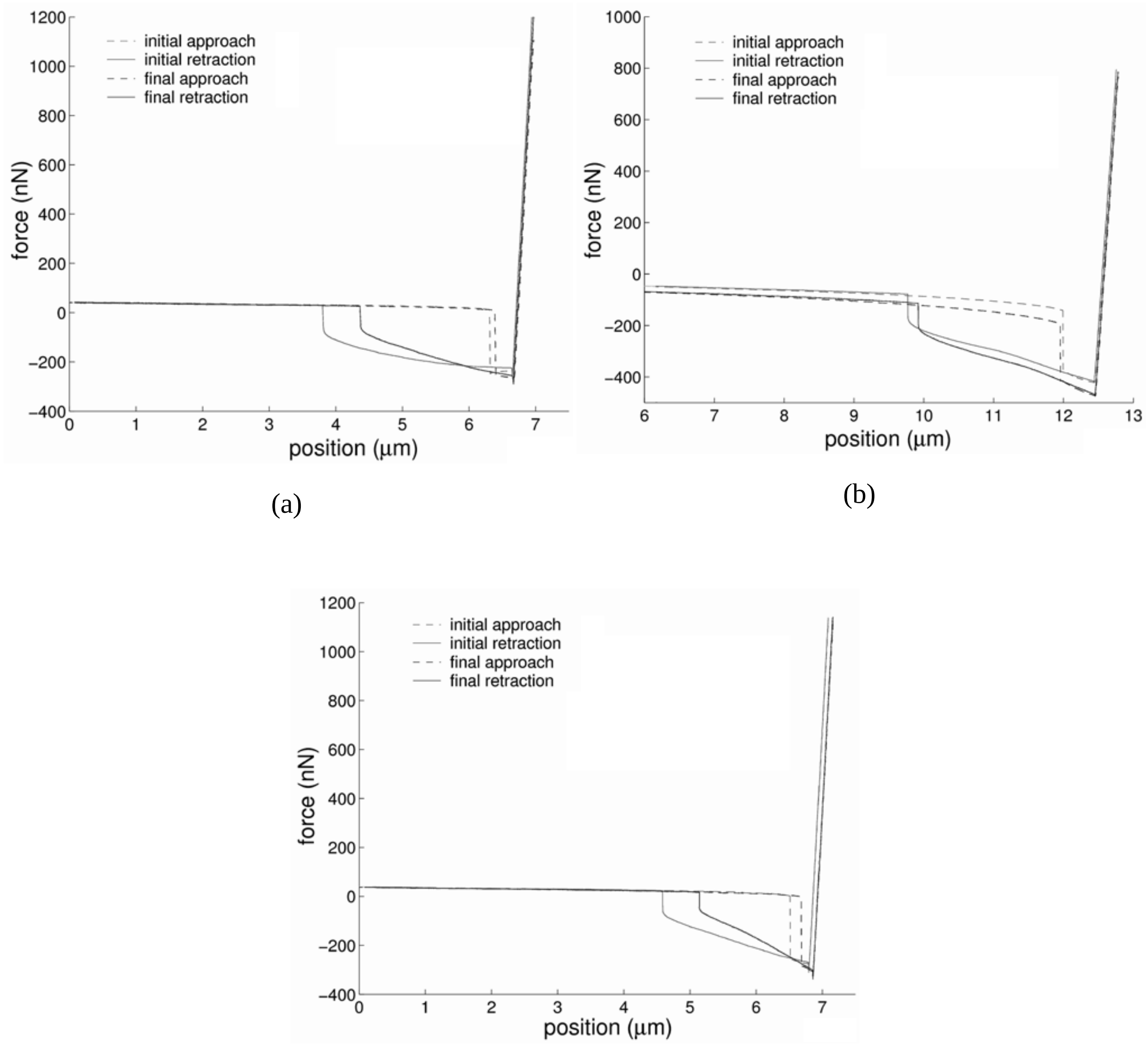

(a)

(b)

(c)

Figure 6.7: Force curve for 5 cSt silicone oil film, with extension/retraction speed of (a) 14 μm/s, (b) 3.6 μm/s, (c) 0.7 μm/s; the initial film thickness was 0.4 μm in all cases.

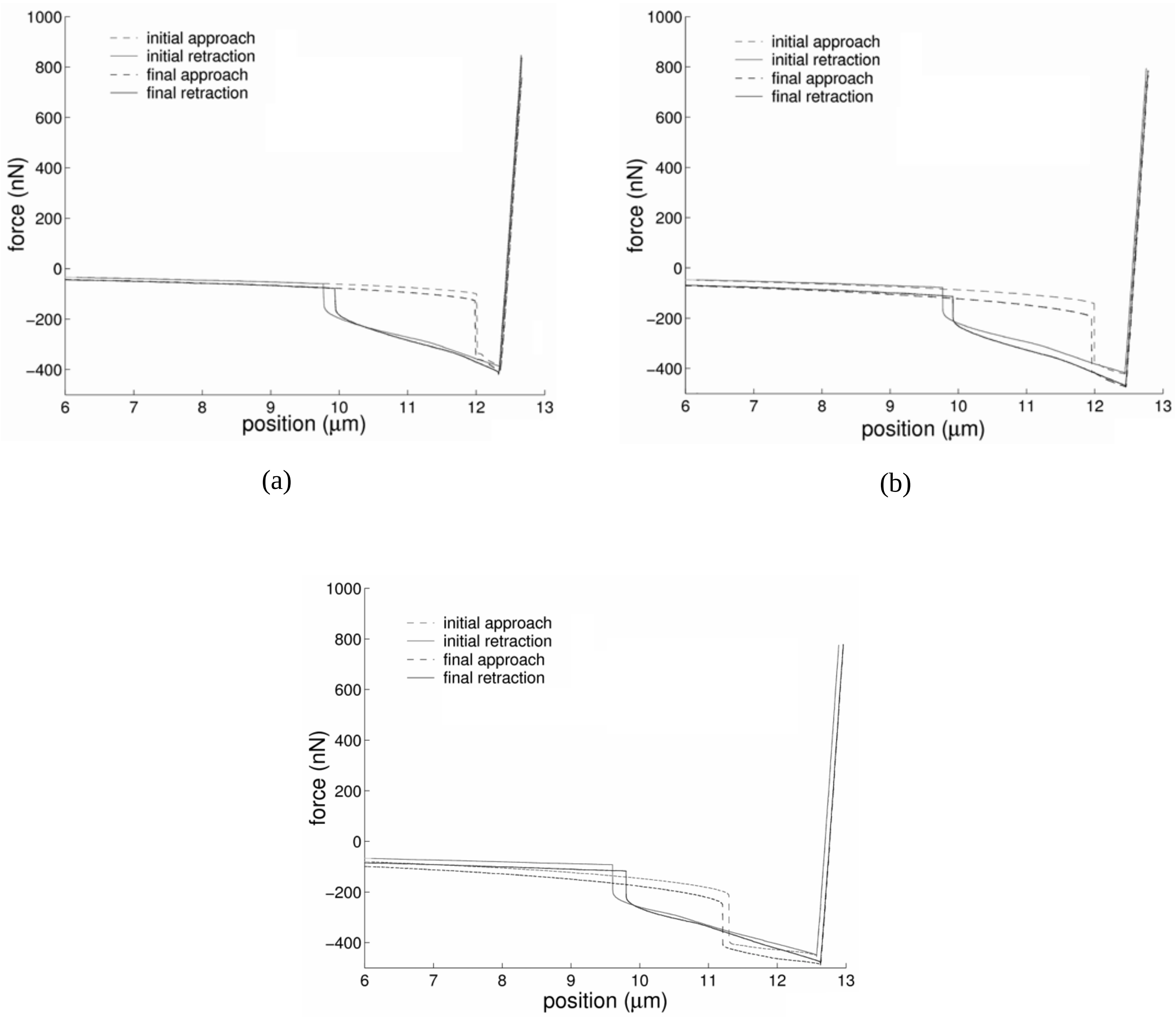

(a)

(b)

(c)

Figure 6.8: Force curve for 10 cSt silicone oil film, with extension/retraction speeds and initial film thicknesses of (a) 25 µm/s and 0.5 µm, (b) 6.4 µm/s and 0.5 µm, (c) 1.3 µm/s and 1.1 µm.

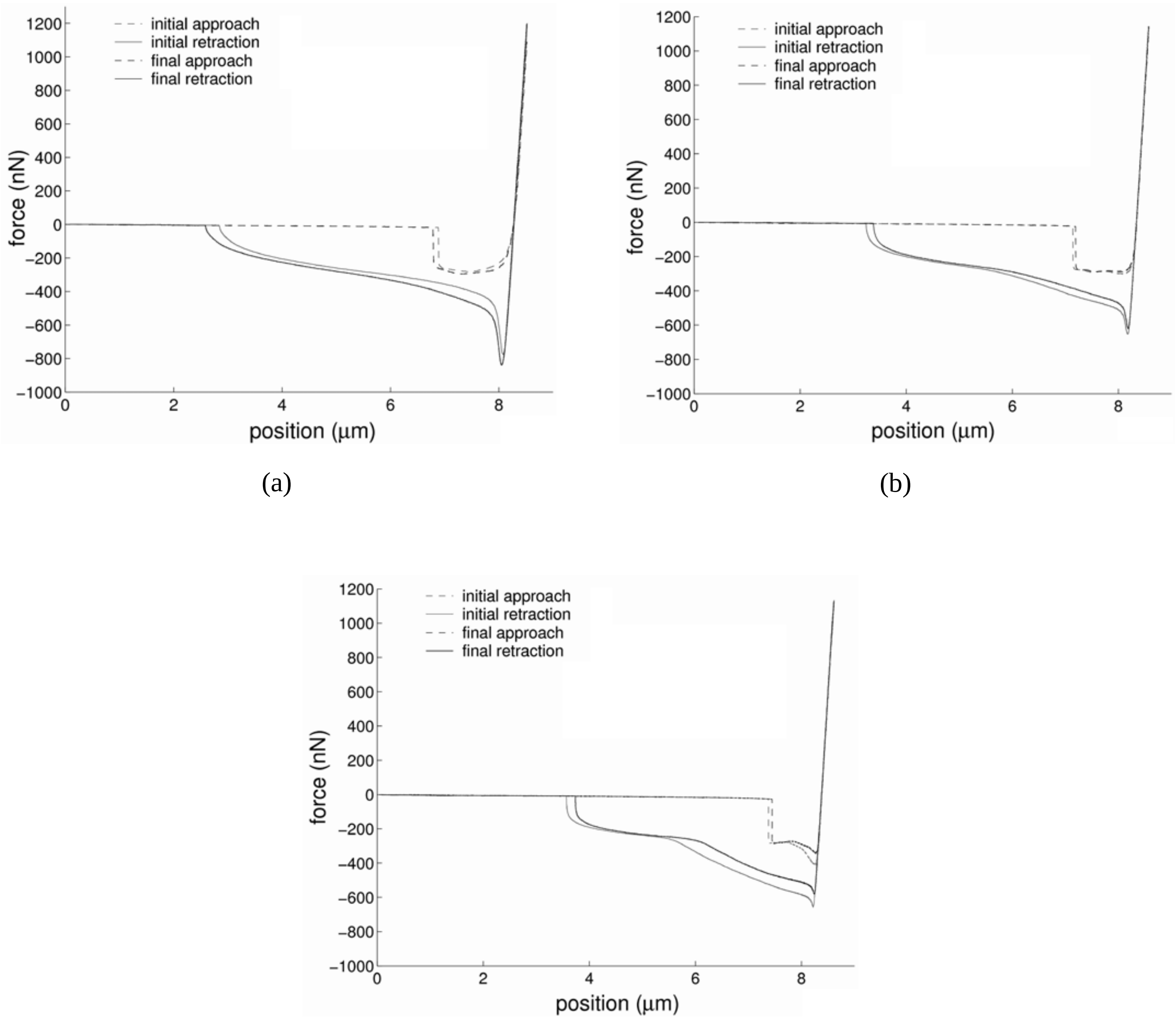

(a)

(b)

(c)

Figure 6.9: Force curve for 10 000 cSt silicone oil film, with extension/retraction speeds and initial film thicknesses of (a) 17 μm/s and 1.4 μm, (b) 4.3 μm/s and 1.1 μm, (c) 0.9 μm/s and 1 μm.

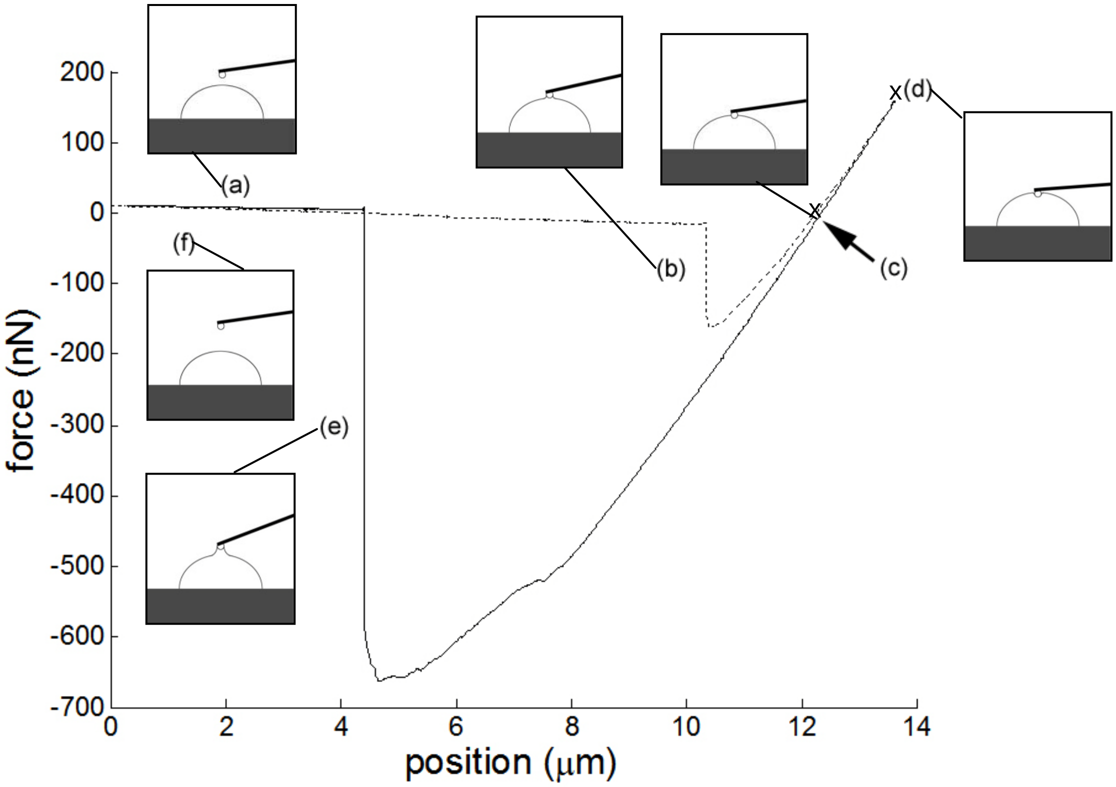

Figure 6.10: A sample force curve generated from a measurement with an air bubble in water at an extension/retraction speed of 7 μm/s. The inset figures show the stages of the extension and detachment of a solid particle into the air-liquid interface of a bubble.

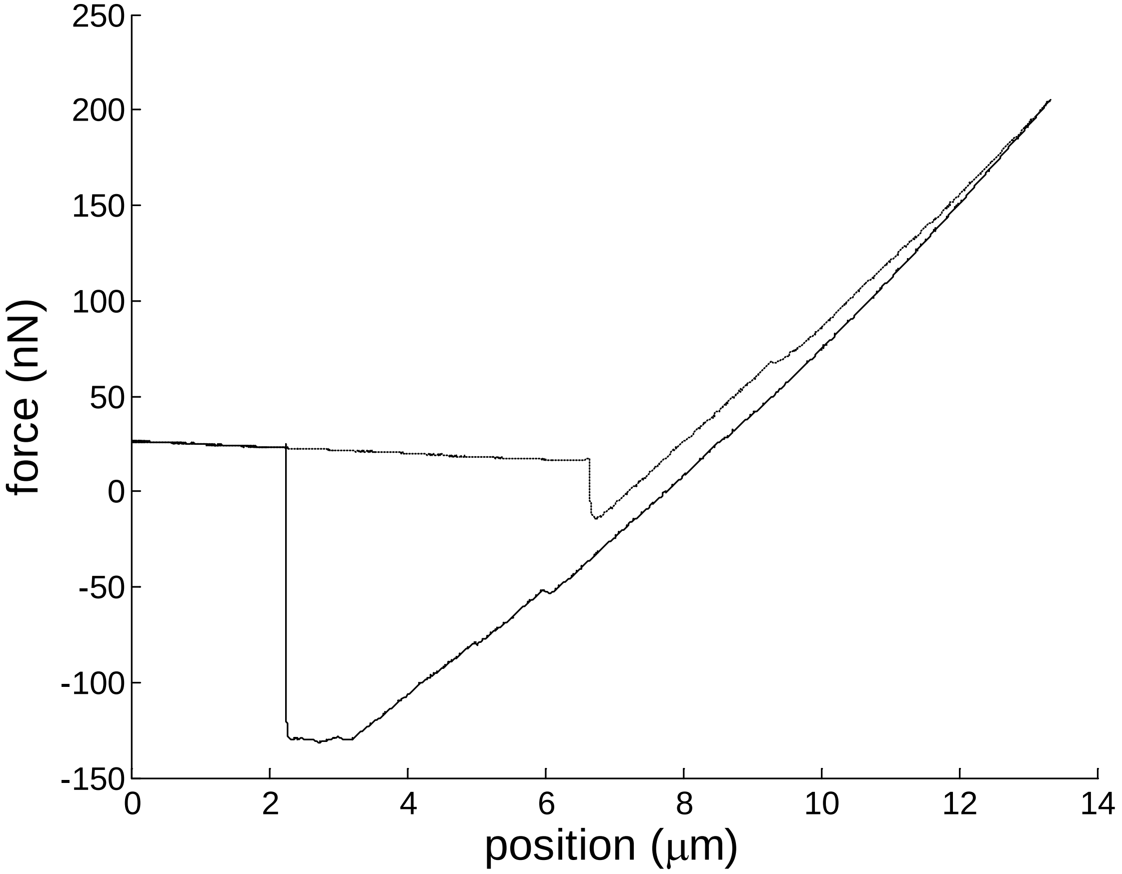

Figure 6.11: Force curve for air bubble in 1 mM SDS solution.

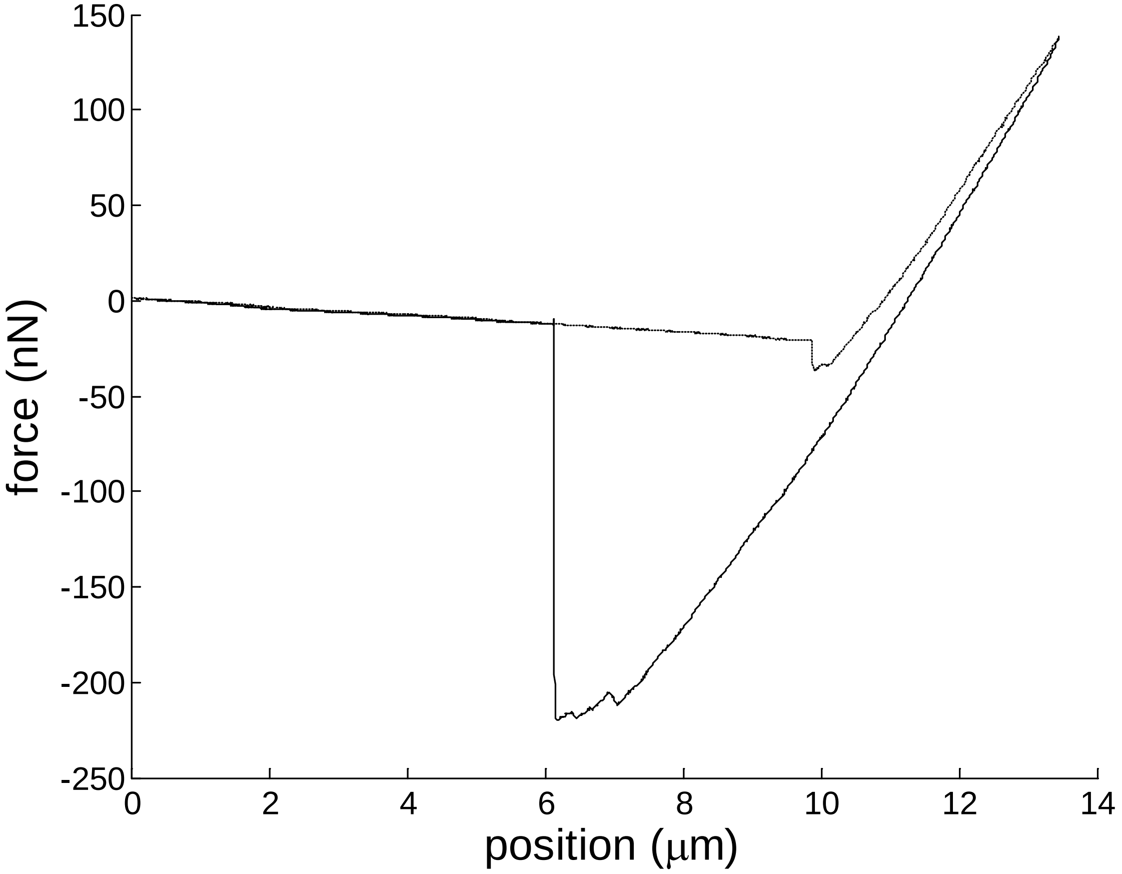

Figure 6.12: Force curve for air bubble in 2 mM SDS solution.

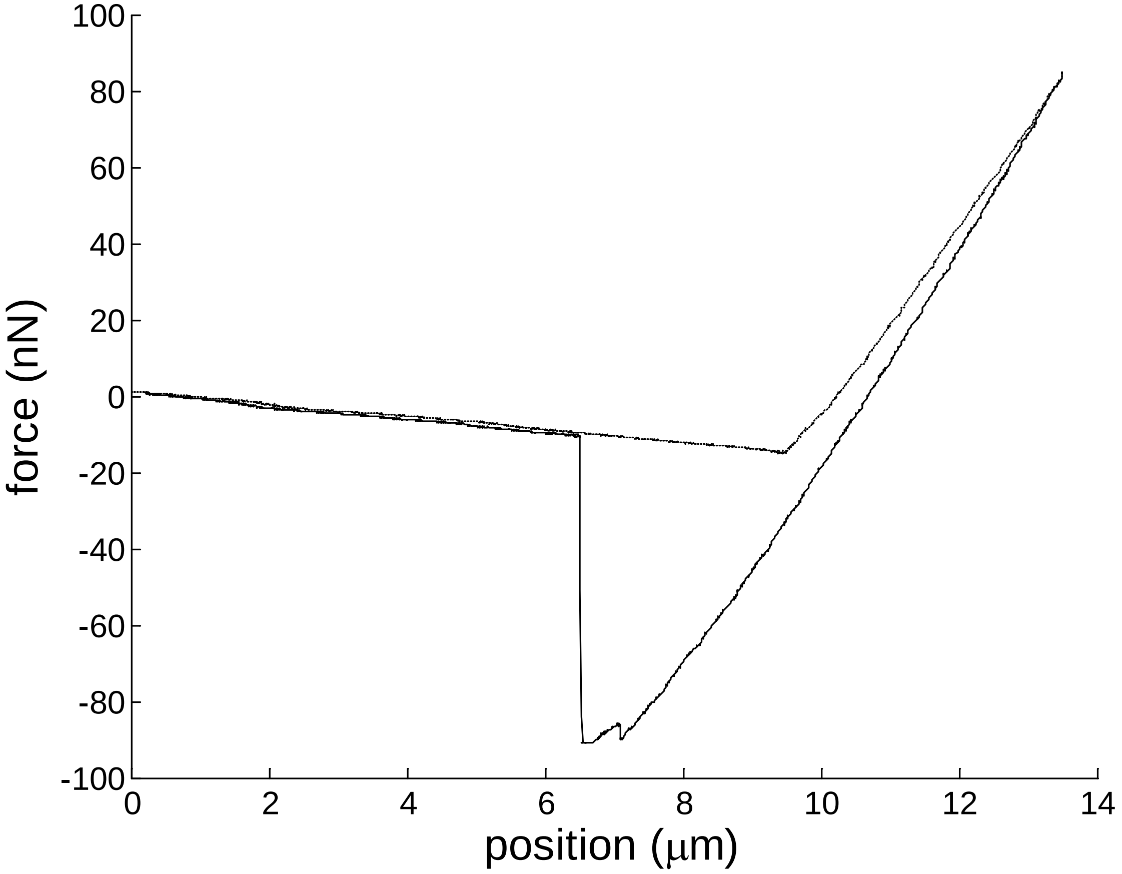

Figure 6.13: Force curve for air bubble in 4 mM SDS solution.

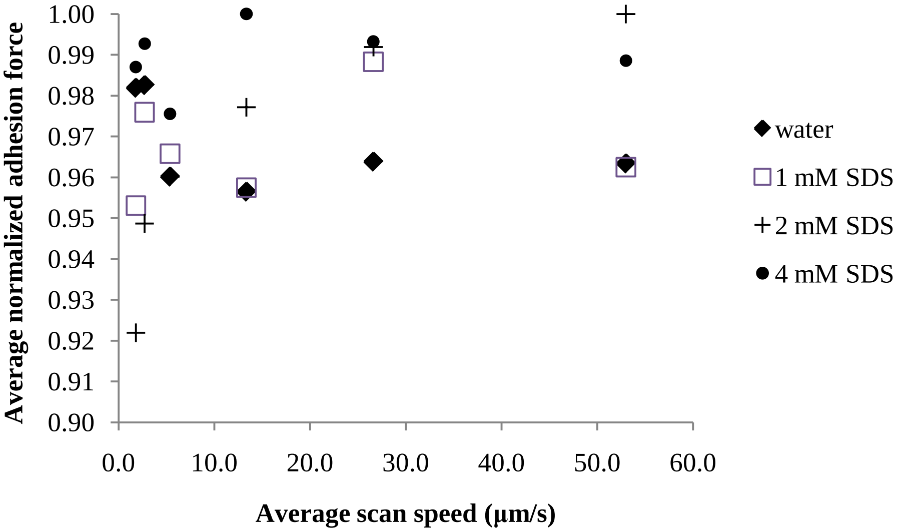

Figure 6.14: Average adhesion forces to the air bubble interfaces, normalized to the maximum value for each sample, as a function of cantilever scan speed.

In all of the figures, the dashed lines show the force on the probe as the cantilever is extended and approaches the film; the solid lines show the force as the cantilever is retracted away from the film. Positive force values mean that the cantilever, i.e. the particle, is being deflected up away from the film; negative force values mean the cantilever is being pulled toward the film.

6.3.2 Force curve interpretation

Figure 6.5 shows a force curve generated during a film experiment with water; regions of the curve labeled with letters for the following discussion. The cantilever extension/retraction speed in Figure 6.5 was 21 µm/s. The corresponding stages of the cantilever approach and retraction are illustrated in the insets of Figure 6.5. Section (a) in Figure 6.5 shows the colloidal probe approaching the air-liquid interface of the film. Point (b) is where the particle makes contact with the interface, and jumps in to form a meniscus. As the particle makes contact, a three-phase contact line with an advancing contact angle is formed as the capillary force pulls the particle into the fluid. The deflection due to the jump in depends both on the stiffness of the cantilever and of the interface. The cantilever continues to move down after contact with the film until the particle makes contact with the solid substrate at point (c). The film thickness corresponds to the distance between point (b) and point (d), the point at which the force on the cantilever is zero. Point (d) is used instead of point (c) to determine the film thickness since at point (d), the cantilever deflection is the same as it was before contact with the film. If point (c) were used, the film thickness would be underestimated due to the deflection of the cantilever. Once the particle is in contact with the substrate, the slope of the force curve corresponds to the sensitivity of the cantilever (i.e. the slope is the same as seen from the calibration curve of the cantilever). Extension of the cantilever continues until point (e).

As the cantilever is retracted, the slope of the retraction force curve between points (e) and (c) in Figure 6.5 is the same as the approach curve until the particle detaches from the solid substrate. In the sample curve shown, the downward force on the cantilever continues to increase between (c) and (f), i.e. the force value becomes more negative, until the particle detaches at point (f) and jumps out of the interface. In Figure 6.5, the particle does not completely jump out of the interface immediately at point (f); there appears to be some slip and reattachment of the contact line along the particle surface before the interface comes off completely.

A labeled sample curve for a bubble experiment is shown in Figure 6.10; corresponding approach and retraction stages are shown in the insets. Figure 6.10(a) shows a particle in the liquid phase approaching the interface of the bubble before making contact. The curve in section (a) may have a positive or negative slope if there is, respectively, repulsion or attraction between the particle and the interface. If the cantilever speed is slow, slope of the curve in section (a) may also be caused by thermal drift in the AFM.

When the particle makes contact with the interface, it jumps in, forming a three-phase contact (TPC) line, as shown in Figure 6.10(b). The jump-in event corresponds to the vertical line in the approach curve of Figure 6.10. Although this point is called the jump-in event, it is important to note that, in addition to the particle being pulled into the interface, the interface is also pulled up around the particle to form the TPC line. The ratio of these deflections (cantilever and interface) depends on the ratio of the cantilever stiffness to the stiffness of the interface. The latter will depend on the size of the bubble and surface tension of the interface.

As the cantilever is extended after the jump-in event, the particle, with the interface attached, is pushed into the bubble. When the force value is zero, at point (c) in Figure 6.10, the particle is at its equilibrium position and the interface is undeformed. The horizontal distance between (b) and (c) in Figure 6.10 gives the jump-in distance of the particle, i.e. the distance *D* from the bottom of the particle to the three-phase line. Using the value of *D* and the particle radius *R*, Equation (6.4) can be used to determine the particle contact angle θ_r.

$$\theta_r = cos^{-1}\left(\frac{R-D}{R}\right) \qquad (6.4)$$

Since the particle is going from liquid into air, the contact angle is receding.

At point (d) in Figure 6.10, the approach part of the force curve ends, and the retraction section begins. As the cantilever is retracted, the particle is pulled away from the interface into the liquid phase until the elastic force due to the bending of the cantilever is equal to the maximum adhesion force of the particle to the interface, at point (e) in Figure 6.10. At this point, there is a vertical line in the retraction curve, corresponding to the particle jumping out of the interface and the cantilever and interface snapping back to their undeflected positions. The force value at (e) in Figure 6.10 corresponds to the adhesion force on the particle given by Equation (6.1). After the particle detaches from the interface, the cantilever continues to retract along the same path as the initial approach, as shown in section (f).

6.3.3 Force at particle detachment

The force required to detach the particles from interfaces is due in part to surface tension. This component of the detachment force can be determined from Equation (6.1) in the case of a liquid film. In order to determine the magnitude of the surface tension component in the case of particle detachment from the interface of a liquid film, the position of the contact line must be known. To determine the contact line position on a particle wetted by a liquid film, the meniscus shape must be calculated.

To calculate the meniscus shape around a particle wetted by a liquid film, it was assumed that the contact line does not slip as the particle is pulled away from the solid surface. Although some slip and reattachment appears in Figure 6.5, it occurs after the particle has begun to detach from the interface. In all of the force curves, for the portions of where the particle is attached to the interface, i.e. before detachment during retraction, the contact line position appears to remain constant. With this assumption, the contact line position can be considered the same for the stages of retraction shown in Figure 6.5(c) – (f). To determine the contact line radius, the meniscus geometry at position (c) illustrated in Figure 6.5 was determined. This was done by solving the Laplace equation in differential form for an axisymmetric meniscus [13]:

$$\frac{d\sin\psi}{dr}+\frac{\sin\psi}{r}=-\frac{\Delta P}{\gamma}+\frac{\rho g z}{\gamma} \quad (6.5a)$$

$$\frac{dz}{dr}=\frac{\sin\psi}{\sqrt{1-\sin^2\psi}} \quad (6.5b)$$

where r is the radial coordinate, z is the height of the interface, and ψ is the slope of the interface as a function of r (see Figure 6.2).

The radial boundary conditions for the solution of Equation (6.5b) are that, far from the particle, the film becomes flat ($\frac{dz}{dr}=0$) and the interface height z is the same as the initial thickness of the film (the extent for the film is assumed to be very large compared to the meniscus). The position at which this boundary applies is unknown, however, as is the pressure difference across the interface, ΔP. These values are determined by fitting the numerically predicted particle contact angle and capillary force at Figure 6.5(c) to measured contact angles and capillary force values from Figures 6.5 – 6.9. The average receding contact angle for the polystyrene particles used and water, measured in Chapter 5, was 76°. The average immediate contact angle with silicone oils, also measured in Chapter 5, was 12°.

Meniscus geometries were calculated for boundary condition position and the pressure difference values over intervals of radial position from 3 – 100 µm and pressure values of 1 – 100 kPa, respectively. From the calculated menisci, the solution with the averaged lowest percent difference between the measured and calculated contact angles and capillary force was selected. The intervals of the boundary position and pressure difference were refined until the error value was less than 3%. The contact line radius is then determined from the position of the fitted meniscus, as show in Figure 6.15.

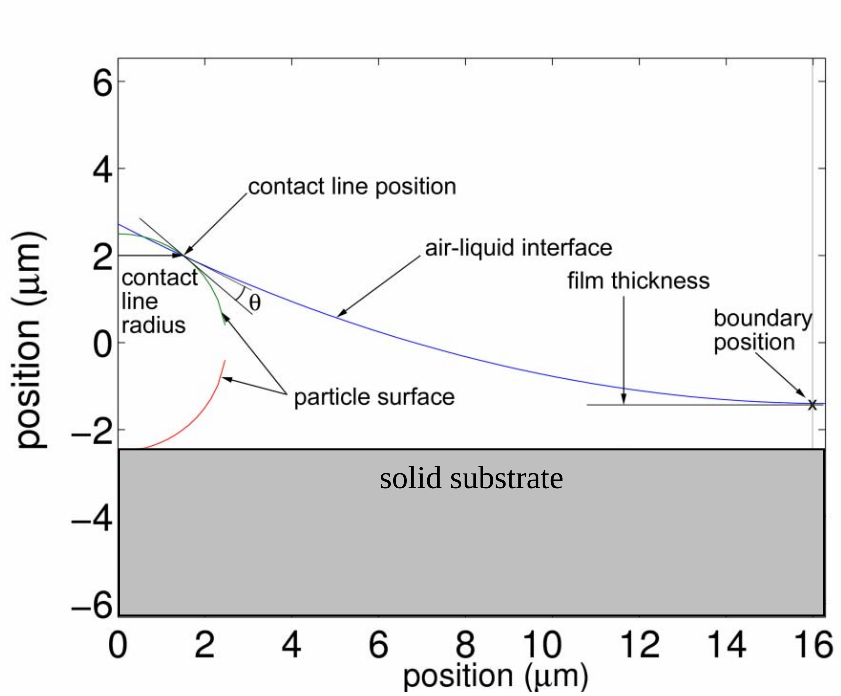

Figure 6.15: Numerically calculated meniscus profile for a polystyrene particle in contact with a silicone oil film; the solid substrate is shown in gray.

The meniscus geometry immediately before the particle detaches from the interface (Figure 6.5(f)) is determined similarly. Using the previously calculated contact line position and previously measured receding particle contact angle, the calculated meniscus geometry is fitted using the boundary position and pressure difference as parameters. The capillary force on the particle can then be calculated using Equation (6.1) and the interface angle ψ at the contact line. Numerically predicted capillary force values are given in Table 6.2. The calculated force values agree with the measured detachment force values, i.e. the force value just as the particle detaches from the interface. This agreement indicates that, at the point where the particle detaches, only the capillary force predicted by Equation (6.1) is acting on the particle.

Table 6.2: Adhesion force and capillary number values from the film experiments

Liquid	**Retraction Speed (μm/s)**	**Particle detachment force (nN)**	**Calculated adhesion force (nN, Eqn 6.1)**	**Maximum downward force (nN)**	**Film thickness (μm)**	**Rate of film thickness change ($\times 10^3$ μm/s)**	**Capillary number ($\times 10^5$)**
Water	21	335 ± 5	368	335 ± 5	1.5	77	0.03
	142	340 ± 7	368	713 ± 4	0.4	25	0.2
5 cSt silicone oil	0.7	100 ± 15	104	315 ± 11	0.4	0.4	0.02
	3.6	90 ± 15	104	330 ± 10	0.4	0.2	0.1
	14	100 ± 15	104	289 ± 7	0.4	0.1	0.4
10 cSt silicone oil	1.3	105 ± 15	98	488 ± 12	0.5	0.1	0.1
	6.4	120 ± 15	98	473 ± 8	0.5	0.1	0.3
	25	120 ± 15	98	420 ± 12	1.1	0.2	1.3
10 000 cSt silicone oil	0.9	-	85	654 ± 14	1.4	0.2	43
	4.3	-	80	682 ± 14	1.1	0.1	214
	17	-	80	837 ± 14	1	0.2	850

In the bubble experiments, the detachment force corresponds to the minimum force value on the force curve (Figure 6.10(e)). Average adhesion force results from the bubble experiments using the water and SDS solutions are given in Table 6.3. The force values represent the force required to pull a particle from the interface into the liquid phase.

Table 6.3: Measured adhesion force and contact angles (CAs) in the bubble configuration. Error values are based on the standard deviation of the results

SDS concentration (mM)	**Force (nN)**	**Calculated Force Eqn (6.2), (nN)**	**Advancing CA Eqn (6.2), (°)**	**Receding CA Eqn (6.2), (°)**	**CA hysteresis (°)**
0	433 ±	282 ± 144	76 ± 8	58 ± 19	18 ± 14
1	262 ±	161 ± 80	57 ± 9	44 ± 13	13 ± 10
2	201 ±	64 ± 15	50 ± 1	32 ± 6	18 ± 7
4	110 ±	0	38 ± 1	0	38 ± 1

The contact line position can be determined from the contact angle of the particle and bubble interface. As explained earlier, when the particle makes contact with the bubble (unrestricted wetting due to large liquid volume), the interface remains flat (with respect to the particle size) and the particle is initially displaced into the air phase to form the appropriate contact angle (it is assumed that the contact line remains pinned until detachment). Since a meniscus is not formed, solution of the Laplace equation is not required to determine the surface tension force [8].

Force values calculated from the receding contact angles using Equation (6.3) are also given in Table 6.3. The receding contact angles were determined from the approach curve using Equation (6.4). Although of similar order of magnitude, the calculated force values are lower than the measured values. This is because the contact angle is advancing when the particle is pulled out of the interface, and advancing contact angles tend to be higher than receding. As such, the calculated values underestimate the adhesion force.

The advancing contact angles can be determined from the measured adhesion forces using Equation (6.2), and are shown in Table 6.3 with the contact angle hysteresis values. In the case of the 4 mM SDS solution, the high hysteresis value of 36° occurs because the measured receding contact angle was 0°. This is because there was no apparent jump-in event in any of the force curves, as illustrated in Figure 6.13. There was an adhesion force measured as the particle was retracted (Table 6.3) – i.e. a three phase line was formed, but no jump-in appeared to occur. This implies that the contact line advanced along the particle surface during the cantilever approach.

6.3.4 Maximum force during retraction

In the bubble experiments, the detachment force was the largest force on the particle observed as the particle was retracted into the liquid phase. In the film experiments however, the force when the particle detached was not typically the largest downward force value as the particle was pulled from the interface into the air phase. For the silicone oils, the detachment force values occurred just as the particle detached from the solid substrate during retraction. In the case of water, when the cantilever was retracted at 21 µm/s, the largest downward force occurred just before the particle detached from the interface, as in the case of the bubble experiments. This behavior is expected if the capillary force is dominant, holding the particle to the interface as it is retracted. When the cantilever was retracted from the water film at 142 µm/s, the downward force initially increased, as for the silicone films, and then decreased. Since the increase or decrease of the force was dependent on the retraction speed and film viscosity, this suggests it is due to hydrodynamics. The film thickness may also affect this behavior as, like viscosity, it restricts the liquid flow.

In the bubble configuration, particles can be freely displaced into the air-liquid interface, and hence the interface remains flat around the particle (since the bubble is much larger than the particle, curvature of the bubble may be neglected). In the film configuration, since the particle cannot be displaced into the rigid substrate, a concave meniscus is formed around the particle. The pressure in the meniscus region is lower than that in the air, according to the Laplace equation (Equation (6.3)). The low pressure in the meniscus region has two consequences: pulling the particle into the liquid phase due to higher pressure outside of the meniscus, and liquid flow from the rest of the film into the meniscus region.

The pressure difference across the interface acts on the immersed surface of the particle, not on the contact line. Therefore, the particle is not pulled out of the interface even though the total force on the particle exceeds the force required to overcome the capillary force at the contact line, as seen by comparing the calculated force at detachment and the largest force values given in Table 6.2. The pressure difference across the interface will change as it is offset by the flow of liquid from the surrounding film. In the bubble experiments, since there is no meniscus formed around the particle, the Laplace pressure is negligible, and thus only the capillary force at the contact line must be overcome to detach the particle from the interface.

For the films of low-viscosity liquids, the force on the particle at detachment from the interface agreed well with the values calculated using Equation (6.1). Even though the detachment force was not the largest downward force on the particle, there was a clear discontinuity in the retraction curves when the particle broke away from the interface as seen in Figures 6.5 – 6.8. This is consistent with the Laplace pressure being offset by liquid flow. As the particle is pulled away from the interface, the pressure difference across the interface increases, as described above. This accounts for the increase in downward force in addition to the capillary force. The pressure difference is also offset as it causes liquid from the film to flow into the meniscus region. Once the additional pressure difference is completely offset by the liquid flow, the capillary force is the limiting force holding the particle to the interface. In the case of the 10 000 cSt silicone oil, the force at detachment could not be determined as there was no clear jump-out event; this is also likely due to hydrodynamic effects.

The strength of viscous forces relative to capillary forces is reflected by the capillary number:

$$c = \frac{\eta U}{\gamma} \quad (6.6)$$

where U is the particle speed. The particle speed is used here because it is assumed to be proportional to the liquid velocity. The capillary numbers for the film experiments are given in Table 6.2. For the 10 000 cSt silicone oil, the flow is dominated by viscous effects, which explains the difference between the curves in Figure 6.9 and, for example, Figure 6.5 for water. Two different capillary number regimes can be seen by comparing force curves. In the force curves for experiments with capillary numbers less than 10^{-5}, there was a distinct jump-out region in the retraction force curves when the particles detached, appearing as a vertical line. When the capillary number was greater than 10^{-5}, i.e. for the 10 000 cSt silicone oil, the particle detachment was gradual, and there was no distinct vertical line.

The film thickness decreased as the measurements were performed, as can be seen in Figures 6.5 – 6.9 by comparing the jump-in position (point (b) in Figure 6.5) of the initial and final force curves, as shown in Figure 6.16. For water (Figures 6.5 and 6.6), the change in thickness is most likely due to evaporation. For the silicone oils (Figures 6.7 – 6.9), evaporation is not significant. In this case, further spreading of the liquid on the glass substrate is likely the reason for the decrease in film thickness.

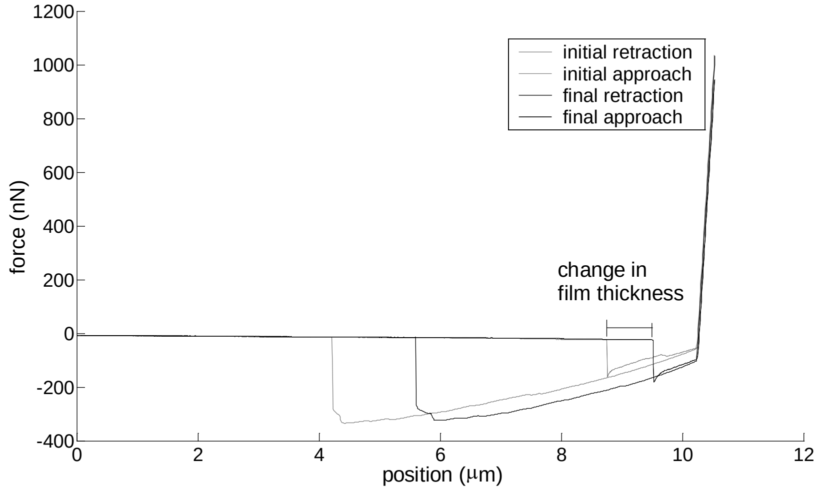

Figure 6.16: The change in film thickness over repeated measurements, shown here for the water film with 21 μm/s extension/retraction speed.

6.3.5 Mucus simulant results

Figure 6.17 shows a sample curve from an experiment using the locust bean gum gel which is used as a mucus simulant. In these experiments, the particles approached a 1 mm thick layer of locust bean gum from air. The jump-in force here is much stronger than in other experiments (~400%). Also, the jump-in distance is larger than the particle diameter, even though the particle was not completely engulfed, as seen by observation of the cantilever using the microscope on which the AFM was mounted. Both of large jump-in force and distance are due to the elasticity of the mucus simulant. As the particle forms a three phase contact line with the surface, the gel phase is pulled up as it wets the particle. This creates tension within the bulk gel which accounts for the additional force felt by the particle. The adhesion force in these experiments was too large to be measured with the cantilevers used. This is also due to the gel elasticity, as additional force would be required to deform the interface before pulling the particle out due to the elasticity of the bulk liquid phase.

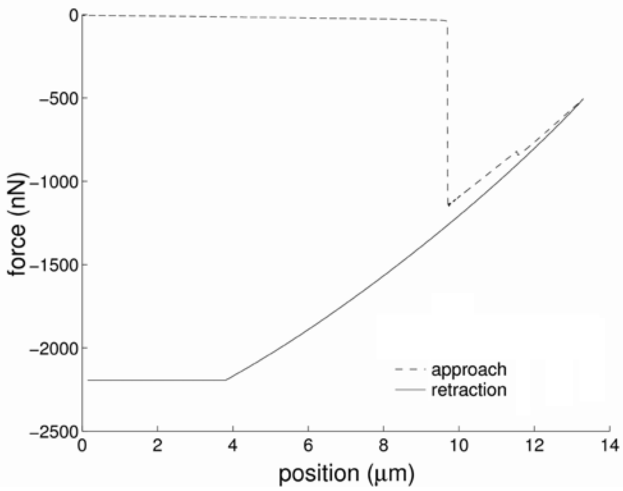

Figure 6.17: Sample force curve from an experiment with mucus simulant; the extension/retraction speed was 28 µm/s.

6.3.6 Implications for magnetic targeting of particles

In terms of particle retention in the airways, these results show that the force required to pull a particle from an interface into a liquid is on the order of ~500 nN. This is considering only the surface tension force, as was shown to be valid for the bubble experiments. To consider the implications for magnetic targeting, consider the magnetic force on a spherical particle 5 µm in diameter with a magnetic susceptibility of 0.3. Such particles are the appropriate size for aerosol drug delivery to the airways, and similar to those used in previous studies of magnetic targeting in the airways [1][14][15].

In a magnetic field with a flux density of 0.5 T and a flux density gradient of 100 T/m, the force on the particle will be ~1 nN. Such a magnetic field is near the maximum that can be practically produced; see [16]. Pulling individual particles through the mucus layer appears impractical. However, the force on particle aggregates will be larger due to their size, and as such may be possible to pull through the interface. Retention of larger particles (~180 µm characteristic size) in magnetic fields of up to 0.2 T with a 10 T/m gradient was demonstrated in [3].

The film experiment results show that the hydrodynamics of the liquid film must also be considered to determine the force required to pull particles across an air-liquid interface of the mucus layer, and may aid in pulling the particle into the liquid phase. Since the goal in the proposed application is to pull particles into a liquid layer, the pressure difference across the meniscus around a particle would reduce the force required if hydrophilic particles are used.

Limiting the speed of the particles, i.e. by using the weakest effective magnetic field, could also help in pulling the particles through the mucus layer.

Mucus elasticity would greatly increase the magnetic force required to pull particles across the interface, as shown by these results. The effect of elasticity may be overcome the use of additional methods, such as mucolytics, as proposed in [14], to alter the properties of the mucus rather than require magnetic fields strong enough to overcome the resistance to pulling the particles through.

6.4 Conclusions

An order-of-magnitude calculation considering only capillary force shows that the estimated force required to pull individual particles through an interface would require stronger magnetic fields than can be practically produced. However, the effect of changing Laplace pressure and associated liquid flow in liquids film as the particle is pulled from the interface has been shown to be significant. The experiments showed that the Laplace pressure in liquid films will hold particles in the liquid film, and may be stronger than surface tension force.

Elasticity of the liquid phase increases the force required to pull a particle from an air-liquid interface beyond that predicted when only considering capillary force, as was demonstrated by the experiments with the mucus simulant. The force would be similarly increased when pulling particles into the interface. In practice, however, this could be overcome by the application of mucolytics [14].

The differences between the results of the bubble and film experiments show the effect of a constrained liquid phase on particle detachment from interfaces, which has not been demonstrated in previous studies that considered only cases where the liquid phase was unconstrained. The bubble experiments in this study were similar to those in previous works by Butt et al. [1], and confirmed the previous findings in the literature. The bubble experiments demonstrated that when detaching particles from air-liquid interfaces with unconfined liquid phases (i.e. large liquid volume) only the capillary force on the particle must be overcome. This is in contrast to the liquid film experiments, which showed that when the motion of the liquid phase is constrained (i.e. low liquid volume), the Laplace pressure on the particle must also be considered. In the context of magnetic targeting, the Laplace pressure may reduce the force required to pull particles into the liquid phase.

6.5 References

1. Gillies, G., Kappl, M. and Butt, H-J. 2005. Direct measurements of particle-bubble interactions. Adv. Colloid Interfac. Sci., Vol. 114, pp. 165-172.

2. Pitois, O. and Chateau, Xavier. 2002. Small Particle at a Fluid Interface: Effect of Contact Angle. Langmuir, Vol. 18, pp. 9751-9756.

3. Ally, J., Amirfazli, A. and Roa, W. 2006. Factors affecting magnetic retention of particles in the upper airways: an in vitro and ex vivo study. J. Aerosol Med., Vol. 19, pp. 491-509.

4. Amirfazli, A. 2007. Magnetic nanoparticles hit the target. Nat. Nanotechnol., Vol. 2, pp. 467-468.

5. Model studies of magnetic particle retention in the conducting airways. Ally, J., Amirfazli, A. and Roa, W. [ed.] W. Badawy and W. Moussa. Los Alamitos, USA : IEEE Publications, 2005. Proc. ICMENS 2005, Banff, Canada. pp. 182-184.

6. Sleigh, M.A., Blake, J.R. and Liron, N. 1988. The propulsion of mucus by cilia. Am. Rev. Respir. Dis., Vol. 137, pp. 726-741.

7. Schürch, S., et al. 1999. Particles at the airway interfaces of the lung. Colloid Surface B, Vol. 15, pp. 339-353.

8. Scheludko, A.D. and Nikolov, A.D. 1975. Measurement of surface tension by pulling a sphere from a liquid. Colloid Polym. Sci., Vol. 253, pp. 396-403.

9. Preuss, M. and Butt, H-J. 1998. Direct measurement of particle-bubble interactions in aqueous electrolyte: dependence on surfactant. Langmuir, Vol. 14, pp. 3164-3174.

10. Ecke, S., Preuss, M. and Butt, H-J. 10, 1999. Microsphere tensiometry to measure advancing and receding contact angles on individual particles. J. Adhes. Sci. Technol., Vol. 13, pp. 1181-1191.

11. Amirfazli, A. and Neumann, A.W. 2004. Status of the three-phase line tension: a review. Adv. Colloid Interfac. Sci., Vol. 110, pp. 121-141.

12. King, M., Brock, G. and Lundell, C. 1985. Clearance of mucus by simulated cough. J. Appl. Physiol., Vol. 58, pp. 1776-1782.

13. Hadjiiski, A., et al. 1996. Film trapping technique: precise method for three-phase contact angle determination of solid and fluid particles of micrometer size. Langmuir, Vol. 12, pp. 6665-6675.

14. Ally, J., Roa, W. and Amirfazli, A. 2008. Use of mucolytics to enhance magnetic particle retention at a model airway surface. J. Magn. Magn. Mater., Vol. 320, pp. 1834-1843.

15. Ally, J., et al. 2005. Magnetic targeting of aerosol particles for cancer therapy. J. Magn. Magn. Mater., Vol. 293, pp. 442-449.

16. Takeda, S., et al. 2007. Development of magnetically targeted drug delivery system using superconducting magnet, J. Magn. Magn. Mater., Vol. 311, pp. 367-371.

Chapter 7: Conclusions

7.1 Deposition

Magnetically targeted aerosol particle deposition was shown to be feasible under simulated airway conditions. Spherical iron particles 1 – 3 μm in diameter were deposited in an *in vitro* model airway using various arrangements of permanent magnets. These experiments demonstrated the importance of the magnetic field gradient in particle deposition and of the distribution of aerosol particles in the flow. A numerical model was also developed to predict the trajectories of the aerosol particles using independent magnetic field and fluid flow datasets. This approach to predicting particle deposition is useful for the development of a magnetic targeting system, as extensive data and models of air flow in the airways are available in the literature [1], and magnetic fields can be readily modeled using finite element analysis.

The numerical model was validated using the experimental results for a single magnet. With multiple magnets, the particle deposition after particles passed through the field of an initial magnet was consistently greater than predicted for subsequent magnets. This was likely due to aggregation of the particles changing the size distribution, and increasing the effective particle size and thus the force acting on the particles.

The numerical model of aerosol capture showed that the aerosol flow rate had a limited effect on the amount of particle deposition. The main factor was the proximity particle trajectory to the magnets. The closer the particles passed to the magnets, the greater the field strength and gradient, and thus the greater the force on the particles. This explains the importance of the particle distribution in the aerosol flow in determining the amount of deposition, as there is a spatial bias.

The results of the particle deposition experiments showed that high-gradient magnetic fields are required for particle deposition. When a uniform field was applied, the amount of particle deposition was negligible. However, since high gradients are difficult to produce over large distances, particle aggregation must also be exploited for effective deposition. Since particles will aggregate in uniform magnetic fields, which are easier to produce over large distances, e.g. using Helmholz coils, a possible strategy for deposition is to use a uniform field to aggregate the particles in aerosol, increasing the effective particle size, and allowing the particles to be captured by a weaker gradient field at the target site.

7.2 Retention

Particle retention was studied using two experimental models: an *in vitro* model that used a liquid flow to simulate mucus clearance, and an *ex vivo* frog palate model. The *in vitro* model consisted of a liquid flow along the bottom surface of a channel, and allowed the effect of varying liquid viscosity to be studied through the use of different liquids. The *ex vivo* model consisted of an excised frog palate. The tissue on the palate is structurally and functionally similar to that in the human airway, and remains active after the palate is harvested. In both cases, magnetic fields were applied with permanent magnets. The frog palates provided a realistic model of mucus clearance, but did not allow for precise control of the mucus viscosity or transport rate. Coarse control of mucus viscosity and elasticity was possible through the use of mucolytics.

Mucus viscosity proved to be the most significant factor in determining the force required for magnetic particle retention in the airways. This is because it affects both the force required to hold the particles at a target site against the flow of mucus as well as the size of the aggregates formed by particles after deposition. As in the case of magnetic aerosol deposition, particle aggregation greatly enhances the effectiveness of magnetic fields in retaining particles at the airway surface. The size of aggregates formed in the *in vitro* model was correlated with the viscosity of the liquid used. Similar behavior was observed in the frog palate experiments. On frog palates, particle retention was only possible when the mucus viscosity was reduced by treating the palates with mucolytic. With mucolytics applied to the palates, larger particle aggregates formed than on the untreated palates, and these were retained by the magnetic field.

The frog palate experiments also showed that aggregation and retention could be enhanced by the magnetic field orientation. A radial field in the plane of mucus surface that concentrates particles in a small region promotes retention by producing larger aggregates. The component of the field directed into the palate also helped retain particles. The particles pushed down on the cilia, disrupting the mucus clearance mechanism, which helped retain the particles. The particles did not penetrate the mucus, however, as indicated by clearance once the magnetic field was removed.

7.3 Interface penetration

Pulling particles through the mucus layer is desirable because it would prevent particles from being cleared after the magnetic field is removed. In order to determine the force required for particles to penetrate an air-liquid interface, experiments were performed using the colloidal probe technique. Particles attached to tipless atomic force microscope cantilevers were brought into contact with and then pulled out of the air-liquid interfaces of various liquid films.

In experiments performed with the air-liquid interfaces of liquid films, however, the maximum force on the particles as they were pulled out exceeded the capillary force at detachment, which could be predicted theoretically [2]. This was due to the increasing Laplace pressure in the liquid as the particle was withdrawn. This result shows that hydrodynamics, i.e. Laplace pressure, play a significant role and will tend to pull deposited hydrophilic particles into the liquid. This may facilitate pulling particles through the mucus layer, as the Laplace pressure may be stronger than the surface tension at the contact line.

Experiments performed with a mucus simulant showed that the elasticity of the liquid increased the force required to pull the particle from the interface, to the point where the particle could not be withdrawn far enough to be removed due to the limited range of the atomic force microscope. The forces for any deformation of the liquid were larger than for water or silicone oil due to the ability of the viscoelastic mucus simulant to resist deformation. Similar behavior would be expected of mucus in the airways when pulling magnetic particles into the layers. This result suggests that mucolytics or large particle aggregates would be required in order to pull particles through the interface.

7.4 Drag force on individual particles

Aggregation of particles immediately after deposition is a key factor in particle retention. Particle aggregation at the air-liquid interface of the airways depends on the particle mobility, i.e. the drag force on the particles as they move along the interface. The drag force on particles at air-liquid interfaces was studied using various liquids to simulate different properties of mucus.

The results of the particle drag experiments showed that for air-liquid interface without surfactants present, the theoretical model developed in [3] accurately predicts the drag force on particles moving along the interface. This was demonstrated using water, which also showed the validity of the method used by agreement with other results in the literature. The results of the experiments with silicone oil showed that the theoretical results can be extrapolated to contact angles of less than 20°, and that they are valid for a wide range of viscosities, allowing the bulk viscosity component of the drag on a particle at the air/liquid interface of the airways to be predicted. These experiments provided the first verification of the theoretical model for low contact angles and high bulk viscosity.

The particle drag experiments with surfactant (sodium dodecyl sulfate) showed that surfactants greatly increase the resistance to particle motion of the interface due to the surface tension gradient caused as the particle distorts the surfactant concentration around it as it moves along the interface. The resistance was found to increase non-uniformly with surfactant concentration. This was likely due to the presence of minute amounts of dodecanol in the surfactant solutions. The surface resistance was also found to be dependent on particle velocity. This dependence has not been noted previously, as other experimental studies have focused on surfactant concentrations above the CMC and, with the exception of [5], been limited to the study of Brownian motion, i.e. low particle velocity. This velocity dependence is also not predicted theoretically in [3] or other analyses, because in these studies, the addition resistance to particle motion due to surfactants is included in constant surface shear and dilatational viscosity terms which cannot account for it. In terms of magnetic particle retention, the additional drag force due to surface tension gradients would limit the size of aggregates formed by magnetic particles in the airways, increasing the magnetic field required to retain the particles at the target site.

7.4.1 Strategies for magnetic targeting in airways

Both particle deposition and retention require high-gradient fields to be applied by magnets outside of the body, at distances of 10 cm or more from the target site. Even if extremely large magnets are used, high gradients at such distances are difficult to produce. A ‘brute force’ solution to this challenge seems unlikely – simply increasing the size and power of magnets will not work. Better understanding of magnetic particle behavior in the body, i.e. particle aggregation and the physiological environment, is required to make optimal use of fields that can be practically produced.

The orientation of magnetic fields with respect to the target site and aerosol flow must also be considered. Magnetic fields applied by external magnets will always pull particles out of the body, toward the magnet. For particles to be retained, they must be held against a tissue surface. If a target site is located on the inside of the dorsal surface of the trachea, for example, magnets applied from the ventral surface of the body will be ineffective. Possible solutions to this issue include the use of magnetic seed particles to create local field gradients within the airways, and improving targeting over long distances as discussed above.

Particle aggregation was found to be a key factor in facilitating both particle deposition and retention. Particle aggregation immediately after deposition is strongly correlated to the mucus consistency. The experiments measuring the drag force on individual particles suggest that the surfactant layer of the mucus may also affect particle aggregation. The incorporation of mucolytics into the administration of magnetic aerosol particles may significantly help with particle retention.

7.5 Future work

Particle deposition was studied by using an experimental model with a straight channel and uniformly distributed aerosol. The simplicity of this model allowed for verification of a numerical particle deposition model. The next two steps in the study of magnetic particle deposition are to study deposition in a bifurcation and deposition in an airway model after the aerosol passes through a realistic mouth/throat geometry.

Studying deposition in a bifurcation would allow the development of a magnetic targeting approach to guide particles to one branch of the bifurcation preferentially. This is in itself a useful goal as such a system could be used to target particles to one lung instead of both. Such crude targeting would still represent a dramatic improvement in targeted aerosol drug delivery. The air flow in a bifurcation would be similar to that in the airways, as would the particle distribution. Also, since bifurcations are the basic element of the airway structure, this study would suggest the extent to which particles can be targeted after the aerosol passes through successive generations of the airways.

Deposition of aerosol particles passing through a realistic mouth-throat geometry must also be studied. Passing through a mouth-throat geometry will produce a certain amount of turbulence and particle distribution in the aerosol flow. Studying a realistic mouth-throat geometry would allow design of a targeting system that would work with the aerosol particle distribution that would enter the trachea. Such a model would also produce more realistic turbulence, which may also be important, as it may affect particle aggregation due to shear forces between particles and on the aggregates. Such studies would also function as a bridge between the fundamental base knowledge developed in this thesis and ultimate clinical applications.

The results of the particle drag experiments have provided insight into the motion of particles pinned at air-liquid interfaces. The next step in this study would be the study of particle interactions leading to aggregation. As an immediate next step, the interaction of two magnetic particles in a uniform field should be studied. This would show how mucus properties, including viscoelasticity and the surfactant layer, will affect aggregation.

The most important particle property for retention is the particle size, as the magnetic force on a spherical particle increases with the cube of the particle diameter. The particle magnetic susceptibility is also important, however, this is subject to diminishing returns as it is increased, as the increased particle magnetization is countered by the demagnetizing field within the particle. In the case of non-spherical particles, the particle size is similarly important; particle aggregates could be considered as large, non-spherical particles. Non-spherical particles would also experience magnetic torques, and may have different aggregation characteristics e.g. due to strong gradients at corners or sharp edges. The effects of particle and aggregate shape could be exploited to enhance retention, e.g. to disrupt clearance by rotating the particles or using particle shape to enhance aggregation.

Further study of individual particle motion is required on a functionally realistic mucus layer. As discussed in Chapter 1, the frog palate model is not suitable for microscopic studies. A possible alternative is the use of cultured airway epithelium models. Such models have been used to study mucus transport [6]. Cultured airway epithelium models consist of tissue cultured from human lungs, and are structurally and functionally similar to tissue in the human airway. As the tissue is grown under controlled conditions, it is uniform and would be more suitable for microscopic experiments than the frog palates. Cultured tissue would be structurally similar to the tissue in the airway, and would have a fully expressed mucus layer with surfactant when grown under proper conditions.

Using cultured tissue models, particle drag and mucus penetration experiments, similar to those in Chapters 5 and 6 could be performed on a real airway surface. This would provide insight into the levels of importance of the various factors studied in isolation in Chapters 5 and 6 (mucus viscosity, elasticity, and the surfactant layer) for particle retention on a realistic airway surface. Particle interaction experiments, as described above, would also help to understand the aggregation process.

As the goal of this research is to develop a magnetic aerosol targeting in the airways for clinical use, two matters are ultimately needed: demonstration of clinical effectiveness in animal models and demonstration of effective targeting in a human-scale model. In medical science, animal studies are used to validate protocols prior to clinical trials. However, great care is required in comparing animal and human studies due to the issue of scale as well. Scaling of magnetic fields may limit the usefulness of animal model validation from an engineering perspective, hence the need for full-scale *in vitro* testing. Consideration of magnetic field and force scaling is necessary to ensure effective treatment achieved in animal tests can be replicated on a human scale.

To address these issues, long term future work must be pursued along two avenues. Investigations similar to those performed in [7] must be performed to validate magnetic targeting apparatus designs. In addition to verification in animal models, however, full-scale magnetic targeting apparatus must be developed and tested using full-scale *in vitro* models to ensure that the magnetic fields can be scaled up to achieve effective dosages at the target site.

7.6 References

1. Finlay, W. The Mechanics of Inhaled Pharmaceutical Aerosols: An Introduction. London, UK : Academic Press, 2001.

2. Scheludko, A.D., Nikolov, A.D. 1975. Measurement of surface tension by pulling a sphere from a liquid. Colloid Polym. Sci., Vol. 253, pp. 396-403.

3. Danov, K., Aust, R., Durst, F., Lange, U. 1995. Influence of the surface viscosity on the hydrodynamic resistance and surface diffusivity of a large Brownian particle. J. Colloid Interfac. Sci., Vol. 175, pp. 36-45.

4. Sickert, M., Rondelez, F., Stone, H.A. 2007. Single-particle Brownian dynamics for characterizing the rheology of fluid Langmuir monolayers. Europhys. Lett., Vol. 79, pp. 66005-p1-p6.

5. Petkov, J.T., Danov, K.D., Denkov, N.D. 1996. Precise method of measuring the shear surface viscosity of surfactant monolayers. Langmuir, Vol. 12, pp. 2650-2653.

6. Roomans, G.M., Kozlova, I., Nilsson, H., Vanthanouvong, V., Button, B., Tarran, R. 2004. Measurements of airway surface liquid height and mucus transport by fluorescence microscopy, and of ion composition by X-ray microanalysis. J.Cystic Fibrosis, Vol. S2, pp. 135-139.

7. Dames, P., Gleich, B., Flemmer, A., Hajek, K., Seidl, N., Wiekhorst, F., Eberbeck, D., Bittman, I., Bergemann, C., Weyh, T., Trahms, L., Rosenecker, J., Rudolph, C. 2007. Targeted delivery of magnetic aerosol droplets to the lung. Nat. Nanotechnol., Vol. 2, pp. 495-499.

8. Fischer, T.M., Dhar, P., Heinig, P. 2006. The viscous drag of spheres and filaments moving in membranes or monolayers. J. Fluid Mech., Vol. 558, pp. 451-475.

9. Butt, Ecke, S., Preuss, M., Butt, H-J. 1999. Microsphere tensiometry to measure advancing and receding contact angles on individual particles. J. Adhes. Sci. Technol., Vol. 13, pp. 1181-1191.

10. Hadjiiski, A., Dimova, R., Denkov, N.D., Ivanov, I.B., Borwankar, R. 1996. Film trapping technique: precise method for three-phase contact angle determination of solid and fluid particles of micrometer size. Langmuir, Vol. 12, pp. 6665-6675.

11. King, M., Brock, G., Lundell, C. 1985. Clearance of mucus by simulated cough. J. Appl. Physiol., Vol. 58, pp. 1776-1782.

12. Schürch, S., Geiser, M., Lee, M.M., Gehr, P. 1999. Particles at the airway interfaces of the lung. Colloid Surf. B, Vol. 15, pp. 339-353.

Appendix A

A.1 Sample ANSYS script for finite element analysis of magnets in aerosol channel

```
/PREP7

ET,1,SOLID98,10
ET,2,INFIN47

MPTEMP,,,,,,,,
MPTEMP,1,0
MPDATA,MURX,1,,1.05

MPTEMP,,,,,,,,
MPTEMP,1,0
MPDATA,MGXX,1,,0
MPDATA,MGYY,1,,0
MPDATA,MGZZ,1,,884000

MPTEMP,,,,,,,,
MPTEMP,1,0
MPDATA,MURX,2,,1

cyl4,0,0.1354,0.0127,,,,0.003175
cyl4,0,0.2308,0.0127,,,,0.003175
block,-0.1,0.1,-0.1,0.4,-0.1,0.1,
block,-0.0254,0.0254,0,0.3048,0,0.0254,

cyl4,0,0.1354,0.02,,,,0.0254
cyl4,0,0.2308,0.02,,,,0.0254

vovlap,all
vglue,all

allsel,all
vsel,s,,,1
vsel,a,,,2
!vsel,a,,,3
vatt,1,,1,,
vsel,inve
vatt,2,,1,,
allsel,all
asel,s,,,9
asel,a,,,10
asel,a,,,11
asel,a,,,12
asel,a,,,13
asel,a,,,14
AATT,2,,2,0
```

```
allsel,all
lsel,u,,,33
lsel,u,,,35
lsel,u,,,38
lsel,u,,,40
lesize,all,,,10
lsel,inve
lesize,all,,,30

vmesh,all

FINISH
/SOL
MAGSOLV,2, , ,0.001,25,0
FINISH
/POST1

ETABLE, ,H,X
!*
ETABLE, ,H,Y
!*
ETABLE, ,H,Z
!*
ETABLE, ,CENT,X
!*
ETABLE, ,CENT,Y
!*
ETABLE, ,CENT,Z

PRETAB,
```

A.2 Sample particle trajectory calculation C code for two magnet aerosol flow configuration

```
#include <stdio.h>
#include <stdlib.h>

#include <math.h>
#include <time.h>
#include <string.h>

float pi = 3.14159265;
float g       = -9.81;
float mu_m    = (4e-7)*pi;
float mu_f    = 1.79e-5;
float rho_f   = 1.2;
float rho_p   = 7870;

float t_max   = 1;
float t_step  = 0.001;
```

```
float setheight = 0.005;
int loadflag = 0;
int setflag = 0;
int hits5 = 0;
int hits4 = 0;
int hits3 = 0;
int hits2 = 0;

char filename[] = "2mag-esol.lis";
long results_length=0;

float Hx[1000000];
float Hy[1000000];
float Hz[1000000];
float x[1000000];
float y[1000000];
float z[1000000];
float Px[1000000];
float Py[1000000];
float Pz[1000000];

float k[4][3];

void loadMagFld(char filename[]) {
    FILE * inFile;
    inFile = fopen (filename,"r");

    float temp;
    long i = 0;

    while(!feof(inFile)) {
        fscanf (inFile, "%f", &temp);
        fscanf (inFile, "%f", &temp);
        fscanf (inFile, "%f", &temp);
        fscanf (inFile, "%f", &temp);
        fscanf (inFile, "%f", &temp);
        fscanf (inFile, "%f", &temp);
        fscanf (inFile, "%f", &temp);
        i=i+1;
        }

    results_length = i;

    rewind(inFile);
    fscanf (inFile, "%f", &temp);
    i=0;
    while(!feof(inFile)) {
        fscanf (inFile, "%f", &temp);
        Hx[i] = temp;
        fscanf (inFile, "%f", &temp);
        Hy[i] = temp;
```

```
        fscanf (inFile, "%f", &temp);
        Hz[i] = temp;
        fscanf (inFile, "%f", &temp);
        x[i] = temp;
        fscanf (inFile, "%f", &temp);
        y[i] = temp;
        fscanf (inFile, "%f", &temp);
        z[i] = temp;
        fscanf (inFile, "%f", &temp);
        i=i+1;
        }
    fclose (inFile);
    }

float t      = 0;
long s1      = -1;
long s2      = -1;
long s3      = -1;
long s4      = -1;

float d      = 1e3;
float d1     = 1e3;
float d2     = 1e3;
float d3     = 1e3;
float d4     = 1e3;
float d_sum  = 0;

float HPx;
float HPy;
float HPz;

float dHPx;
float dHPy;
float dHPz;

float Mx;
float My;
float Mz;

float vrel_x = 0;
float vrel_y = 0;
float vrel_z = 0;
float v_x =0;
float v_y = 0;
float v_z = 0;
float r      = 0;

void trace_step(float p_x, float p_y, float p_z,long i,float tmult) {
    float V      = (4/3)*pi*r*r*r;
    float m = V*rho_p;
    float Wx = 0;
```

```
    float Wy = 0;
    float Wz = m*g;

        long j = 0;
        s1 = -1;
        s2 = -1;
        s3 = -1;
        s4 = -1;
        d1 = 1000;
        d2 = 1000;
        d3= 1000;
        d4 = 1000;
        d_sum = 0;
        while(j < results_length) {

            d = sqrt((((x[j]-p_x)*(x[j]-p_x)) + ((y[j]-p_y)*(y[j]-p_y)) + ((z[j]-p_z)*(z[j]-
p_z)));
            if(d<d1) {
                s4=s3;
                s3=s2;
                s2=s1;
                s1=j;
                d4=d3;
                d3=d2;
                d2=d1;
                d1=d;
                }
            else if(d1<=d && d<d2) {
                s4=s3;
                s3=s2;
                s2=j;
                d4=d3;
                d3=d2;
                d2=d;
                }
            else if(d2<=d && d<d3) {
                s4=s3;
                s3=j;
                d4=d3;
                d3=d;
                }
            else if(d3<=d && d<d4) {
                s4=j;
                d4=d;
                }
            d_sum = d1+d2+d3+d4;
            j=j+1;
            }

        HPx = (1-(d1/d_sum))*(1-(d1/d_sum))*Hx[s1];
        HPx += ((1-d2/d_sum)*(1-d2/d_sum))*Hx[s2];
```

```
        HPx += ((1-d3/d_sum)*(1-d3/d_sum))*Hx[s3];
        HPx += ((1-d4/d_sum)*(1-d4/d_sum))*Hx[s4];

        HPy = (1-d1/d_sum)*(1-(d1/d_sum))*Hy[s1];
        HPy += ((1-d2/d_sum)*(1-d2/d_sum))*Hy[s2];
        HPy += ((1-d3/d_sum)*(1-d3/d_sum))*Hy[s3];
        HPy += ((1-d4/d_sum)*(1-d4/d_sum))*Hy[s4];

        HPz = (1-d1/d_sum)*(1-(d1/d_sum))*Hz[s1];
        HPz += ((1-d2/d_sum)*(1-d2/d_sum))*Hz[s2];
        HPz += ((1-d3/d_sum)*(1-d3/d_sum))*Hz[s3];
        HPz += ((1-d4/d_sum)*(1-d4/d_sum))*Hz[s4];

        dHPx = (1-d1/d_sum)*((Hx[s1] - HPx)/(x[s1] - k[i][0]));
        dHPx += (1-d2/d_sum)*((Hx[s2] - HPx)/(x[s2] - k[i][0]));
        dHPx += (1-d3/d_sum)*((Hx[s3] - HPx)/(x[s3] - k[i][0]));
        dHPx += (1-d4/d_sum)*((Hx[s4] - HPx)/(x[s4] - k[i][0]));

        dHPy = (1-d1/d_sum)*((Hy[s1] - HPy)/(y[s1] - k[i][1]));
        dHPy += (1-d2/d_sum)*((Hy[s2] - HPy)/(y[s2] - k[i][1]));
        dHPy += (1-d3/d_sum)*((Hy[s3] - HPy)/(y[s3] - k[i][1]));
        dHPy += (1-d4/d_sum)*((Hy[s4] - HPy)/(y[s4] - k[i][1]));

        dHPz = ((Hz[s1] - Hz[s2])/(z[s1] - z[s2]));
        dHPz = (1-d1/d_sum)*((Hz[s1] - HPz)/(z[s1] - k[i][2]));
        dHPz += (1-d2/d_sum)*((Hz[s2] - HPz)/(z[s2] - k[i][2]));
        dHPz += (1-d3/d_sum)*((Hz[s3] - HPz)/(z[s3] - k[i][2]));
        dHPz += (1-d4/d_sum)*((Hz[s4] - HPz)/(z[s4] - k[i][2]));
        if(HPz*dHPz > 0) {dHPz = -dHPz;}
        v_x = U_x + (m/(6*pi*mu_f*r))*((100*mu_m/rho_p)*HPx*dHPx + Wx/m);
        v_y = U_y + (m/(6*pi*mu_f*r))*((100*mu_m/rho_p)*HPy*dHPy + Wy/m);
        v_z = U_z + (m/(6*pi*mu_f*r))*((100*mu_m/rho_p)*HPz*dHPz + Wz/m);

        k[i+1][0] = p_x + t_step*v_x;
        k[i+1][1] = p_y + t_step*v_y;
        k[i+1][2] = p_z + t_step*v_z;
        k[i][0] = tmult*t_step*v_x;
        k[i][1] = tmult*t_step*v_y;
        k[i][2] = tmult*t_step*v_z;
    }

int traj(float pstart_x,float pstart_y,float pstart_z,char outfilename[])
{
time_t start;
start = time(NULL);

long j      = 0;

  FILE *outFile;
 outFile = fopen (outfilename,"w");
 if(loadflag == 0) {
```

```
    FILE * inFile;
    inFile = fopen (filename,"r");

    float temp;
    long i = 0;

    while(!feof(inFile)) {
        fscanf (inFile, "%f", &temp);
        fscanf (inFile, "%f", &temp);
        fscanf (inFile, "%f", &temp);
        fscanf (inFile, "%f", &temp);
        fscanf (inFile, "%f", &temp);
        fscanf (inFile, "%f", &temp);
        fscanf (inFile, "%f", &temp);
        i=i+1;
        }

    results_length = i;


    rewind(inFile);
    fscanf (inFile, "%f", &temp);
    i=0;
    while(!feof(inFile)) {
        fscanf (inFile, "%f", &temp);
        Hx[i] = temp;
        fscanf (inFile, "%f", &temp);
        Hy[i] = temp;
        fscanf (inFile, "%f", &temp);
        Hz[i] = temp;
        fscanf (inFile, "%f", &temp);
        x[i] = temp;
        fscanf (inFile, "%f", &temp);
        y[i] = temp;
        fscanf (inFile, "%f", &temp);
        z[i] = temp;
        fscanf (inFile, "%f", &temp);
        i=i+1;
        }
    fclose (inFile);
    results_length = i;
    }

long q = 0;
long n = 0;
Px[0] = pstart_x;
Py[0] = pstart_y;
Pz[0] = pstart_z;
float rndmass = (1e-6)*((float)rand()/(float)RAND_MAX);
r = 0.5e-6 + rndmass;
```

```
printf("\nd = %f micrometers\n",2*r*1000000);
fprintf(outFile, "%f\n", r);

while(t < t_max) {

    if(Pz[q] >= setheight) {
        k[0][0] = Px[q];
        k[0][1] = Py[q];
        k[0][2] = Pz[q];
        trace_step(Px[q],Py[q],Pz[q],0,1);
        trace_step(Px[q]+0.5*k[0][0],Py[q]+0.5*k[0][1],Pz[q]+0.5*k[0][2],1,1);
        Px[q+1] = Px[q] + k[1][0];
        Py[q+1] = Py[q] + k[1][1];
        Pz[q+1] = Pz[q] + k[1][2];
        }
    else {
        Px[q+1] = Px[q];
        Py[q+1] = Py[q];
        Pz[q+1] = 0;
        if(setflag==0) {
        if(Py[q]<0.0877) {
            hits5 += 1;
            }
        if(0.0877<=Py[q] && Py[q]<0.1831) {
            hits4 += 1;
            }
        if(0.1831<=Py[q] && Py[q]<0.2785) {
            hits3 += 1;
            }
        if(0.2785<=Py[q] && Py[q]<0.3048) {
            hits2 += 1;
            }
        setflag=1;
        }
    }

    fprintf(outFile, "%f %f %f\n", Px[q],Py[q],Pz[q]);
    q = q + 1;
    t=t+t_step;

    }

printf("run time: %ld\n", time(NULL)-start);

fclose(outFile);
t=0;
q=0;

return 0;
}
```

```
int main() {
srand ( time(NULL)%7 );
int n;
n=0;
float xmin = -0.0225;
float xmax = 0.0225;
float xinc = 0.0025;
float xpos = xmin;
float zmin = 0.005;
float zmax = 0.025;
float zinc = 0.0025;
float zpos = zmin;
char file [20];
char filenum [10];
char fileext [10];
char outfilename[30];
float numparticles;

while(zpos<=zmax) {
    while(xpos<=xmax) {
        itoa (n,filenum,10);
        strcpy(file,"2mag-traj");
        strcpy(fileext,".dat");
        strcpy(outfilename,strncat (file, filenum, 10));
        strcpy(outfilename,strncat (outfilename, fileext, 10));
        traj(xpos,0,zpos,outfilename);
        xpos = xpos + xinc;
        n=n+1;
        loadflag = 1;
        setflag = 0;
        printf("\n\nparticles in section 5: %d\n",hits5);
        printf("particles in section 4: %d\n",hits4);
        printf("particles in section 3: %d\n",hits3);
        printf("particles in section 2: %d\n",hits2);
        printf("total particles traced: %d\n",n);
        }
    zpos = zpos + zinc;
    xpos=xmin;
    }
loadflag = 0;
FILE *resFile;

strcpy(outfilename,"2mag-res.dat");
resFile = fopen (outfilename,"w");

printf("\n\nparticles in section 5: %d\n",hits5);
printf("particles in section 4: %d\n",hits4);
printf("particles in section 3: %d\n",hits3);
printf("particles in section 2: %d\n",hits2);
printf("total particles traced: %d\n",n);
```

```
fprintf(resFile, "\n\nparticles in section 5: %d\n",hits5);
fprintf(resFile, "particles in section 4: %d\n",hits4);
fprintf(resFile, "particles in section 3: %d\n",hits3);
fprintf(resFile, "particles in section 2: %d\n",hits2);
fprintf(resFile, "total particles traced: %d\n",n);
fclose(resFile);

return 0;
}
```